THÈSE

En vue de l'obtention du

DOCTORAT DE L'UNIVERSITÉ DE TOULOUSE

Délivré par :

Institut National Polytechnique de Toulouse (Toulouse INP)

Discipline ou spécialité :

Surfaces Interfaces Continentales Hydrologie

Présentée et soutenue par :

M. TAWFIK RAJEH

le mercredi 5 juin 2019

Titre :

Modeling flow in fractured geologic media: upscaling and application to deep geothermal reservoirs

---

Ecole doctorale :

Sciences de l'Univers de l'Environnement et de l'Espace (SDU2E)

Unité de recherche :

Institut de Mécanique des Fluides de Toulouse (IMFT)

Directeur(s) de Thèse :

M. RACHID ABABOU

M. MANUEL MARCOUX

Rapporteurs :

M. BENOÎT NOETINGER, IFPEN

Mme INGA BERRE, UNIVERSITETET I BERGEN NORVEGE

Membre(s) du jury :

M. PHILIPPE RENARD, UNIVERSITE DE NEUCHATEL, Président

M. DOMINIQUE BRUEL, MINESPARISTECH, Membre

M. ISRAEL CANAMON, UNIVERSIDAD POLITECNICA DE MADRID, Invité

M. JEAN-FRANÇOIS THOVERT, CNRS, Membre

M. MANUEL MARCOUX, TOULOUSE INP, Membre

M. MICHEL GARCIA, SA KIDOVA, Membre

M. RACHID ABABOU, TOULOUSE INP, Membre

MODELING FLOW IN FRACTURED GEOLOGIC MEDIA: UPSCALING AND APPLICATION TO GEOTHERMAL RESERVOIRS

Contents

Remerciement

Je remercie mes directeurs de thèse Mr Manuel Marcoux, maitre de conférences à l'Université Paul Sabatier Toulouse III et Mr Rachid Ababou Professeur à l'Institut Nationale Polytechnique de Toulouse pour le suivi durant mon travail, pour les conseils précieux, pour tous leurs efforts et leur patience.

J'exprime tous mes remerciements à Mr Israel Cañamón Valera Professeur à l'université Polytechnique de Madrid, pour tous ses efforts, ses soigneux conseils et tout son soutien. Aussi, je remercie Mr Philippe Renard de m'inviter au Centre d'Hydrogéologie et de Géothermie de l'Université de Neuchâtel dans le cadre de la mobilité international et pour les précieux échanges et conseils.

Je remercie les membres de comité de suivi de thèse: Mr Jean-François Thovert de l'Institut PPRIME et Mr Wladimir Bergez de l'IMFT pour leurs efforts de suivi et d'accompagnement et pour leurs critiques constructives. Je remercie les membres de Jury d'avoir accepté de juger ce modeste travail.

Je remercie tous les membres du groupe « Milieux Poreux » de l'Institut de Mécanique des Fluides de Toulouse (IMFT) pour l'accueil durant ces 40 mois de thèse.

Enfin je passe un grand salut à tous ceux qui ont été à mes côtés durant ces années de travail : ma famille, mes amis et mes collègues.

Je dédie cette thèse de doctorat à mes parents Chahida et Abdessalem qui m'ont procuré amour, soutien et sacrifice me permettant ainsi de réussir mon parcours.

Résumé

Les fractures dans les roches constituent un chemin préférentiel pour les écoulements et les transferts dans les milieux géologiques. Les roches poreuses fracturées se retrouvent dans diverses applications comme par exemple l'ingénierie pétrolière et gazière, le stockage géologique du CO2 et l'extraction d'énergie géothermique. Cette thèse de doctorat présente un ensemble d'analyses des propriétés géométriques, topologiques et hydrauliques des réseaux de fractures dans une perspective d'homogénéisation et d'application à la simulation numérique des réservoirs géothermique.

La description des fractures planes en 3D, ou plus spécifiquement des réseaux de fractures discrets (dénommés « DFN » pour « Discrete Fracture Networks »), leurs propriétés statistiques et la façon de les modéliser sont étudiés. Comme la perméabilité joue un rôle essentiel dans l'écoulement et le transport dans les roches poreuses fracturées, nous avons dans un premier temps développé une procédure de changement d'échelle (upscaling) pour déterminer le tenseur de perméabilité équivalente des milieux poreux fracturé en 3D. Cette nouvelle approche est basée sur le principe de superposition, amélioré par des facteurs de connectivité déterminés tout d'abord empiriquement. Ces facteurs correctifs ont pour but de prendre en compte les propriétés de connectivité et de percolation des réseaux de fractures. Malgré son efficacité à prédire la perméabilité équivalente, la méthode proposée présente deux limitations dues essentiellement à la difficulté numérique de capter la percolation et les détails des connections des réseaux de fractures. Pour surmonter ces difficultés et pour effectuer des analyses plus fines des réseaux de fractures, un nouvel outil d'analyse des propriétés géométriques et topologiques des réseaux de fractures 3D a été développé. Dans cet outil, tous les attributs géométriques et topologiques (calcul d'intersections, longueurs de traces, amas percolant, etc.) des réseaux de fractures sont déterminés par un ensemble d'algorithmes. Ces algorithmes sont validés en détails, et leurs efficacités computationnelles sont démontrées. La finalité de ces outils algorithmiques est de donner une représentation des réseaux de fractures par graphes.

Avec ces nouveaux outils, les capacités à traiter des réseaux de fractures 3D sont fortement améliorées. Ainsi, en utilisant la représentation en graphes, de nouvelles approches ont été développées concernant trois aspects des réseaux de fractures : (i) la percolation, (ii) le phénomène de groupement de fractures (Clustering) et (iii) la monté d'échelle de la perméabilité par la méthode des graphes.

Un simulateur thermo-hydraulique a in fine été développé avec le code open source « OpenFoam ». L'objectif est d'appliquer les techniques de changement d'échelle développées dans cette thèse à des problèmes de simulations des réservoirs géothermiques. Un premier exemple prototype de système de deux puits d'injection-production dans un réservoir géothermique est simulé. D'autres cas sont en cours de traitement dans le cadre du projet GEOTREF (www.geotref.com).

Abstract

Fractures constitute major pathways for flow and transport in fractured porous rocks. These types of rocks are encountered in a wide range of applications like for example gas and petroleum engineering, CO2 sequestration and geothermal energy extraction.

The present thesis presents a framework to analyze geometrical, topological and hydraulic properties of 3D planar fracture networks with focus on upscaling these properties to obtain an equivalent continuum, in view of application to simulations of geothermal reservoir exploitation. The description of fractures and discrete fracture networks (DFN), their statistical properties and their generation procedures are studied. As permeability plays a key role in flow and transport in fractured porous rocks, we have developed a fast upscaling approach for determining the equivalent permeability tensor of 3D fractured porous media. This new approach is based on the superposition principle improved by empirical connectivity factors in order to take into account the connectivity and percolation properties of the fracture network.

Although efficient in predicting permeability, the proposed method presents a major limitation due mainly to the difficulty in assessing the percolation and connectivity properties of the network. To overcome these limitations and for further insightful analyses of DFN composed of planar fractures, an original framework of geometrical and topological analysis of 3D fracture networks has been developed. In this framework, all the geometrical and topological attributes (intersections, areas, trace lengths, clusters, percolating clusters, etc.) of a DFN are explicitly calculated by a set of algorithms. These algorithms are validated in detail by comparison to commercial softwares, and their computational efficiency is highlighted. The final purpose of this framework is to give a graph representation of the DFN.

Given the newly developed tools, our capabilities of treating fracture networks have drastically increased. Hence, using a graph representation of the DFN, new approaches have been developed concerning two main issues with fracture networks: (i) percolation, (ii) clustering phenomenon (i.e., the formation of clusters by groups of fractures) and (iii) permeability upscaling.

A large scale thermo-hydraulic simulator has therefore been developed with the finite volume open source code "OpenFoam". The purpose is to apply the upscaling techniques to large scale reservoir configurations with a full coupling with heat transfer. A typical example of injection-production wells in a 3D geothermal reservoir is presented, and other cases are being developed within the GEOTREF project (www.geotref.com).

Introduction Générale (Français)

La géothermie consiste à exploiter la chaleur contenue dans le sous-sol, pour produire de la chaleur et/ou de l'électricité. La géothermie peut être classée en trois types selon la profondeur et la température de la ressource. Le premier type est la géothermie basse énergie où la température de la ressource est inférieure à 90 °C , elle est accessible à des profondeurs faibles à moyennes et permet généralement de produire de la chaleur (pour des utilisations urbaines et/ou industrielles). Le deuxième type est la géothermie moyenne énergie. Ce type ne peut être atteint qu'à des profondeurs élevées et à des températures entre 90 et 150°C. La principale utilisation de ce type de géothermie est industrielle par des procédés comme le séchage, la distillation etc. Le dernier type est la géothermie haute énergie. Dans cette catégorie, la température de la ressource est supérieure à 150°C et permet la production de vapeur en quantité suffisante pour des applications industrielles. Elle est localisée en priorité dans des zones volcaniques et permet la production d'électricité. La géothermie haute énergie peut être récupérée d'une façon directe (comme le cas de la centrale de Guadeloupe, en DOM-TOM) ou par stimulation du sous-sol par la technologie EGS (Enhanced Geothermal System), en injectant de l'eau sous pression dans la roche pour réactiver le système de fractures comme à Soultz sous- Forêts, en Alsace, France.

A l'échelle nationale, la centrale de Bouillante en Guadeloupe, est la première centrale géothermique électrique en France qui a été mise en production en 1986. Dans une perspective de transition énergétique, la France a développé un plan de transition énergétique (rapport ADEME 2011), dans lequel deux chiffres clés peuvent être retenus: 23% d'énergie renouvelable (toutes les filières confondues) et 80 MW d'électricité d'origine géothermique en France à l'horizon 2020. En examinant cette feuille de route, nous pouvons retenir un accent particulier concernant la géothermie haute énergie pour la production de l'électricité. Dans ce contexte, un projet novateur (GEOTREF) d'envergure nationale a été lancé en 2014.

Le projet GEOTREF (GEOThermie haute énergie dans les REservoirs Fracturés, http://www.geotref.com) est un projet multi-laboratoires associant une dizaine de laboratoires français et deux entreprises privées. Le projet, est financé par l'Agence de Développement et de Maitrise de l'Energie (ADEME) pour un budget initial de 43M€ (Investissement d'Avenir). L'objectif général du projet est l'amélioration de la compréhension des réservoirs géothermiques et le développement d'outils innovants techniques et informatiques. C'est dans le cadre de GEOTREF que s'inscrit le travail de cette thèse.

La caractérisation d'un réservoir géothermique fracturé à haute énergie nécessite, en général, un découpage séquentiel de taches de la manière suivante (i) la caractérisation des attributs géologique du réservoir, (ii) la simulation thermo-hydraulique, en régime dynamique, du réservoir et (iii) le couplage avec la génération de l'électricité. La thèse se situe à l'interface entre les deux premiers axes (caractérisation géologique du réservoir et simulation thermo-hydraulique de la production de fluide et de chaleur).

Le réservoir fracturé contient une masse rocheuse (perméable ou pas) dans laquelle existe un système de fractures. Etant donné la profondeur des réservoirs géothermiques fracturés, la caractérisation de la nature et des caractéristiques des réseaux de fractures constitue un défi majeur. Malgré la technologie déployée dans cette caractérisation, les connaissances exactes sur la nature des fractures dans le sous-sol restent très modestes. Une revue générale sur la description des systèmes des fractures et leurs attributs a été réalisée. Les méthodes utilisées pour décrire les systèmes de fractures et les techniques déployées pour caractériser, sur le terrain, les roches fracturées sont brièvement étudiés dans cette thèse.

Les fractures existent dans les roches à des échelles différentes et leurs propriétés présentent une hétérogénéité à toutes les échelles d'observation. Ainsi, l'homogénéisation des propriétés thermo-hydrauliques des roches fracturées est nécessaire. L'homogénéisation est obtenue par des techniques de montée d'échelle, qui consistent à obtenir des propriétés équivalentes (à grande échelle, de l'ordre de la taille de la maille de grille du réservoir) à partir des propriétés locales (à petite échelle, de l'ordre de la taille d'une fracture ou d'une carotte de roche poreuse).

La perméabilité d'une roche fracturée joue un rôle clé dans le transport de chaleur par le fluide caloporteur (généralement de l'eau) à travers le système de fractures et la matrice poreuse. Un intérêt particulier est montré, dans cette thèse, pour l'homogénéisation de la perméabilité d'une roche fracturée (où la masse rocheuse elle-même peut être perméable). L'homogénéisation de la perméabilité est ici obtenue par la technique de montée d'échelle. Une technique rapide pour obtenir la perméabilité équivalente d'un volume de roche fracturée est présentée (Rajeh et al. 2019). La technique d'homogénéisation développée est basée sur le principe de superposition avec des coefficients empiriques permettant de tenir compte de la percolation et de la connectivité du réseau de fractures.

La spécificité de la géométrie de fractures rend l'homogénéisation en présence de fractures plus compliquée que pour des roches perméables non fracturées. Les difficultés concernent essentiellement la difficulté de capter la percolation et les détails des connections des réseaux de fractures. La prise en compte de ces difficultés a conduit à une collaboration avec Israel Cañamon (Ecole de Mines de Madrid) pour développer un nouvel outil algorithmique d'analyse des propriétés géométriques et topologiques des réseaux de fractures en 3D. Ces outils ont permis, par la suite, de réaliser des analyses plus fines de différentes propriétés des réseaux de fractures telle que la percolation et le phénomène de Clustering, entre autres. Ainsi, une représentation des réseaux de fractures par des graphes est rendue possible, ce qui ouvre de nouvelles perspectives pour la simulation et pour la montée d'échelle dans les roches fracturées.

Le lien entre l'homogénéisation de la perméabilité et la tâche d'évaluation de la ressource et du fonctionnement du réservoir géothermique est présenté par une application concernant la simulation à l'échelle réservoir. Pour cela, un outil de simulation thermo-hydraulique a été développé avec le code OpenFoam afin de réaliser des simulations des scénarios d'exploitation géothermiques par des puits d'injection (d'eau froide) et de production (d'eau chaude ou vapeur).

La thèse est ainsi organisée en cinq chapitres. Dans le premier chapitre, la description et la caractérisation géologique et hydraulique des fractures et des réseaux de fractures est présentée. Les détails de la génération des échantillons numériques synthétiques des réseaux de fractures sont aussi précisés. Le chapitre 2présente ensuite la description et l'implémentation des techniques numériques de changement d'échelle de la perméabilité. La technique de montée d'échelle par superposition est developpée (Rajeh et al. 2019).

Au chapitre3, les développements algorithmiques concernant le traitement de propriétés géométriques et topologiques détaillées du réseau de fractures sont présentés. La validation détaillée de ces algorithmes et leurs efficacités computationnelles sont mises en évidence. Le chapitre 4 présente les nouvelles approches développées dans cette thèse concernant la percolation, le regroupement de fractures (Clustering), la connectivité des réseaux de fractures ainsi que la représentation en Graphes de l'écoulement dans les réseaux de fractures. Le dernier chapitre présente le formalisme mathématique pour la modélisation thermo-hydraulique à l'échelle du réservoir, l'outil de simulation numérique avec OpenFom, et un exemple d'application à l'échelle du réservoir géothermique. Une conclusion générale et des perspectives sont données à la fin de cette thèse.

General Introduction (English)

Geothermal energy consists in exploiting the heat contained in the subsurface, to produce heat and/or electricity. Geothermal energy can be classified into three types depending on the depth and temperature of the resource. The first type is low energy geothermal where the temperature of the resource is less than $90°C$, it is accessible at low to medium depths and generally produces heat (for urban and / or industrial uses). The second type is moderate geothermal energy. This type can only be achieved at high depths and at temperatures between 90 and $150°C$. The main use of this type of geothermal energy is industrial, for several processes such as drying, distillation, etc. The last type is high energy geothermal energy. In this category, the temperature of the resource is higher than $150°C$, allowing the production of steam in sufficient quantity for industrial applications. It is located primarily in volcanic areas and allows the production of electricity. High energy geothermal energy can be recovered in a direct way (as in the case of the Guadeloupe power plant, in the DOM-TOM, France") or by stimulation of the reservoir by the EGS (Enhanced Geothermal System) technology, by injection of water under pressure in the rock to reactivate the fracture system as in Soultz sous-Forêts, in Alsace, France.

On a national level, the Bouillante power plant in Guadeloupe is the first geothermal power plant in France that has been put into production in 1986. In a perspective of energy transition, France has developed an energy transition plan (ADEME 2011 report with two main objectives: 23% of renewable energy (all sectors combined) and 80 MW of geothermal electricity in France by 2020. By examining this roadmap, one can see the special emphasis on geothermal energy for the production of electricity. In this context, an innovative project (GEOTREF) of national scope was launched in 2014.

The GEOTREF project (GEOThermie haute énergie dans les REservoirs Fracturés, http://www.geotref.com) is a multi-laboratory project involving a dozen French laboratories and three private companies. The project is funded by the Agency for Development and Energy Management (ADEME) for an initial budget of 43M € (in the scope of "Investissement d'Avenir"). The main objective of the project is to improve the understanding of geothermal reservoirs and to develop of innovative technical and computing tools. It is within the framework of GEOTREF that the work of this thesis is inscribed.

The characterization of a high-energy fractured geothermal reservoir generally requires sequential splitting of tasks in the following manner (i) characterization of the geological attributes of the reservoir, (ii) thermo-hydraulic simulation, in dynamic regime, of the reservoir and (iii) coupling with the generation of electricity. The thesis is located at the interface between the first two axes (geological characterization of the reservoir and thermo-hydraulic simulation of the production of fluid and heat).

The fractured reservoir contains a rock mass (permeable or not) in which there is a system of fractures. Given the depth of fractured geothermal reservoirs, the characterization of the nature and characteristics of fracture networks is a major challenge. Despite

the technology deployed in this characterization, exact knowledge about the nature of fractures in the subsurface remains very modest. A general review of the description of fracture systems and their attributes has been carried out. The methods used to describe fracture systems and the techniques deployed to characterize fractured rocks in the field are briefly studied in this thesis.

Fractures exist in rocks at different scales and their properties show heterogeneity at all scales of observation. Thus, the homogenization of the thermo-hydraulic properties of fractured rocks is necessary. The homogenization is here obtained by upscaling techniques, which consist of obtaining equivalent properties (at large scale, with a size of the order of the reservoir) from the local properties (at small scale, a size of the order of a fracture or a carrot of porous rock).

The permeability of a fractured rock plays a key role in the heat transport by the fluid (usually water) through the fracture system and the porous matrix. A particular interest is shown, in this thesis, for the homogenization of the permeability of a porous fractured rock (where the rock mass itself can be permeable). The homogenization of the permeability is obtained here by the upscaling technique. A rapid methodology to obtain the equivalent permeability of a fractured rock volume is presented (Rajeh et al., 2019). The homogenization technique developed is based on the superposition principle with empirical coefficients allowing taking into account the percolation and connectivity of the fracture network.

The specificity of the fracture geometry makes homogenization in the presence of fractures more complicated than for non-fractured permeable rocks. The difficulties mainly concern the detection of percolation and the details of the fracture network connections. The taking into account of these difficulties have led us to collaborate with Israel Canamon (Madrid School of Mines) in order to develop new algorithmic tools for analyzing the geometric and topological properties of 3D fracture networks. These tools have subsequently made possible to carry out finer analyzes of different properties of fracture networks such as percolation and the Clustering phenomenon, among others. Thus, a graph representation of fracture networks has been developed, which opens up new perspectives for simulation and upscaling in fractured rocks.

The link between the homogenization of the permeability and the task of evaluating the resource and the operational functioning of the geothermal reservoir is presented by an application concerning reservoir scale simulation. For this purpose, a thermo-hydraulic simulation tool called "GeothFoam" has been developed with the OpenFoam code in order to simulate geothermal exploitation scenarios with injection (cold water) and production (hot water or steam) wells.

The thesis is organized in five chapters. In the first chapter, the description of geological and hydraulic characterization of fractures and fracture networks is presented. The details of the generation of synthetic numerical samples of fracture networks are also specified. Chapter 2 then presents the description and implementation of numerical permeability upscaling techniques. The technique of upscaling by superposition is developed in detail (Rajeh et al., 2019). In chapter 3, the algorithmic developments concerning the treatment of detailed geometrical and topological properties of the fracture network are presented. The detailed validation, by comparison with the commercial software Comsol Multiphysics, of these algorithms and their computational efficiencies are highlighted. Chapter 4 presents the new approaches developed in this thesis concerning percolation, clustering, fracture network connectivity, and graph-based flow simulation in fractured rocks. The last chapter presents the mathematical formalism for reservoir scale thermo-hydraulic modeling, the

numerical simulation tool developed with OpenFom, and an example of geothermal reservoir scale application. A general conclusion and perspectives are given at the end of this thesis.

Chapter 1

Fractures and Fracture Networks: Description and Generation

1.1 Introduction

Geologic formations, in general, are heterogeneous over a large range of scales. Fractured rocks are even more heterogeneous because of the existence of fracture systems embedded in the rock. Although our main interest in this thesis concerns the hydraulic and thermal properties of the fractured rock at large scale (i.e., the reservoir scale), it is of great importance to gain sufficient knowledge about the geologic nature of fractures, the mechanisms of their formation, their geometric and physical properties, etc. Hence, the aim of this chapter is to give a description of the nature of fractures and of fracture networks and the methodology of their identification. To realize this goal, this chapter is organized as follows. Firstly (Sect. 1.2) , the interest is focused on the geometrical and physical properties of a single fracture: the type of fractures encountered in nature are briefly described and a summary of the attributes of a fracture are listed. Secondly (Sect. 1.3), a review of the methods used to describe and/or numerically generate fracture networks is given. The methods are divided into three categories (geological, mechanical and stochastic) and the advantages and the limitations of each method are also described. Thirdly (Sect. 1.4), the method used in the present work is described. Finally, a conclusion about the topic of fracture networks generation and its relation with the remaining of the thesis is given.

1.2 Geometrical and physical properties of a single fracture

In geology, the term fracture is attributed to a mechanical discontinuity in the rock mass [National Research Council (1996)]. Generally, a fracture is viewed as two rough surfaces separated by void or filled space. Based on the mechanical type of displacement that creates the fracture, fractures are classified into three major groups: (i) dilating fractures, (ii) shearing fractures and (iii) pressuresolution surfaces. The first two groups are also called modes (mode I, mode II and mode III). The dilating fractures (mode I) result from the displacement of the two surfaces away from each other in the direction perpendicular to them. The shearing fractures (mode II) results from the displacement of the two surfaces parallel to each other and perpendicular to the fracture front. Similarly modee III results from the displacement of the two surfaces parallel to each other but parallel to the fracture front. Figure 1.1 is a schematic representation of these three modes adopted from [Pollard and Aydin (1988)].

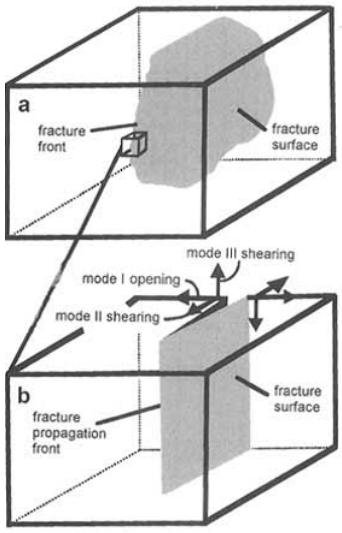

Figure 1.1: The three modes of displacement (modes I, II and III) at the origin of the creation and propagation of fractures (from [Pollard and Aydin (1988)])

These fractures can be found at all scales: from the microscopic scale to continental one. Hence, one can also classify fractures based on their spatial extension. Usually, three scales can be mentioned [Macé (2006)]: (i) microscopic scale fractures, (ii) mesoscale fractures (metric scale) also known as joints and finally (iii) the large scale fractures commonly known as faults.

Fractures, independently from the observation scale, share geometrical and physical characteristics. The geometrical attributes of a single fracture are as follows:

- Fracture location

The first attribute of a fracture is its position in space. The fracture position can be defined by the geometrical coordinates of its center (X_F, Y_F, Z_F). The determination of a fracture position remains a challenge in modeling fractured rocks due to underlying uncertainty.

- Fracture shape:

It is difficult to attribute a precise shape to a fracture embedded in a rock mass. Usually fracture is considered to be a space between two surfaces. The topology of the two surfaces is complex [Adler and Thovert (1999)]. Nevertheless, it is widely assumed, in fracture models, that the two surfaces are planar which is a considerable assumption. The outer contour of the fracture is also of complex shape. However, it can be modeled by some standard shapes such as polygons, rectangles, circles, ellipses etc. [Adler et al. (2012)].

- Fracture aperture

The fracture aperture refers to the mean distance between the two surfaces. This space can be totally open or can contain material (e.g., rock debris). The space could be totally occupied by materials that have precipitated during past fluid circulation through the fracture. In the latter case, the fracture is closed and fluid is not able to pass throw it. Alternatively, the material filling the space between the surfaces of the fracture could be permeable and hence enabling the circulation of fluids. In real cases, fracture aperture

should be modeled using a variable function inside each fracture. [Adler et al. (2012)] present correlated distribution functions of aperture inside single fracture. Nevertheless, it is widely assumed that a fracture has constant aperture; for example, the mean distance between the two surface of the fracture.

- Fracture size:

The fracture size represents its spatial extension. This size is dependent on the fracture shape. Along with the assumption of polygonal fractures, the assumption of disc shaped or elliptical shaped planar fractures is also widely used. Here we focus on planar disc fractures.For example, if the fracture is modeled as a planar disc (which is a widely used assumption), the diameter of the fracture, D_F, is a measure of its size.

- Fracture orientation:

The fracture orientation has its first definition from geologists for whom the dip direction and the dip angle, with reference to the geographic north, are the measure of the fracture orientation. A much simpler orientation definition can be adopted by defining the classical polar angles of the normal vector to the fracture plane as illustrated in Fig. (1.2).

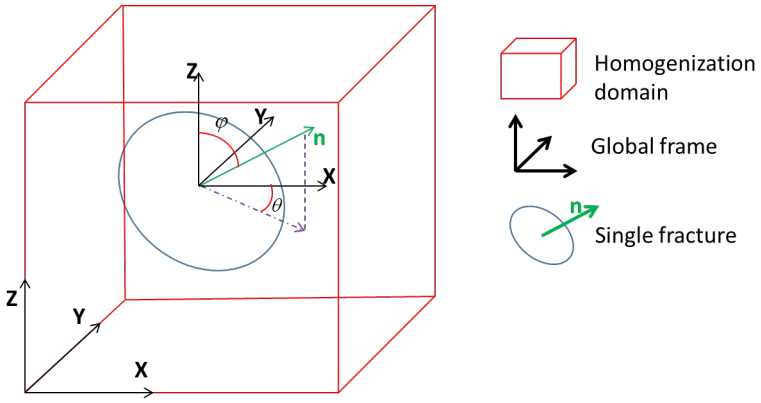

Figure 1.2: Representation of the two spherical angles (θ, φ) defining the orientation of the unit vector "n" (normal to a given planar fracture) with respect to the global frame of the homogenization domain. Here the domain is parallelepipedic, and a single fracture is shown for clarity.

The physical properties of a single fracture are as follow (here only properties directly related to hydraulic are listed):

- Fracture porosity

The porosity θ of a material of volume V is generally defined as the fraction of void in that volume (i.e., $\theta = \frac{V_{void}}{V}$). As mentioned earlier, fractures are not always totally open. If the fracture is totally open, its porosity would be $\theta_F = 1$. In reality and because of the presence of filling material inside the fracture, the fracture porosity varies between 0 and 1. Hence, a closed fracture have no porosity (i.e., $\theta_F = 0$).

- Fracture permeability

The fracture permeability k_f is a measure of how easily fluid flow through the fracture. More extended definition of fracture permeability and its derivation is given later in Chapter 2.

1.3 Generation of fracture networks: a review

In order to understand flow and transport processes in fractured rocks, it is crucial to possess minimum knowledge of fracture network properties. Fractures constituting the network can either be natural or engineered. The description of fracture network properties is the aim of the concept of "Discrete Fracture Network" (DFN). A DFN refers to a computational model that explicitly represents the geometrical properties of each individual fracture (e.g. orientation, size, position, shape and aperture) [Lei et al. (2017)]. Typically, none of these fracture attributes is well known by available data. Usually, the subsurface data about fractures are gathered directly from wellbore samples and analogues outcrops or indirectly from seismic measurements. The direct measurement (i.e., wellbore samples,) gives very limited information about fracture properties due essentially to the restricted size and number of samples. The indirect technique (seismic) is also very limited because of its indirectness. Hence, it is very difficult to give a precise three-dimensional description of fractures and usually field data are collected from lower dimensional observations (2D description from outcrop mapping and 1D description from well logging).

Extensive researches have been conducted in recent decades to overcome the difficulties related to fracture characterization. The detailed works can be found in a recent review on the topic [Lei et al. (2017)]. It comes out from these works that there exist three main methodologies for generating fracture networks. The three methods are (i) the geologically-mapped fracture network, (ii) the stochastically-generated networks and (iii) the geomechanically-generated fracture networks. Ideally, these three methodologies are combined with each other in a single framework in order to reduce uncertainty and to take into account the available data. A detailed description of the three methods is now given in the following sub-sections.

1.3.1 Field-mapped fracture networks

A geologically mapped fracture network is a fracture network deduced from direct or indirect observations. Generating fracture networks from geological data is the most precise way of characterizing fractured rocks. These geological data came from three main sources [Macé (2006)]: (i) Well observations and core drilling, (ii) exposure outcrops and (iii) seismic signal interpretations.

The first type of data (Core drilling) is obtained during drilling or excavation. Once analyzed, these cores give precise informations about fracture characteristics except their spatial extension and this is due to the small size of the cores (the order of magnitude of the well diameter). However, recovering cores is very expensive and the analysis is complicated and time consuming. Additionally, multiple imaging techniques (Borehole Televiewer, Formation MicroImager FMI) has been used to extract images of the wellbore wall and post process them in order to characterize fracture characteristics around the wells and finally generate the corresponding 3D fracture networks by optimization techniques[Zhang et al. (2000)]. Canamon (2006) analyzed trace maps from different boreholes in a granite rocks in the southern part of the Central Massif and a 3D fracture network had been generated accordingly. Recently, [Thovert et al. (2011)] studied the reconstruction of a fracture network observed in an underground gallery of a tunnel buried in clay stones in Switzerland, below Mont Terri.

The second type of data comes from direct observations on analogues exposures. Analogue outcrops are emergent rock volumes considered to have similar properties as the underground rock of interest [Hennings et al. (2000)]. If this similarity is demonstrated,

which is a delicate demonstration; one can characterize the fracture system of the outcrop and then conclude about the fracture system of the underground. However, these outcrops give only two-dimensional representation of the fracture system. Hence, multiple techniques and assumptions are needed in order to estimate the real 3D fracture network [Wennberg et al. (2005)].

The third type of data (Seismic) concerns determining a fracture description in the underground rock based on the interpretation of seismic signals. Seismic data are used to build 3D maps of large-scale (Metric and above) faults. However, the limited resolution of the signal does not enable to capture detailed features such as small cracks [Kattenhorn and Pollard (2001)]. An example of geologically-mapped fracture system if presented in Fig. (1.3).

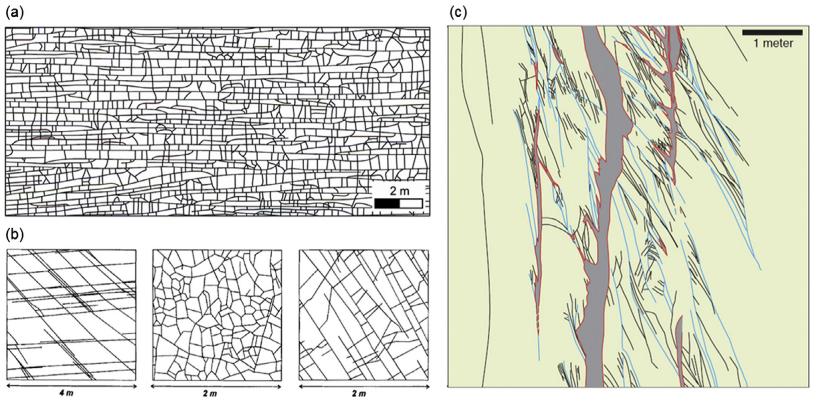

Figure 1.3: Geologically-mapped DFN patterns based on (a) a limestone outcrop at the south margin of the Bristol Channel Basin, UK, (b) sandstone exposures in the Dounreay area, Scotland, and (c) fault zone structures in the Valley of Fire State Park of southern Nevada, USA. From [Lei et al. (2017)]..

1.3.2 Stochastically-generated fracture networks

Due to the high difficulty of performing a complete identification of the 3D fracture systems embedded in subsurface, stochastic approaches have been developed and widely used for decades [Dershowitz et al. (1988)]. In the 1980s, number of works, using stochastically-generated fracture networks, had been performed in order to study the percolation properties of 2D and 3D finite-size fracture networks [Balberg et al. (1983), Robinson (1983)]. Furthermore, many studies regarding fluid flow in fracture networks have been conducted on 3D stochastic networks[Long et al. (1982), Long et al. (1985), Anderson et al. (1984)].

The general stochastic DFN approach assumes fractures to be straight objects in two or three-dimensional space. Usually, fractures are modeled as straight lines in 2D. In 3D, many fracture shapes have been adopted like discs, polygons, rectangles, ellipses etc... Once the fracture shape fixed, the rest of geometrical properties (e.g. position, size, orientation, aperture) are treated as random variables (independent or not) obeying certain probability distributions [Beacher (1983)]. These variables can either be totally random or obeying specified distribution functions which are derived from field measurements such as borehole imaging [Zhang et al. (2000)] as well as scan line [Priest (1981)] or window sampling [Kulatilake (1984)] of outcrop traces or other mapping techniques as mentioned in the previous section. For example, the orientation data can be processed using stereogram

so that fractures can be grouped into different families with respect to their orientations. [Einstein et al. (1983)] reported several distribution functions for the orientation like uniform, normal or Fisher among other distributions. Fracture size is usually attributed to the equivalent radius of the circumscribed circle of the fracture ([Adler et al. (2012)]). Fracture sizes may exhibit several distributions such as log normal, gamma or power law distribution as reported in [Davy (1993)].

The random nature of the stochastic DFN method may be regarded, at first view, as a major inconvenient of stochastically-generated networks. However, this random nature can be seen as an advantageous aspect, as explained in [Lei et al. (2017)], because uncertainty is unavoidable when analyzing complex geological systems. For fractured rocks, single-valued predictions from limited deterministic methods (e.g., geologically-mapped methods (Sect.1.3.1)) may be even more risky [Herbert (1996)]. [Long et al. (1985)] have highlighted the important difference between 2D and 3D fracture networks with respect to connectivity and permeability. This difference renders another advantage of the stochastic method, which has an intrinsic capability of generating 3D networks. However, it is still very important to continue improving the realism and accuracy of stochastic DFN models because unrealistic DFNs may lead to systematically biased physical properties of the fractured medium (e.g. permeability, connectivity, etc.). Hence, it is of critical importance to understand and quantify the uncertainty while generating fracture networks. Current efforts concern the combination of the three generation methods (i.e., geologically, mechanically and stochastically) in a way to obtain the most realistic possible representation of the fracture system in the subsurface. An example of a stochastic network is given in the following figure (Fig. (1.4)) .

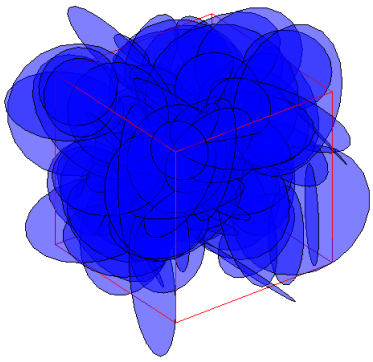

Figure 1.4: 3D Poissonian statistically isotropic fracture network with constant fracture size: this network has been generated with an in-house e matlab code for fracture netwrok generation.

1.3.3 Geomechanically-generated fracture networks

Extensive studies have been conducted to interpret the geological history and the mechanical processes that could explain the formation of natural fracture systems [National Research Council (1996)]. The increased knowledge of fracture mechanics promoted the development of geomechanically based DFN models that incorporate the physics of fracture growth and simulate fracture network evolution as a geometrical response to stress and deformation.[Renshaw and Pollard (1994)] were among the earlier to use numerical

simulations based on a mechanistic model to predict the formation and propagation of fractures and validated their results with experimental observations. Different numerical methods have been used to generate DFN's inspired from geomechanics and based on linear elastic fracture mechanics. The process of fracture generation is performed in four main steps in an iterative manner [Paluszny et al. (2009)]: (i) generation of initial mechanical state of the rock to mimic the process by which natural fractures initiate from micro cracks, (ii) calculation of the perturbed stress field in the rock under imposed boundary conditions, (iii) derivation of the stress intensity factor at the tip of each fracture and (iv) propagation of fractures which satisfy a growth criterion (e.g., the criterion of sub-critical law [Atkinson (1984)]). Many studies used the mechanical approach to generate physically coherent fracture networks and reviews on the subject can be found in the literature (see, for instance, an extended review by [Jing (2003)]). Additionally, some pseudo-mechanical procedures can be used. The pseudo-mechanical methods for fracture network generation are constrained stochastic methods in which mechanical conditions for fracture formation and propagation are integrated in the stochastic generator. For example, [Bonneau et al. (2013)] developed a pseudo-genetic method to generate stochastic fracture models that are consistent with patterns observed on outcrops and fracture growth principles (Fig. (1.5)). More recently, [Bruel (2018)] has developed a geo-mechanically based approach aiming at reproducing the fracture network developing in an extensional context by capturing some pattern inherited from mechanical processes.

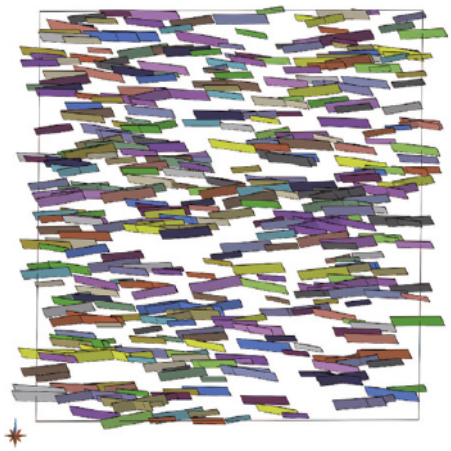

Figure 1.5: Geomechanically-generated 3D fracture network from [Bonneau et al. (2013)]

1.4 Fracture network generation in the present work

It comes out from the review presented in the previous section that describing the fracture system in a given field (e.g., a subsurface reservoir) is a very complicated and human resources consuming task. In engineering applications, this task (the description of the fracture system) can either be dissociated or not from the rest of the reservoir evaluation. As the present work is part of a multi-disciplinary project, we have the opportunity in the framework of the project to work with experts in field studies of fractured rocks (e.g., geology, geophysics etc.). However, one should have in-house numerical tools to generate 3D fracture networks, sophisticated enough to permit the study of the physical (hydraulic and thermal) behavior of the fractured reservoir. In the present thesis, we use the stochastically-

generated fracture networks as the main type of networks to consider in the remaining of this work. This choice is justified by the efficiency and the fast implementation of this method in one hand and by the lack of the available data (at least at the present state of the project) on the other hand. The procedure of generation of the fracture networks used along this thesis is now described. First, the domain size of the hypothetical mass rock is defined in 3D. Usually, a parallelipipedic domain is adopted as illustrated by the red cube in fig. (1.6).

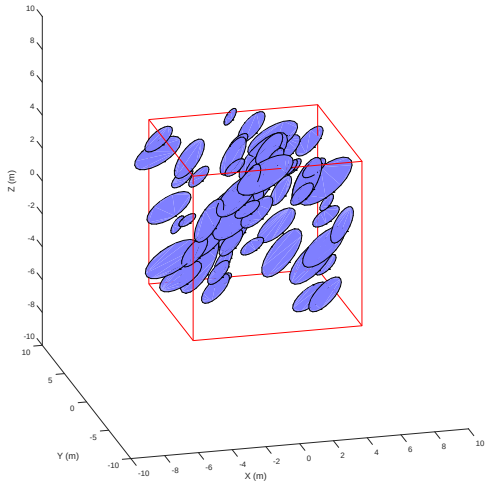

Figure 1.6: Poissonian 3D fracture network in a $10 \times 10 \times 10\,[m]$ cubic domain (red). The fracture size obeys a truncated Pareto law with $R_{min} = 0.5\,[m]$ and $R_{max} = 2.5\,[m]$. The mean azimuth angle of the normal vector to fracture planes is 45 and the standard deviation is 15. This network is generated with an in-home Matlab script.

Once, the 3D domain limits are fixed, the number of fractures to generate can be calculated given the density of fractures which is a user input. At this stage, each attribute of fractures is generated independently with various possibilities of distribution functions. The generation of the different attributes is as follows:

- Distribution of fracture shape

Only two possible shapes are considered in the present work: circular and elliptic. The extension to other fracture shapes studied in the literature (polygons, rectangles etc.) are kept as extensions to this work.

- Distribution of fracture position

It is widely assumed that the fracture position (X, Y and Z coordinates of the fracture center) obeys to Poisson distribution function. This assumption is adopted in the developed fracture generator. The neutrality of the Poisson law is explained by the fact that the probability of finding N_1 fractures in a given region 1 is independent from the probability of finding N_2 objects in a disjoint region 2.

- Distribution of fracture orientation

A direction of a fracrture is determined by two angles of orientation by defining the classical two polar angles of the normal vector to the fracture plane. In this work, fracture network

is divided into families or sets. Each of them is defined by a mean principal directions and the standard deviations around the mean values of the two polar angles. A 3D statistically isotropic network corresponds to the case where the standard deviation is equal to 2π. For example, Fig. (1.6) presents a poissonian network with anisotropic distribution of orientation: a pole around the mean angle $\hat{\theta} = 45$ and a standard deviation of 15 around this mean value.

- Distribution of fracture size

As fractures are assumed to be planar objects in 3D, a measure of fracture size can be modeled by the radius of the equivalent circle corresponding to the fracture contour (a circle with same area as the actual fracture). Fracture networks can be mono disperse and in that case the fracture radius R_F is kept constant. Usually, fractures have different sizes depending on the mechanical conditions of their formation and propagation (cf. previous section). The cases of non-constant fracture size correspond to poly disperse networks. To model the fracture size, many distribution function can be used depending on various field observations [Davy (1993)]. For more details on various fracture size distributions, one can refers to [Bonnet et al. (2001)]. In thiq work, fracture size in poly disperse networks is modeled by truncated Pareto law. The general expression of a truncated Pareto law in a fixed range of values $[R_{min}, R_{max}]$,is given by Eq. 1.1

$$\begin{cases} P(R) = \frac{C}{R^{\alpha}}, if\ R \in [R_{min}, R_{max}] \\ \\ P(R) = 0, if\ R \notin [R_{min}, R_{max}] \end{cases} \tag{1.1}$$

where C and α are the parameters of the Pareto law and R is the the fracture radius.

- Distribution of fracture aperture

It is assumed in this work that aperture is left constant over the network. However, it can be presented by a distribution and can be correlated to the fracture size. Beside the previous stochastically generated fracture networks, it is possible to combine them with deterministic fracture system. All the previous generation techniques are implemented in an in-home Matlab scripts initially developed in (Canamon 2006).

1.5 Conclusion

Definitions and descriptions of fracture and fracture networks are given. The main conclusions from the review of fracture and fracture network generation can be listed as follows.

• The identification of the geometrical and physical attributes of a single fracture or a system of fractures in natural geologic formations is a very complicated task. It needs interdisciplinary skills, adequate technical equipment's and a considerable amount of working time.

• The full three-dimensional description of the fracture system in subsurface reservoir is impossible.

• The generation of fracture networks can be performed mainly using three major methods: geologically-mapped generation, stochastic generation and geomechanical generation.

• Ideally, for generating realistic fracture networks, a combination of the three methods is needed. Stochastic simulation of fracture networks is generally required. Additionally, the characteristics of the fracture sets and fracture network, i.e. fracture orientation, sizes

and aperture, but also the interactions, repulsions, connections and other relationships between fractures can be observed and described using geological maps, outcrops or geomechanical models.

The generation procedure adopted in this work is the stochastic one. The main reasons of this choice are: (i) available data on the fracture network description are limited, (ii) as our focus is about hydraulic and thermal behavior of fracture rock at reservoir scale, this task was attributed to more specialized team in the GEOTREF project and (iii) the stochastic method is the more efficient and easy to implement in order to obtain 3D fracture networks and finally (iv) the stochastic method permit to have unlimited networks enabling to test the validity of the methodologies and conclusions derived from this thesis. To sum up, the fracture network generation is viewed as an upstream task regarding our focus on deriving macro-scale properties of fractured rock at reservoir scale. Although the method used to generate fracture networks is stochastic, the majority of the numerical and theoretical tools developed in the framework of this thesis and the underlying conclusions can be easily extended to more realistic networks generated by other teams (geologists, geomechanists etc.). However, more constraint models of DFN's taking into account abutting, bed control, swarms etc., which are even more realistic, are not studied in this work and are kept as perspectives.

Chapter 2

Fast Upscaling of Permeability of a Fractured Porous Rock

2.1 Introduction

This chapter is mainly constituted from the research paper of Rajeh et al. (2019)[1]. The following is a short introduction to the published work.

Rock permeability presents one of the most important properties regarding flow and transport processes. This aspect is very important for many applications like unconventional gas and petroleum engineering, radioactive waste storage, carbon sequestration, geothermal energy extraction, etc. Permeability of the fractured porous rock has to be obtained at reservoir scale. As seen in the previous chapter, the permeability is a local property that is assigned to a single fracture. To obtain permeability at larger scale (e.g., reservoir grid scale), one has to use homogenization or upscaling techniques. Usually, the upscaling techniques are based on detailed flow simulations in the fractured porous media. These techniques are computationally expensive especially in three-dimensional cases with dense fracture networks. Beside these flow simulation techniques, there exist other approximate approaches to evaluate equivalent permeability. Although these methods are approximate, they are generally much faster than the flow simulation-based techniques.The determination of the equivalent properties of fractured rocks has been under important research efforts in the past two decades (e.g., [Renard et al. (1997), Adler et al. (2012), de Dreuzy et al. (2001)] to name a few). A review of these methods is given at the beginning of this chapter (the paper by Rajeh et al. 2019). We propose a fast upscaling approach based on the superposition principle. This new method is, itself, based on previous works (Snow (1969), Oda (1986), Canamon (2006)). The improvements given in the present work concern essentially (i) a simplified approach to implement the superposition method, and (ii) the introduction of empirical connectivity factors to take into account the percolation properties and the connectivity of the fracture network.

[1]Addendum. One point has to be clarified concerning the published paper (Rajeh et al. 2019). In section 4.2.2.2 of the paper, it was mentioned that in the work of [Mourzenko et al. (2005)], the critical percolation density $\rho_{EX,C}$ does not depend on the fracture size; however this was a false interpretation. In fact, in the work of [Mourzenko et al. (2005)], the dependence of $\rho_{EX,C}$ was revealed and an approximate universal formula for $\rho_{EX,C}$ was proposed in which $\rho_{EX,C}$ is not dependent of fracture size (Eq.26 in [Mourzenko et al. (2005)].

2.2 Fast Upscaling of Hydraulic Conductivity of Fractured Porous Rock: Rajeh et al. (2019)

Math Geosci
https://doi.org/10.1007/s11004-019-09785-w

Fast Upscaling of the Hydraulic Conductivity of Three-Dimensional Fractured Porous Rock for Reservoir Modeling

Tawfik Rajeh[1] · **Rachid Ababou**[1] · **Manuel Marcoux**[1] · **Israel Cañamon**[2]

Received: 30 November 2016 / Accepted: 30 January 2019

Abstract A fast upscaling procedure for determining the equivalent hydraulic conductivity of a three-dimensional fractured rock is presented in this paper. A modified semi-analytical superposition method is developed to take into account, at the same time, the hydraulic conductivity of the porous matrix (K_M) and the fractures (K_F). The connectivity of the conductive fracture network is also taken into account. The upscaling approach has been validated by comparison with the hydraulic conductivity of synthetic samples calculated with full numerical procedures (flow simulations and averaging). The extended superposition approach is in good agreement with numerical results for infinite size fractures. For finite size fractures, an improved model that takes into account the connectivity of the fracture network through multiplicative connectivity indexes determined empirically is proposed. This improved model is also in good agreement with the numerical results obtained for different configurations of fracture networks.

Keywords Fractured porous medium · Three-dimensional upscaling · Equivalent hydraulic conductivity · Numerical simulations · Darcy · Random fracture sets · Network connectivity

Tawfik Rajeh
tawfikrajeh@gmail.com

[1] Institut de Mécanique des Fluides de Toulouse (IMFT), CNRS and Université de Toulouse, 2 Allée du professeur Camille Soula, 31400 Toulouse, France

[2] ETSI de Minas y Energía, Departamento de Ingeniería Geológica y Minera, Universidad Politécnica de Madrid, C./Ríos Rosas 21, 28003 Madrid, Spain

1 Introduction

Geologic formations are heterogeneous over a broad range of scales. Small-scale heterogeneity must be represented at some coarser scale for feasible yet accurate simulations of flow and transport phenomena in reservoirs. The key parameter for hydraulic simulation, the hydraulic conductivity, is upscaled to a coarser grid by assigning an equivalent conductivity K_{EQ} to each cell of the coarse grid. The equivalent hydraulic conductivity K_{EQ} should be distinguished from the effective hydraulic conductivity $K_{\mathrm{EFF.}}$ The equivalent conductivity K_{EQ} can be defined for any finite domain with specific boundary conditions, based on equivalence criteria (as done later in this paper). The effective conductivity K_{EFF} is usually defined theoretically for infinite domain. In the case of a continuous heterogeneous porous medium, and assuming that the local conductivity $K(x,y,z)$ is modeled by a statistically homogeneous and ergodic random function of space, the quantities K_{EQ} and K_{EFF} coincide in the limit of infinite upscaling domain. In the remainder of this introduction, a brief literature review of basic theoretical results on conductivity upscaling for heterogeneous porous media will be presented. Secondly, some of the most common upscaling methods and algorithms available in the literature will be presented. Finally, a summary description of the organization of this paper will be provided.

Theoretical results on equivalent conductivity are found in the literature in two forms, as bounds or as analytical relations. For heterogeneous porous media, the equivalent hydraulic conductivity must satisfy two fundamental inequalities called "Wiener bounds" (Wiener 1912). These bounds have been demonstrated in many works (Wiener 1912; Cardwell and Parsons 1945; Matheron 1967; others). They are given by

$$K_{\mathrm{H}} \leq K_{\mathrm{EQ}} \leq K_{\mathrm{A}}, \tag{1}$$

where K_A and K_H represent respectively the arithmetic and the harmonic mean of hydraulic conductivity.

Other narrower bounds (or tighter bounds)[1] have been obtained in the literature for the equivalent hydraulic conductivity, but their domain of applicability is usually restricted to particular types of spatial distribution or probability distribution of the heterogeneous conductivity. The most known are the "HS" bounds (Hashin and Shtrikman 1963), which are valid only for the case of isotropic binary media (as explained further below). These bounds are given by

$$K_{\mathrm{A}} - \frac{f_1 f_0 (K_1 - K_0)^2}{(1 - f_0)K_0 + f_0 K_1} \leq K_{\mathrm{EQ}} \leq K_{\mathrm{A}} - \frac{f_1 f_0 (K_1 - K_0)^2}{(1 - f_1)K_1 + f_1 K_0}, \tag{2}$$

[1] The terms "narrow bounds" and "tight bounds" both refer to the case where the lower and upper bounds (K_{LOW} and K_{UP}) are relatively close to each other; obviously, the inequality becomes an equality in the ideal case of equal bounds ($K_{\mathrm{LOW}} = K_{\mathrm{UP}}$).

where the labels 0 and 1 refer to the two conductive media ("binary mixture"). Thus, K_0 and K_1 represent respectively the hydraulic conductivities of medium 0 and medium 1; f_0 and f_1 represent the volumetric fractions of the two media; and K_A and K_H are the arithmetic and harmonic means of the binary conductivity distribution.

These HS bounds are theoretically relevant only for isotropic binary media. A fractured porous medium may be modeled as a matrix/fracture binary medium; however, the conductive porous matrix "0" and the conductive fractures "1" do not constitute an isotropic mixture. In addition, even for the ideal case of isotropic binary mixtures, the HS bounds in Eq. (2) may be far apart from each other. To sum up, keeping in mind the objective of upscaling fractured porous media, the HS bounds have several limitations: the assumed isotropy of the binary medium (a theoretical limitation), and the possible lack of tightness of the bounds (a practical limitation).

Analytical expressions for the equivalent hydraulic conductivity have been obtained in the literature, but only for some limited types of heterogeneous media (spatially correlated heterogeneity), or only for special types of discontinuous fractured media. Thus, Matheron (1967) obtained an analytical relation for the macroscopic permeability of a continuous, randomly heterogeneous medium where the local permeability $K(\boldsymbol{x})$ is a random field, under additional hypotheses of statistical homogeneity, isotropy, and ergodicity.[2] More precisely, Matheron's expression is theoretically valid under several hypotheses: (i) Euclidean space is two-dimensional; (ii) the mean flow field is uniform; (iii) the spatial distribution of $K(x,y)$ is statistically invariant under $\pi/2$ rotations (which is implied by statistical isotropy); and finally (iv) the probability distributions of K/K_G and its inverse K_G/K should be identical.[3]

In particular, as a special case, Matheron's relation holds for two-dimensional isotropic spatial distribution of $K(x,y)$ in an infinite domain, provided that the probability density function (PDF) of $\ln(K)$ is symmetric (footnote 3). Matheron's relation is given by

$$K_{\mathrm{EQ}} = E(K)^{1/2}\left[E(K^{-1})\right]^{-(1/2)}, \tag{3}$$

[2] *Homogeneity, ergodicity, isotropy*. A random field, such as $K(\boldsymbol{x})$ or $\ln K(\boldsymbol{x})$, is a random function of position $(\boldsymbol{x})$. The moments of a statistically homogeneous, or "stationary", random field are invariant by translation. Ergodicity refers to the convergence of spatial averages (spatial moments) to ensemble averages (ensemble moments), in the limit of infinite spatial domain. In practice, only the 1st and 2nd order moments are considered (2nd order stationarity and ergodicity). Finally, statistical isotropy refers to the case where the moments of the random field are invariant by rotation.

[3] *Probability distribution of a random field F(x)*. One should distinguish the *single-point* probability law of $F(\mathbf{x})$, from its general *multipoint* probability law. In the case of a Gaussian random field, the one-point and two-point moments suffice to entirely define its *multipoint* probability law. In the two-dimensional case at hand, if $F = \ln K(x,y)$ is assumed Gaussian (in the sense "multi-Gaussian"), then $K(x,y)$ is by definition a "log-normal" random field. In that case, it can be shown that K/K_G and its inverse K_G/K both have well defined *multipoint* laws (log-normal) with the same moments. Furthermore, the mean, variance and two-point covariance of the log-normal $K(x,y)$ can be explicitly related to those of the Gaussian $\ln K(x,y)$.

where $E(K)$ is the mathematical expectation of K. If K is log-normal (that is, if ln$K$ Gaussian, i.e., multi-Gaussian) then Eq. (3) specializes as: $K_{\mathrm{EQ}} = \exp\{E(\ln K)\} = K_{\mathrm{G}}$, which is the geometric mean of K. This relation is also applicable to two-dimensional networks of conductors (Marchant 1977). For more discussions on the probability distribution of K and its consequences, one can refer to Matheron (1967), Ababou et al. (1989) and Zinn and Harvey (2003), as well as the previous footnote. Note also that for a layered medium or for a porous medium containing a parallel set of fractures, the infinite domain equivalent conductivity is the arithmetic mean conductivity if the flow is parallel to the layers and the harmonic mean conductivity if the flow is perpendicular to layers. This classical result has been demonstrated and re-used by many authors since Wiener (1912).

Except for a few results such as those mentioned above, there is no analytical "formula" for determining the equivalent hydraulic conductivity of general three-dimensional fractured porous media, with planar disc fractures. However, many studies in recent decades have led to approximate methods for estimating the equivalent (upscaled) conductivity of a heterogeneous medium. Approximate upscaling methods do not require the direct numerical solution of the detailed equations governing flow in the heterogeneous medium, which are computationally very demanding in terms of CPU time and memory capacity. Indeed, direct numerical simulations require the discretization of the entire fractured porous domain (planar fractures and porous matrix), which leads to a great number of grid nodes or cells, because fracture apertures are very fine compared to porous matrix blocks or to fracture spacing. Among these approximate upscaling methods, the most popular are the self-consistent method (also known as effective medium theory), power averaging methods, and renormalization methods, among others.

The self-consistent method was introduced by Budiansky (1965) in a different context. Dagan (1979) applied the method for upscaling hydraulic conductivity in heterogeneous porous media. He considered a multiphase material made up of homogeneous blocks or "inclusions", with conductivities K_j ($j = 1,\ldots, N$). The blocks are distributed at random in a domain of infinite extent. The following expression was obtained for the effective hydraulic conductivity (Dagan 1979)

$$K_{\mathrm{EFF}} + (m-1)\,K_{\mathrm{M}} = \left[\int_0^{\infty} \frac{f(K)\,dK}{(m-1)K_{\mathrm{EFF}} + K}\right]^{-1}, \tag{4}$$

where the unknown quantity is K_{EFF}, the effective conductivity of the random porous medium; K_M is the conductivity of the porous matrix; "m" is the dimension of Euclidean space ($m = 3$ for a three-dimensional problem); and *f(K)* is the probability density function (PDF) of the random conductivity variable K. Note that the implicit relation in Eq. (4) must be solved or "inverted", for a given *f(K)*, in order to extract from it the effective conductivity K_{EFF}. This can be done analytically or numerically, depending on the probability law of K. The validity of the self-consistent Eq. (4) is limited due to some restrictive hypotheses and approximations. This relation was obtained by an approximate calculation of the pressure field around each "block", assuming that each block is spherical, and replacing the medium surrounding each block by a

homogeneous matrix having the (unknown) conductivity K_{EFF}. It is also assumed that the averaging volume is large compared to the single block inclusion. Pozdniakov and Tsang (2004) generalized the self-consistent method to ellipsoidal inclusions, which could represent fractures. More recently Sævik et al. (2013) proposed three varieties of the self-consistent formulation to ellipsoidal fractures. However, the self-consistent method provides a good estimation of K_{EFF} only in the case of poorly connected fractures or inclusions ("diluted limit").

On the other hand, several authors have proposed different types of power-averages to estimate the equivalent or the effective hydraulic conductivity of a heterogeneous medium. The power average is of the form: $K_{ii,\mathrm{EFF}} = \mathrm{E}(\mathrm{K}^{\mathrm{Pi}})^{1/\mathrm{Pi}}$. Thus, Ababou (1990), Ababou et al. (1994) proposed a power average expression for the principal components of the effective conductivity tensor $K_{ij,\mathrm{EFF}}$ in an N-dimensional medium, where the N exponents (powers Pi) were expressed in terms of N correlation scales (λi). Other authors investigated various semi-empirical formulae for power average upscaling (Journel et al. 1986; Deutsch 1989; Le Loc'h 1988; Dimitrakopoulos and Desbarats 1997; Desbarats 1992). Finally, let us mention some other approximate upscaling methods which are usually implemented numerically, but can also be viewed as quasi-analytical methods. Thus, Renard et al. (2000) proposed and implemented a heuristic method to calculate the equivalent conductivity based on the renormalization method. Their method is based on a combination of the bounds of Cardwell and Parsons. The resulting equivalent conductivity takes into account the three-dimensional geometric anisotropy of the medium, and yields a diagonal equivalent conductivity tensor (the principal directions of anisotropy are not computed, which is a limitation of the method).

The superposition method of Snow (1969), Kiraly (1969) and Oda (1985, 1986), yields equivalent conductivity of a fractured rock assuming impervious porous matrix. The method can be considered as another type of "fast" quasi-analytical upscaling method. The superposition method is exact only in special cases, such as parallel fracture networks. It has been extended to three-dimensional porous media with planar fractures and with non-negligible matrix permeability (Cañamón 2006; Ababou et al. 2011). For more details on this topic, see paragraph around Eq. (5) and the end of Sect. 2.2, where the superposition method is further discussed and compared with previous approaches. This paper will be essentially based on this type of method and several improvements and extensions will be provided.

In summary, some theoretical and approximate results from the literature on the upscaled conductivity of a heterogeneous medium have been presented. The review included analytical bounds and analytical expressions for effective conductivity in specific cases. Approximate methods have been also presented for numerically evaluating the equivalent conductivity of a finite sample numerically, but without solving the detailed flow problem in the heterogeneous porous sample (renormalization-type methods; superposition-type methods). These results can be applied not only to porous medium flow (hydraulic conductivity), but also to various other physical phenomena such as electrical conduction and heat diffusion.

In this paper, our focus is on fractured rock. The need for upscaling is motivated by modeling issues concerning geothermal exploitation, where coupled flow and heat transport occur in the porous rock matrix and also in many rock fractures that cannot

all be represented in detail. Upscaling the hydraulic conductivity leads to an equivalent continuum that is easier and less expensive to model numerically. This constitutes the main motivation of this paper. Now, given the available results and methods in the literature, it appears that the upscaling problem is particularly difficult for the case of fractured porous media, due mainly to the discontinuous nature and the large aspect ratio of the conductive fractures included in the porous matrix. To tackle this problem, this paper focuses on a "fast" superposition method which has already been used in various forms in the literature, and which can be viewed as quasi-analytical. Our aim in the remainder of this paper is to develop a more general type of "fast" upscaling method, which can treat correctly (accurately) the case of fractured porous media in three dimensions. This new method, to be developed here, is basically a modification of the three-dimensional flux superposition method of Ababou, Cañamon et al. (2011), itself based on the original superposition method of Snow 1969 and others. The goal of this paper is to explain the novel superposition method and to demonstrate its validity and limitations.

The remainder of the paper is, therefore, organized as follows. In Sect. 2, the proposed "fast" superposition method will be explained in detail. Sect. 3 describes how to obtain numerically the equivalent conductivity by direct flow simulations (this numerical $\underline{\underline{K}}_{\mathrm{EQ}}$ will serve as a reference to test the validity of the "fast" upscaling method). The validation will be presented in Sect. 4 for different types of fracture networks: "infinite size" fractures (defined further below) (Sect. 4.1); finite size fractures (Sect. 4.2); and finally, the more general case where both "infinite" and finite size fractures are present in the domain (Sect. 4.3). The important parameters in these analyses are: the fracture diameters; the density and connectivity of the fracture set (via the notion of excluded volume); and the fracture/matrix conductivity contrast (K_F/K_M). Discussions and conclusions will be presented in Sect. 5.

2 The Semi-analytical Superposition Method

2.1 General Description of the Method

Snow (1969) and Kiraly (1969) independently proposed a formulation for the equivalent conductivity of a fractured rock, with "infinite size fractures"[4] embedded in an impermeable matrix. This basic approach was later reproduced or extended by several authors (Oda 1986; others). Thus, a general expression of the conductivity tensor K_{ij} for a two-dimensional medium traversed by infinite size fractures was developed, and the final result K_{ij} was shown to depend only on the specific area and volume fraction of each individual fracture (Ababou et al. 1994). Defining an ensemble of M subsets of planar fractures, each with hydraulic apertures, sizes, and geometric parameters

[4] *Infinite size fractures*. It is understood in this paper that the term "*infinite size fracture*" or "*infinite fracture*" refers to any planar fracture that entirely crosses the upscaling domain. More precisely, if the upscaling domain is a convex region of finite volume (e.g., a three-dimensional parallelepiped), then an "infinite fracture" is a planar object that completely crosses the domain: it separates the domain in two subdomains, and its trace on the domain boundary is a closed curve. If the upscaling domain is infinite, then an "infinite fracture" is simply a planar fracture of infinite diameter.

(orientation angles of the normal to the fracture plane), they obtained the equivalent conductivity tensor of an arbitrary set of infinite-length fractures where each subset (labeled "m") is composed of N_m parallel fractures. The equivalent tensor is expressed as

$$K_{ij} = \frac{1}{12}\frac{g}{\nu}\sum_{m=1}^{M}\frac{A_m^3}{L_m}\left[\delta_{ij} - n_{i,m}n_{j,m}\right], \tag{5}$$

where A_m is the mean aperture of the parallel fracture subset "m"; L_m is the mean interspacing between fractures in parallel subset "m"; (δ_{ij}) is the Kronecker symbol; ($n_{i,m}$) is the ith component of the unit vector normal to fracture subset "m"; "g" is the acceleration of gravity ($g = 9.8$ m/s^2); "ν" is kinematic viscosity [m^2/s]. It should be mentioned that the number N_m of fractures within each parallel subset "m" does not appear in the above expression because averaging within each parallel subset has already been performed, resulting in the mean aperture "A_m" and mean spacing "L_m" of parallel set "m". This expression (Eq. 5) was later generalized to an arbitrary set of planar fractures of finite diameters and arbitrary orientations in three-dimensional space, taking also into account a permeable rather than impervious porous matrix (Ababou et al. 2011). The present paper is a further extension to better take into account the possible lack of connectivity of the set of finite diameter fractures (percolation effects).

In the present paper, each fracture is assumed a priori to have an anisotropic hydraulic conductivity, which is expressed in the local coordinate frame of the fracture as follows

$$\underline{\underline{K_{\mathrm{F}}}} = \begin{pmatrix} K_{\mathrm{F}}^{||} & 0 & 0 \\ 0 & K_{\mathrm{F}}^{||} & 0 \\ 0 & 0 & K_{\mathrm{F}}^{\perp} \end{pmatrix}, \tag{6}$$

where $K_{\mathrm{F}}^{||}$ and $K_{\mathrm{F}}^{\perp}$ are, respectively, the parallel and orthogonal components of the fracture conductivity tensor. These principal components could be obtained, in principle, from direct measurements. Alternatively, the parallel fracture conductivity $K_{\mathrm{F}}^{||}$ can be obtained theoretically by invoking the classical cubic law for flow between two parallel plates (planar Poiseuille flow): in this approach, the fracture walls are viewed as smooth parallel plates, flow is laminar (low Reynolds number), and the fracture is opened (not filled with porous material). This approach yields a parallel fracture permeability $K_{\mathrm{F}}^{||}$ [m^2] proportional to the squared aperture, and therefore, a parallel fracture conductivity $K_{\mathrm{F}}^{||}$ [m/s] also proportional to the squared aperture. The parallel fracture transmissivity $T_{\mathrm{F}}^{||}$ [m^2/s] is then proportional to the cubic aperture, hence the name "cubic law", (Tsang 1984; Brown 1987), among others. Finally, the orthogonal conductivity component is interpreted as infinite in this case ($K_{\mathrm{F}}^{\perp} \to \infty$), based on the fact that viscous dissipation due to fluid/solid friction is null in the transverse direction orthogonal to the fracture plane (in the absence of filling material between the fracture walls). Another possible representation of fracture flow is that each frac-

ture behaves, hydraulically, like a Darcian porous material with isotropic conductivity labeled "K_F". In the remaining of the paper, it will be assumed that $K_{\mathrm{F}}^{||} = K_{\mathrm{F}}^{\perp} = K_F$ in the fracture conductivity tensor of Eq. (6). Therefore, K_F is now scalar. Usually, the porous medium in the fracture is coarser and more permeable than the surrounding rock matrix and, therefore, $K_F > K_M$. Finally, in all cases, it is assumed that the porous rock matrix surrounding the fractures behaves according to the isotropic version of Darcy's law (scalar hydraulic conductivity K_M).

In the present superposition approach, the three-dimensional fractured porous domain is considered as the upscaling domain or "homogenization" domain of volume V_{hom}. This domain contains N_f fractures (or pieces of fractures) embedded in the permeable porous matrix. The first step of the superposition approach consists in disjoint partitioning of the domain into N_f "single-fracture" blocks (also named "unit blocks"). Each unit block contains a single fracture surrounded by a portion of the permeable matrix (the unit block in the upper right part of Fig. 1). The volume of each unit block is then calculated as

$$V_{\mathrm{block},\,f} \;=\; \pi\; R_f^2\; b, \tag{7}$$

where R_f is the lateral size of the block "f", equal to the equivalent radius of the fracture (this is the radius of the planar disc with the same area as the portion of the planar fracture located inside the homogenization domain). The transverse size "b" is the same for all unit blocks, and it is calculated by imposing volume conservation for the homogenization domain, as follows (Eq. 8)

$$\sum_{f=1}^{f=N_f} V_{\mathrm{block},\,f} \;=\; \sum_{f=1}^{f=N_f} \pi\; R_f^2\; b = V_{\mathrm{hom}}, \tag{8}$$

where R_f is the equivalent radius of the fracture "f", and b is the thickness of unit block "f". Equation 8 is essentially a volume conservation law.

Based on this decomposition of the fractured domain into unit blocks, two volume fractions are defined and will serve later for the implementation of the superposition method towards conductivity upscaling. First, the volume fraction of each discrete fracture "f", with respect to its corresponding block is defined in Eq. (9). Then, the volume fraction of each unit block "f", with respect to the homogenization domain is introduced in Eq. (10). The two volume fractions are given by

$$\Phi_f \;=\; \frac{V_f}{V_{\mathrm{block},\,f}} \;=\; \frac{\pi\; R_f^2\; a_f}{\pi\; R_f^2\; b} \;=\; \frac{a_f}{b}, \tag{9}$$

$$\Phi_{\mathrm{bloc},\,f} \;=\; \frac{V_{\mathrm{block},\,f}}{V_{\mathrm{hom}}}, \tag{10}$$

where a_f is the aperture of fracture "f".

The direction of the normal vector "$\underline{n}$" is represented, for each fracture "f", by a rotation matrix $\underline{\underline{Rot}}_{\boldsymbol{f}}$. This matrix converts the coordinates of the local coordinate

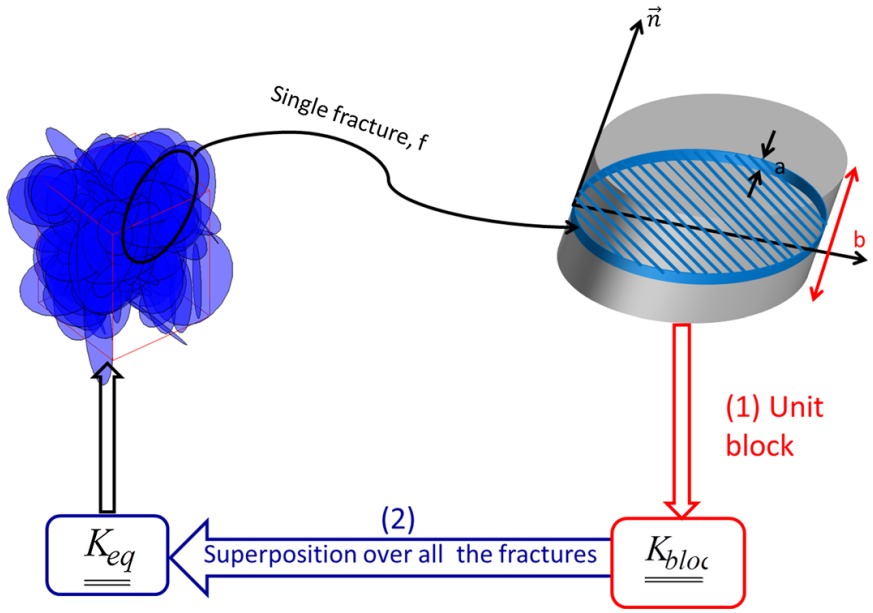

Fig. 1 Illustration of the superposition method for upscaling the hydraulic conductivity in two major steps: (1) upscaling over the single-fracture block, and (2) superposition over all unit blocks

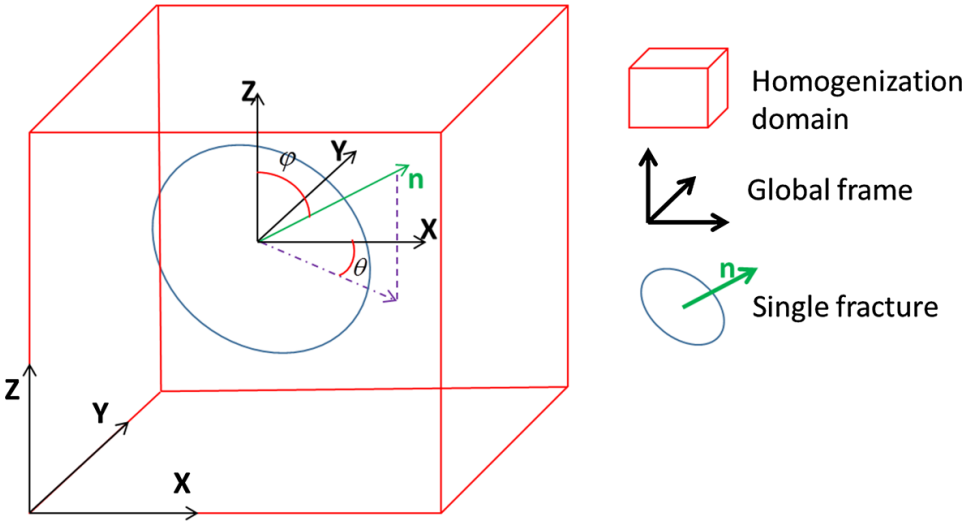

Fig. 2 Representation of the two spherical angles (polar angle φ and the azimuthal angle θ) defining the orientation of the unit vector "$\underline{n}$" (normal to a given planar fracture) with respect to the global frame of the homogenization domain. Here the domain is parallelepipedic, and a single fracture is shown for clarity

frame (fracture "f") to those of the global coordinate frame (homogenization domain). The rotation matrix is given by

$$\underline{\underline{\mathrm{Rot}_f}} = \begin{pmatrix} \cos\theta\ \cos\phi & \sin\theta & -\cos\theta\ \sin\phi \\ -\sin\theta\ \cos\phi & \cos\theta & \sin\theta\ \sin\phi \\ \sin\phi & 0 & \cos\phi \end{pmatrix}, \tag{11}$$

where θ and φ are the spherical angles defining the orientation of the unit vector "$\underline{n}$" normal to the fracture plane. The two angles are illustrated in Fig. 2 for a single planar disc fracture.

2.2 Implementation Steps of the Quasi-Analytical Superposition Method

After the domain decomposition step (leading to a discrete number of "unit blocks"), hydraulic upscaling is implemented in two major steps, as illustrated in Fig. 1. In step (1), a first upscaling is performed at the scale of each single-fracture block and then in step (2), a second upscaling is implemented by superposing the fluxes over all unit blocks.

2.2.1 Step1: The Equivalent Conductivity of a Single-Fracture Block (First Upscaling)

First, a preliminary upscaling is performed on each "single-fracture" block, viewed as a composite medium comprising three "layers" (two matrix layers and one fracture layer). An analytical solution was obtained for flow through this sample by setting appropriate boundary conditions (piecewise linear pressure), calculating the volume averages of the resulting pressure gradient and flux vector fields, and finally, expressing the "exact" equivalent hydraulic conductivity of each "unit" block ($\underline{\underline{K}}_{\text{bloc}}$). The details are shown in Cañamon (2006) and in Ababou et al. (2011). The final result is

$$\underline{\underline{K}}_{\text{bloc}} = \begin{pmatrix} K_A & 0 & 0 \\ 0 & K_A & 0 \\ 0 & 0 & K_H \end{pmatrix}, \tag{12}$$

where K_A and K_H are the weighted arithmetic and harmonic means of K over the block and are given by

$$\begin{cases} K_A = (1-\Phi_f).K_M + \Phi_f.K_F^{\parallel} \\ K_H = \frac{1}{\frac{(1-\Phi_f)}{K_M} + \frac{\Phi_f}{K_{F\perp}}} \end{cases}. \tag{13}$$

At this stage, each "single-fracture block" (unit block) is viewed as a new "fictitious" fracture with conductivity $\underline{\underline{K}}_{\text{bloc}}$. Note also that $\underline{\underline{K}}_{\text{bloc}}$ is a tensorial conductivity and is expressed in the local coordinate frame of the fracture. The conductivity tensor $\underline{\underline{K}}_{\text{bloc}}$ can then be expressed more generally in the global coordinate frame, using the rotation matrix $\underline{\underline{\text{Rot}}}_f$ (Eq. 11).

2.2.2 Step2: Superposition of Fluxes Over All Unit Blocks (Second Upscaling)

Having calculated the equivalent tensorial conductivity of each unit block, the flux contribution of each block is calculated under a given fixed pressure gradient. The flux contributions of all unit blocks are then superposed to obtain the total flux through the domain. This superposition takes into account orientations, diameters, and apertures of all fractures. It finally leads to a linear Darcy-type relation between flux and pressure gradient, with a tensorial equivalent conductivity ($\underline{\underline{K}}_{\text{EQ}}$), at the scale of the

homogenization domain. The resulting equivalent hydraulic conductivity takes the form

$$\underline{\underline{K_{\mathrm{EQ}}}} = \left\{ \sum_f \Phi_{\mathrm{bloc},\,f}\ \underline{\underline{\mathrm{Rot}_f}}\ \ \underline{\underline{K_{\mathrm{bloc},\,f}}}\ \ \underline{\underline{\mathrm{Rot}_f^t}} \right\}, \tag{14}$$

where $\underline{\underline{K}}_{\mathrm{EQ}}$ is the equivalent conductivity tensor of the porous fractured domain ("homogenization" domain); $\phi_{\mathrm{bloc},f}$ is the volumetric fraction of each unit block "f" and $\underline{\underline{K}}_{\mathrm{bloc},f}$ is the equivalent conductivity tensor of unit block "f" (expressed in the local coordinate frame of the block).

The expression given by Eq. (14) is an improved variant of the previous one proposed by Ababou et al. (2011). It takes into account, more directly, the volumetric fractions of fractures. Furthermore, it greatly simplifies the algorithm in the implementation of the method. Note that the resulting tensorial "$\underline{\underline{K}}_{\mathrm{EQ}}$" takes into account the geometric anisotropy of the fracture set, and at the same time, incorporates the permeability (K_M) of the porous matrix. The fact that the hydraulic conductivity of the matrix is taken into account here is an important point because in real geologic formations, the rock matrix may contain finer fractures that are not seen explicitly, and hence, matrix permeability should not be neglected. The connectivity structure of the fracture set is not directly taken into account by the above superposition approach (Eq. 14). This is true as well for earlier types of superposition methods (except for a tentative corrective factor proposed by Oda 1986). The present paper proposes (further below) an empirical method with corrective factors to take into account the effect of fracture set connectivity on the equivalent hydraulic conductivity of the fractured rock (Sects. 4.2 and 4.3).

3 Numerical Upscaling (Direct Simulations and Averaging)

To validate and test the superposition method, computational experiments have been developed in order to determine numerically (rather than theoretically) the equivalent hydraulic conductivity $\underline{\underline{K}}_{\mathrm{EQ}}$ of synthetic samples of three-dimensional fractured porous rocks. To determine numerically a macroscale equivalent hydraulic conductivity $\underline{\underline{K}}_{\mathrm{EQ}}$ for a heterogeneous medium (fractured porous medium), it is necessary to perform detailed numerical simulations of flow inside the porous matrix and the fractures (Sect. 3.1). In this work, the numerical simulations have been carried out in the steady state regime. Several simulations (at least three) are necessary for each fractured sample. Based on the detailed flow field obtained from the numerical experiments, an equivalence criterion (essentially some form of averaging) has been applied to determine numerically the equivalent hydraulic conductivity tensor $\underline{\underline{K}}_{\mathrm{EQ}}$ (Sect. 3.2). The choice of suitable conditions to be imposed at the boundaries of the three-dimensional domain is also important: this is discussed and analyzed in Sect. 3.3.

The subject of numerical upscaling in heterogeneous and fractured porous media has been an intensive area of research in recent decades. Numerical upscaling has been widely used to calculate block conductivities in hydrogeology and petroleum engineer-

ing. Earlier works on this topic include Warren and Price (1961) and Bouwer (1969), among others. Studies on numerical upscaling for heterogeneous and fractured media can be found in Wen and Gomez-Hernandez (1996), Renard and De Marsily (1997), Farmer (2002), Pouya and Fouché (2009), Ababou and Renard (2011) and Lang et al. (2014), among others. In particular, several approaches have been proposed in the literature regarding two essential aspects of numerical upscaling: (i) The equivalence criterion; and (ii) The boundary conditions (or other forcing conditions such as pumping). As will be seen below, our chosen equivalence criterion for numerical upscaling is essentially based on volume averaged flux and head gradient (Sect. 3.2). Furthermore, several possible types of boundary conditions for the numerical flow experiments will be discussed in detail (Sect. 3.3).

3.1 Direct Numerical Simulations of Darcy Flow

In this section, the numerical modeling (then numerical upscaling) of steady state flow in a saturated fractured porous medium is considered. Darcy's law is assumed to be valid inside the porous matrix (with hydraulic conductivity K_M), as well as inside the fractures (with hydraulic conductivity K_F). The areal flux density vector V [$m^3/s/m^2$] (also called Darcy velocity) is governed by Darcy's law. Combining it with mass conservation for steady flow, leads to the system of flow equations to be solved numerically

$$\begin{cases} \vec{\nabla} \bullet \vec{V} = 0 \\ \vec{V} = -K_M \vec{\nabla} H \quad \text{in } \Omega_M \\ \vec{V} = -K_F \vec{\nabla} H \quad \text{in } \Omega_F \end{cases}, \tag{15}$$

where Ω_M, Ω_F are, respectively, the porous matrix and the fractured domain, V is the Darcy velocity and H is the total hydraulic head (also known as piezometric head).

To solve this system of Darcy flow equations, two different tools have been used: the commercial software Comsol Multiphysics (Finite Elements), and the free software BIGFLOW3D (Finite Volumes). In BIGFLOW3D (Ababou et al. Ababou and Bagtzoglou 1993), the flux density vector (V) is inserted in the flux divergence equation, div$(V) = 0$, and the resulting elliptic equation is solved for the hydraulic head H. The flux vector field V is then retrieved numerically from Darcy's head gradient law. The two tools present two complementary advantages: Comsol Multiphysics can handle adaptive meshing, which is very useful if high resolution is needed locally (e.g., at fracture intersections), and BIGFLOW code can handle much larger grids, with millions of cells or more, but without adaptive meshing. The choice of these two numerical software packages allows one to benefit from the short computation time (BIGFLOW3D) on the one hand, and customized adaptive meshing available in Comsol Multiphysics on the other hand. The use of each code will be indicated case by case in the sequel. For example, Fig. 3 displays graphically some computational IO's (Inputs and Outputs). The fractured porous medium is projected onto a three-dimensional cartesian grid of voxels (as shown at left). The iso-surfaces of hydraulic head H obtained by solving the flow equations (Eq. 15) are shown at right. In this example there are $N = 125$

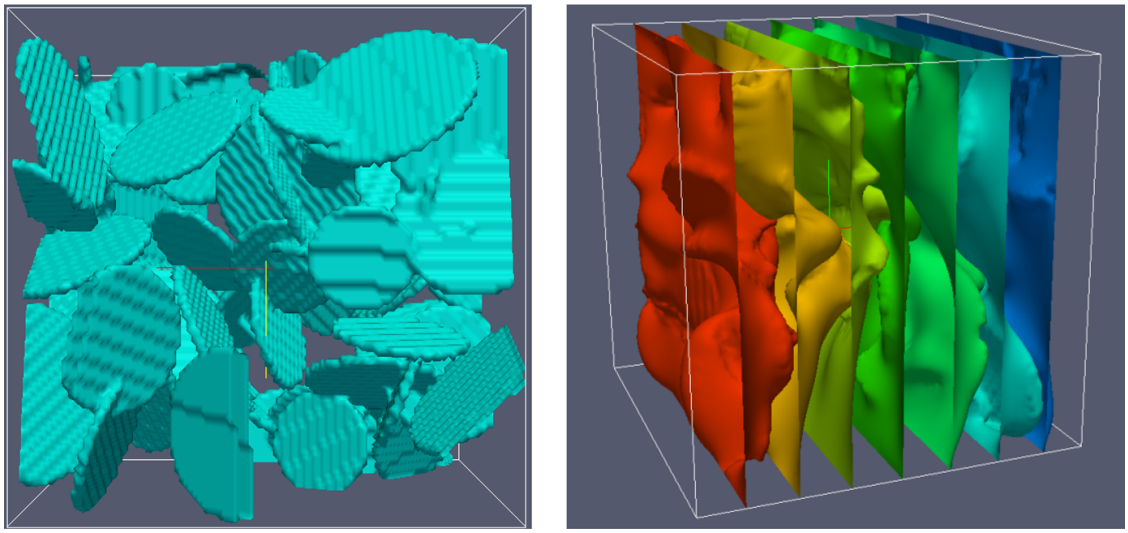

Fig. 3 Left: structured 3D Finite Volume Mesh (FVM) display of the fractured porous domain, with $N = 125$ planar disc fractures, and Ncells $\approx N1 \times N2 \times N3 \approx 106$ cells. Right: numerical flow simulation using the Finite Volume BIGFLOW 3D code (iso-surfaces of hydraulic head are shown)

planar disc fractures in the domain, and the fracture/matrix conductivity contrast is one million ($K_F/K_M = 10^6$). The three-dimensional domain was discretized into one million finite volume cells ($N_{\text{cells}} \approx N_1 \times N_2 \times N_3 \approx 10^6$).

A toolbox has been developed (in Matlab®) for numerically upscaling the hydraulic conductivity of the porous fractured medium based on the numerical flow field (H, V). For this purpose, the numerical tools mentioned above (FEM in Comsol, Finite Volumes in BIGFLOW3D) are used to solve the flow PDEs for each three-dimensional heterogeneous porous sample. These tools are combined with a "Live-Link" with Matlab in order to facilitate the numerical upscaling procedure (computing flux averages, etc.).

3.2 Averaging and Equivalence Criteria (Equivalent Darcy Law)

At the macroscale (homogenization scale), it is assumed here (by choice) that there exists an equivalent Darcy's law relating the volume average flux to the volume average gradient. This equivalence criterion is called VAF (volume average flux). As a consequence, at the homogenization scale, the laws governing the flow are

$$\begin{cases} \nabla \cdot \left\langle \vec{V} \right\rangle = 0 \\ \vec{V} = -\underline{\underline{K_{\text{eq}}}} \left\langle \vec{\nabla} H \right\rangle \end{cases}, \tag{16}$$

where

$$\begin{cases} \left\langle \vec{V} \right\rangle = \frac{1}{V_{\text{hom}}} \int_{V_{\text{hom}}} \vec{V} \, dV_{\text{hom}} \\ \left\langle \vec{\nabla} H \right\rangle = \frac{1}{V_{\text{hom}}} \int_{V_{\text{hom}}} \left(\vec{\nabla} H \right) dV_{\text{hom}} \end{cases}. \tag{17}$$

The angular brackets $<\bullet>$ in Eqs. (16, 17) indicate the volumetric average of the quantity "•". The "VAF" approach is widely used in the literature Pouya and Fouché (2009), Renard and Ababou (2009), Ababou and Renard (2009), Ababou and Renard (2011) and Lang et al. (2014) and others. It is worth mentioning here that other types of averaging have also been defined and used in the literature, such as "NSF" for net surface flux, among others. In addition, other criteria can be invoked, such as upscaling the mechanical work (or viscous dissipation work) rather than the flux (Ababou and Renard 2011).

A fully three-dimensional $\underline{\underline{K}}_{\mathrm{EQ}}$ tensor must be identified. Since each numerical simulation yields three scalar equations, the nine components of the $\underline{\underline{K}}_{\mathrm{EQ}}$ tensor ($i =$ 1,2,3 and $j = 1,2,3$) can be determined with three numerical simulations corresponding to three different directions of the imposed head gradient. Therefore, in each of the three numerical experiments ($m = 1, 2, 3$), it is assumed that

$$V_i^{(m)} = \left\langle \frac{\partial H^{(m)}}{\partial X_j} \right\rangle K_{\mathrm{EQ}ij} \; (m = 1, 2, 3)\,, \tag{18.a}$$

where implicit summation have been used on repeated indices. Finally, the following 9×9 linear system (Eq. 18.b) is obtained, which allows the determination of the nine components of the equivalent $\underline{\underline{K}}_{\mathrm{EQ}}$ tensor (presumed to be non-symmetric a priori) as follows

$$\begin{bmatrix}
\langle \nabla H_X^1 \rangle & \langle \nabla H_Y^1 \rangle & \langle \nabla H_z^1 \rangle & 0 & 0 & 0 & 0 & 0 & 0 \\
0 & 0 & 0 & \langle \nabla H_X^1 \rangle & \langle \nabla H_Y^1 \rangle & \langle \nabla H_z^1 \rangle & 0 & 0 & 0 \\
0 & 0 & 0 & 0 & 0 & 0 & \langle \nabla H_X^1 \rangle & \langle \nabla H_Y^1 \rangle & \langle \nabla H_z^1 \rangle \\
\langle \nabla H_X^2 \rangle & \langle \nabla H_Y^2 \rangle & \langle \nabla H_z^2 \rangle & 0 & 0 & 0 & 0 & 0 & 0 \\
0 & 0 & 0 & \langle \nabla H_X^1 \rangle & \langle \nabla H_Y^2 \rangle & \langle \nabla H_z^2 \rangle & 0 & 0 & 0 \\
0 & 0 & 0 & 0 & 0 & 0 & \langle \nabla H_X^2 \rangle & \langle \nabla H_Y^2 \rangle & \langle \nabla H_z^2 \rangle \\
\langle \nabla H_X^3 \rangle & \langle \nabla H_Y^3 \rangle & \langle \nabla H_z^3 \rangle & 0 & 0 & 0 & 0 & 0 & 0 \\
0 & 0 & 0 & \langle \nabla H_X^3 \rangle & \langle \nabla H_Y^3 \rangle & \langle \nabla H_z^3 \rangle & 0 & 0 & 0 \\
0 & 0 & 0 & 0 & 0 & 0 & \langle \nabla H_X^3 \rangle & \langle \nabla H_Y^3 \rangle & \langle \nabla H_z^3 \rangle
\end{bmatrix}
\begin{bmatrix} K_{11} \\ K_{12} \\ K_{13} \\ K_{21} \\ K_{22} \\ K_{23} \\ K_{31} \\ K_{32} \\ K_{33} \end{bmatrix}
=
\begin{bmatrix} \langle V_x^1 \rangle \\ \langle V_y^1 \rangle \\ \langle V_z^1 \rangle \\ \langle V_x^2 \rangle \\ \langle V_y^2 \rangle \\ \langle V_z^2 \rangle \\ \langle V_x^3 \rangle \\ \langle V_y^3 \rangle \\ \langle V_z^3 \rangle \end{bmatrix}. \tag{18.b}$$

This 9×9 linear system is easily solved numerically for the nine unknown conductivity components, given the flow data from the three numerical simulations. The flow data in this system are: the mean velocity components (right hand side vector 9×1) and the mean head gradient components (9×9 matrix). The previous linear system (Eq. 18.a–b) is solved, initially, for the non-symmetric $\underline{\underline{K}}_{\mathrm{EQ}}$ tensor, and then a symmetric tensor is obtained by taking the symmetric part ($(\underline{\underline{K}}_{\mathrm{EQ}+} \; \underline{\underline{K}}_{\mathrm{EQ}}^{\mathrm{T}})/2$). In most cases presented in this paper, the anti-symmetric part was negligible.

3.3 Boundary Conditions (BC) at the Homogenization Scale (Macroscale)

To solve the upscaled equations of flow at the macroscale, the boundary conditions have to be specified. There are various possible types of boundary conditions studied here: (i) permeameter conditions; (ii) linearly distributed head (constant gradient boundary conditions); and (iii) constant head conditions. (Note: in this subsection, the simulation results were obtained with Comsol Multiphysics).

3.3.1 Permeameter Boundary Conditions (PBC)

These conditions consist in imposing fixed heads on two opposite boundaries of the three-dimensional domain (H_0 and H_1) and setting the remaining boundaries to be impermeable (i.e., zero normal flux). These boundary conditions are simple and practical (for numerical, as well as physical laboratory experiments), especially if the purpose is only to determine the equivalent isotropic or diagonal hydraulic conductivity tensor in the frame of the sample. However, more generally, Kfoury et al. (2006) applied permeameter conditions to determine the full tensorial permeability on a two-dimensional sample, and later on, Li et al. (2011) determined the full three-dimensional tensor with the same permeametric conditions. The full tensor determination from these boundary conditions (PBC) requires more complicated averaging procedures: cross-differentiation (Kfoury et al. 2006); skin technique (Li et al. 2011). In this study, the purpose is determining the full equivalent tensor for a given averaging criterion "VAF" under various types of boundary conditions. The permeametric boundary conditions (PBC) will be used only in Sect. 4.2.1 to compare the sensitivity of percolation phenomena to the type of boundary conditions.

3.3.2 Immersion Boundary Conditions (IBC)

"Immersion" boundary conditions (IBC) are implemented by imposing a linearly distributed head $H(x,y,z)$ on the boundary of the sample (that is, on all six faces of the boundary, if the sample is parallelepipedic). These boundary conditions are called "immersion" boundary conditions, because the sample appears to be "immersed" in an infinite domain with a "far field" hydraulic gradient imposed everywhere outside the rock sample. The resulting boundary condition (IBC) can be expressed as a linear head profile ($H\left(\overrightarrow{x}\right) = H_0 - \overrightarrow{J_0} \bullet \overrightarrow{x}$), where H_0 is the hydraulic head at the origin, and $\overrightarrow{J_0}$ is a spatially imposed constant hydraulic gradient.

In the literature, the linear head or linear pressure boundary condition has been widely used for studying PDE problems of the form div(K grad u)$=f$ for constant and variable K. Earlier mathematical references include Bamberger (1977). This type of boundary condition has also been used by Long et al. (1982), and more recently by Pouya and Fouché (2009), Ababou and Renard (2011), and others, for theoretical and numerical upscaling of permeability in heterogeneous and/or fractured media. The IBC flow condition seems to be consistent with the physics of flow in natural rocks: the homogenized sample (sub-domain) is not isolated from the rest of the flow domain, and it is affected by the far field head gradient of the surroundings. By the same token, the IBC gives a large degree of freedom to flow: for instance, under steady flow, water can circulate between any two boundary faces of the three-dimensional domain, and it can also flow out at one point and re-enter at another point of the same boundary face. Indeed, there may exist a flow re-entry at the intersection of one isolated finite size fracture with the domain boundary (Fig. 4). Such boundary re-entry effects, caused by "IBC", can be quite significant, as can be seen in Fig. 4 (zoom insert): the small isolated fracture intersecting a boundary face participates significantly to the volumetric average of velocity, even though the fracture is not

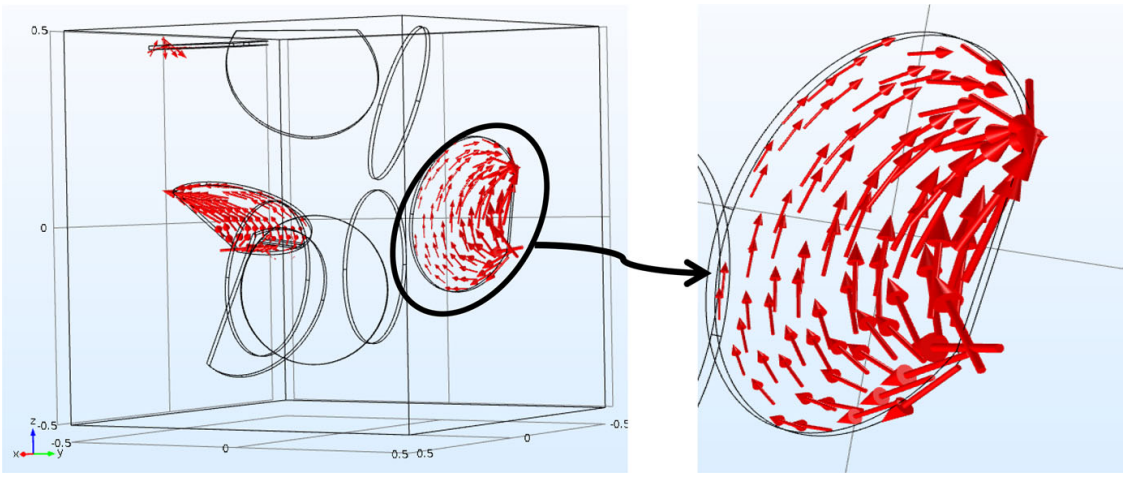

Fig. 4 Left: representation of the Darcy velocity field (arrows) in the case of "IBC". There are nine fractures of radius $R = 2\ [m]$. Domain size is $10 \times 10 \times 10\ \mathrm{m}^3$. Conductivity contrast is $K_F/K_M = 10^6$. Right: zoom on an isolated fracture intersecting one boundary face, illustrating the re-entry effects

connected to any percolating cluster inside the domain. The consequences will be examined in Sect. 3.4, where it will be concluded that other boundary conditions are more suitable for studying percolation effects.

3.3.3 Constant Heads Boundary Condition (CHBC)

The previously described immersion boundary conditions (labeled "IBC") could be replaced by other boundary conditions in order to avoid the effects of flow re-entry at boundary/fracture intersections (described above), while still allowing the full determination of an equivalent conductivity tensor $\underline{\underline{K}}_{\mathrm{EQ}}$. One such method consists in imposing constant heads, rather than linearly distributed heads, on all boundary faces: H_0 and H_1 are imposed on two opposite boundary faces, and $(H_0 + H_1)/2$ is imposed on all the other "lateral" boundary faces. For this reason, this method is labelled "constant heads boundary conditions" (CHBC). This choice of boundary conditions comes at a price: the discontinuity of boundary heads at corners and edges. However, the comparison just below reveals the possible advantages of CHBC.

3.4 Comparison of Different Types of Boundary Conditions (IBC Versus CHBC)

This section presents a comparison of the numerical upscaling method based on two types of boundary conditions: "immersion boundary conditions (IBC)" and "constant heads boundary conditions (CHBC)". The comparisons are made for the case of a three-dimensional set of statistically isotropic, "infinite size" planar fractures (in practice these are generated as planar disc fractures with diameters much greater than domain size, as explained in footnote in Sect. 2.1). Matrix conductivity ($K_M = 10^{-5}$ m/s) is chosen much lower than fracture conductivity ($K_F = 10$ m/s), in order to emulate the case of a discrete fracture network (here the fracture/matrix conductivity ratio is very high: one million). The numerical $\underline{\underline{K}}_{\mathrm{EQ}}$ tensors obtained with IBC and CHBC are relatively close, but not identical, as shown in Fig. 5. Nevertheless, it can be

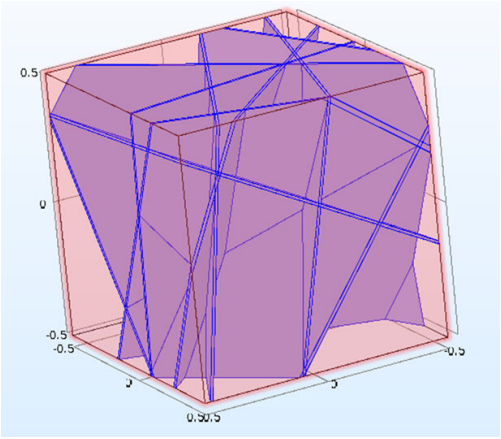

$$\begin{cases} \underline{\underline{K_{EQ}}}_{IBC} = \begin{pmatrix} 4.11 & & \\ & 4.29 & \\ & & 4.36 \end{pmatrix} \\ \underline{\underline{K_{EQ}}}_{CHBC} = \begin{pmatrix} 3.33 & & \\ & 3.43 & \\ & & 3.74 \end{pmatrix} \end{cases}$$

Fig. 5 Left: fracture network composed of "infinite" fractures (all factures completely intersect the homogenization domain). Right: equivalent hydraulic conductivity tensor $\underline{\underline{K}}_{\mathrm{EQ}}$ obtained for the two boundary conditions [immersion (IBC) and constant heads (CHBC)]

considered that the two results are similar, given the high contrast K_F/K_M, and given the discontinuity effects due to CHBC at corners and edges are weak in this case.

However, the conclusions are quite different for a case involving a non-percolating network of finite size fractures. The case considered here is a fracture set comprising nine planar disc fractures, such that the fractures do not traverse the domain boundaries individually and do not form a percolating cluster of fractures collectively (Fig. 6 on the left). The equivalent conductivity tensors $\underline{\underline{K}}_{\mathrm{EQ}}$ obtained numerically with the two different types of boundary conditions (IBC, CHBC) are very different, as shown in Fig. 6 (on the right). In this example, it can be clearly seen (because there are very few fractures in the domain) that there does not exist a percolating cluster of fractures. Therefore, one would expect the equivalent hydraulic conductivity $\underline{\underline{K}}_{\mathrm{EQ}}$ to be very close to the conductivity of the porous matrix (here $K_M = 10^{-5}$ m/s). As can be seen, the resulting $\underline{\underline{K}}_{\mathrm{EQ}}$ obtained with the constant Heads boundary conditions (CHBC) yields values much closer to those expected. The conductivity tensor from IBC overestimates the equivalent hydraulic conductivity by two orders of magnitude (~600). This overestimation due to IBC boundary conditions is explained by a flow re-entry phenomenon at the intersection of one isolated fracture with a boundary face (as in Fig. 4, zoom insert). For this reason, "constant heads boundary conditions (CHBC)" has been chosen for the numerical experiments to be presented in the remainder of this paper. The previous comparison justifies the choice of CHBC, particularly for poorly percolating fracture sets, even if these conditions could generate discontinuities at the borders (while IBC maintains continuity at the borders).

4 Comparisons, Validation Tests, and Extension of Upscaling Method

This section deals with comparison of the upscaled conductivity obtained with the "fast" superposition method developed earlier, with the one obtained numerically. The numerical simulation results are exploited for several different fracture network configurations (in terms of fracture size, density, connectivity, and fracture/matrix conductivity ratio). The objective is to validate the fast upscaling method (superposition

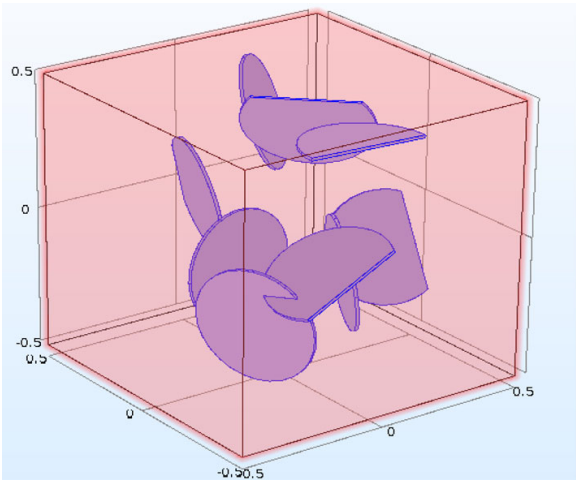

$$\begin{cases} K_{IBC} = \begin{pmatrix} 0.009 & 0.001 & 0.0009 \\ 0.001 & 0.003 & 0.001 \\ 0.0009 & 0.001 & 0.006 \end{pmatrix} \\ K_{CHBC} = \begin{pmatrix} 1.2E^{-5} & 2E^{-7} & 2E^{-7} \\ 2E^{-7} & 1.7E^{-5} & 8E^{-7} \\ 2E^{-7} & 8E^{-7} & 1.3E^{-5} \end{pmatrix} \end{cases}$$

Fig. 6 Left: fracture network composed of finite size fractures. Right: equivalent hydraulic conductivity tensors $\underline{\underline{K}}_{\mathrm{EQ}}$ obtained for the two boundary conditions, immersion (IBC) and constant heads (CHBC)

method), to improve it and propose possible extensions. Because the behavior of the equivalent hydraulic conductivity greatly depends on the size of fractures, the following types of fracture networks are treated separately: infinite size fractures (Sect. 4.1); then finite size fractures (Sect. 4.2); and finally a mixture of infinite and finite size fractures (Sect. 4.3). Most of the numerical tests are conducted for a large contrast of fracture/matrix conductivity.

4.1 Comparisons and Validation Tests: Case of Infinite Size Fractures

Several cases have been tested, involving two-dimensional and three-dimensional sets of infinite size fractures: parallel fractures; inclined set of parallel fractures; Cartesian network, which implies that the fracture orientations are aligned with spatial frame axes (X, Y and Z directions); random set of three-dimensional Poissonian fractures with statistically isotropic orientation among other cases. A fracture set is Poissonian if the fracture centers (X, Y, Z) are distributed according to a three-dimensional Poisson point process; the positions X, Y, Z are uniformly distributed (Vanmarcke 1983). A fracture set is statistically isotropic in the following sense: consider the intersection points of their unit normal vectors with the unit sphere; these points must be distributed uniformly on any spherical cap on the surface of the unit sphere.[5] Reminder: the term "infinite" indicates that each fracture has a diameter larger than the diameter of the rock sample domain (Sect. 2.1). In that case, each individual fracture is percolating "on its own", which means that each individual fracture connects at least two boundary faces. Obviously, the network is also fully percolating as well.

As expected, for fully connected and percolating fracture networks, the results obtained by numerical experiments show that upscaled permeability tensors $\underline{\underline{K}}_{\mathrm{EQ}}$ obtained by the present fast superposition and by numerical experiments are in good

[5] The consequence in three-dimensional space is that the longitude angle Θ must be distributed uniformly in $[0, 2\pi]$, and (independently) the latitude angle φ has its cosine distributed uniformly in $[-1, +1]$.

Table 1 Detailed results of the comparison between numerical upscaling and superposition upscaling for the fracture set of Fig. 7 (parallel inclined fracture set)

Numerical upscaling	Upscaling by fast superposition method
$K_{\text{numerical}} = \begin{pmatrix} 0.00235 & 0 & 0.00312 \\ 0 & 0.0109 & 0 \\ 0.00312 & 0 & 0.009806 \end{pmatrix}$	$K_{\text{superposition}} = \begin{pmatrix} 0.00226 & 0 & 0.00576 \\ 0 & 0.01249 & 0 \\ 0.00576 & 0 & 0.01483 \end{pmatrix}$
Eigen values:	Eigen values:
$K^*_{\text{numerical}} = \begin{pmatrix} 0.00121 & 0 & 0 \\ 0 & 0.0109 & 0 \\ 0 & 0 & 0.0109 \end{pmatrix}$	$K^*_{\text{superposition}} = \begin{pmatrix} 0.0019 & 0 & 0 \\ 0 & 0.0124 & 0 \\ 0 & 0 & 0.0170 \end{pmatrix}$
Eigen vectors:	Eigen vectors:
$\begin{pmatrix} V_1 & V_2 & V_3 \\ 0.939 & 0 & 0.341 \\ 0 & -1 & 0 \\ -0.341 & 0 & 0.939 \end{pmatrix}$	$\begin{pmatrix} V_1 & V_2 & V_3 \\ 0.931 & 0 & 0.362 \\ 0 & -1 & 0 \\ -0.362 & 0 & 0.931 \end{pmatrix}$

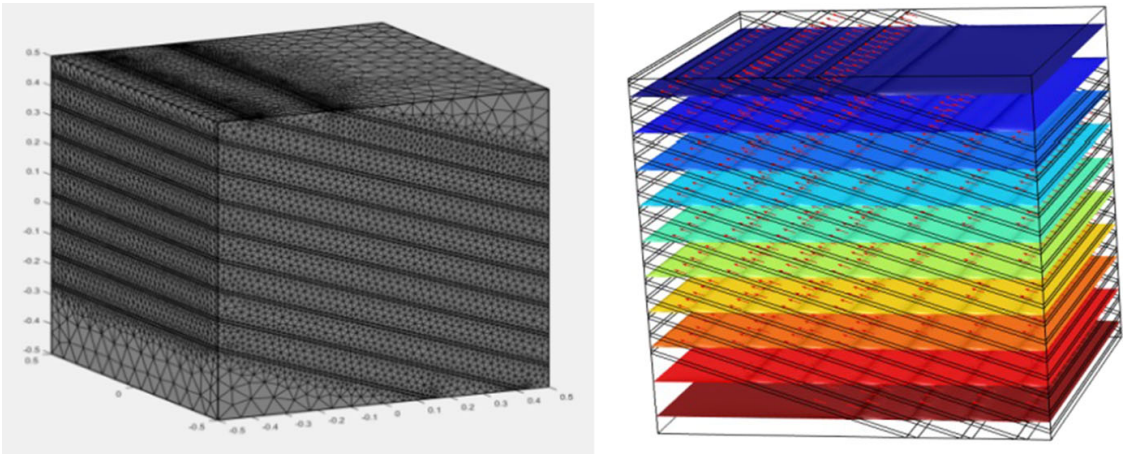

Fig. 7 Left: Finite element mesh of a fractured porous medium containing a set of inclined fractures. Right: results of a numerical flow simulation used for numerical upscaling for the same fracture set: iso-surfaces of piezometric heads and velocity vector arrows

agreement both in terms of norm and principal directions. As an example, it is shown in Table 1 the detailed results for a set of inclined fractures, depicted in Fig. 7, with $K_F = 0.1$ [m/s] and $K_M = 0.0001$ [m/s]). There is an excellent agreement between the superposition method and the numerical upscaling. The eigenvalues and eigenvectors of the equivalent conductivity tensor $\underline{\underline{K}}_{\text{EQ}}$ are also shown in the table, in order to verify that the superposition method is in agreement with the numerical upscaling for the full anisotropic conductivity tensor (The matrix $\underline{\underline{K}}_{\text{EQ}}$ is non-diagonal due to the inclined fractures).

Additionally, the results of numerical upscaling for different fracture densities have been analyzed. First, the equivalent $\underline{\underline{K}}_{\text{EQ}}$ tensor obtained either numerically or by superposition, is diagonalized. This serves several purposes: examining the eigenvalues and eigenvectors qualitatively, and also calculating the trace of the tensor. Because $\underline{\underline{K}}_{\text{EQ}}$ is symmetric definite positive, the trace of $\underline{\underline{K}}_{\text{EQ}}$ is equivalent to the Frobenius norm of the square root B of the matrix $\underline{\underline{K}}_{\text{EQ}}$ such that $BB^{\text{T}} = \underline{\underline{K}}_{\text{EQ}}$. More precisely, the square-root

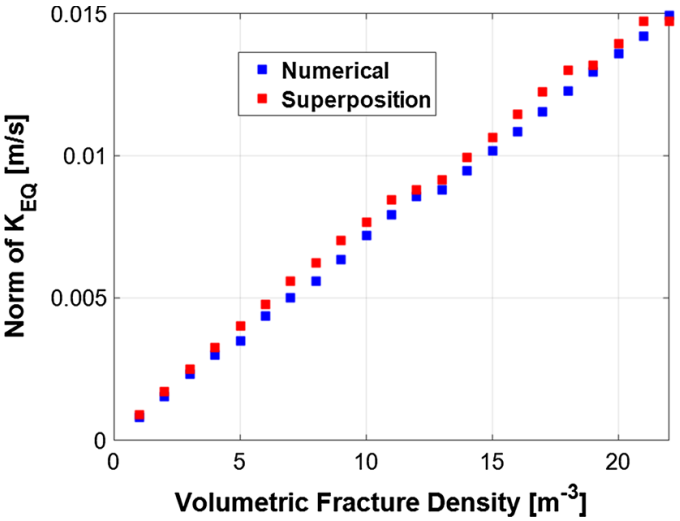

Fig. 8 Plot of the norm of equivalent hydraulic conductivity tensor, as a function of volumetric fracture density $\rho_{0,3}$ (blue symbols for the superposition method, red symbols for numerical upscaling)

matric B is given by $B = PD^{1/2}$ where P is the passage matrix containing column eigenvectors, and D is the diagonal eigenvalues matrix. Hereafter, the term "norm" of the conductivity tensors refers to the following expression

$$\|K\| = \left\| \begin{matrix} K^*_{xx} & 0 & 0 \\ 0 & K^*_{yy} & 0 \\ 0 & 0 & K^*_{zz} \end{matrix} \right\| = \frac{1}{3}(K^*_{xx} + K^*_{yy} + K^*_{zz}), \tag{19}$$

where the stars * refer to the principal components of $\underline{\underline{K}}_{\mathrm{EQ}}$.

Figure 8 shows the norm of the equivalent hydraulic conductivity tensor as function of the volumetric density of fractures $\rho_{0,3}$ [m^{-3}] for a three-dimensional Poissonian network with statistically isotropic orientation. The fractures in this figure are "infinite" (percolating fractures). The volumetric fracture density $\rho_{0,3}$ is defined as the number of fractures per unit volume ([number of fractures/m^3] or [m^{-3}]). As it can be seen in that plot, there is a good agreement between the equivalent hydraulic conductivities obtained by the superposition method and by numerical upscaling. A slight difference can be observed however, especially with high fracture densities, and it is generally attributed to numerical errors. The effect of the conductivity contrast (K_F/K_M) in the upscaling values has also been analyzed. Figure 9 shows the numerically upscaled and quasi-analytical (superposition) values of equivalent hydraulic conductivities for different fracture/matrix conductivity contrasts (from one to one million), for a three-dimensional Poissonian fracture network. The diameters in this case are larger than domain size ("infinite" fractures). Here, the density is $\rho_{0,3} = 20.0$ [m^{-3}].

Based on Fig. 9, it can be concluded that the superposition method yields a good estimation of the equivalent hydraulic conductivity of three-dimensional fracture networks with "infinite" fractures for different conductivity contrasts (K_F/K_M). This influence of the conductivity contrast can be important, because the matrix may contain finer fractures that are not seen explicitly, and hence, its permeability must not be neglected. These results confirm so far that the quasi-analytical superposition method is a correct method for upscaling "infinite" fractures regardless of their orientation

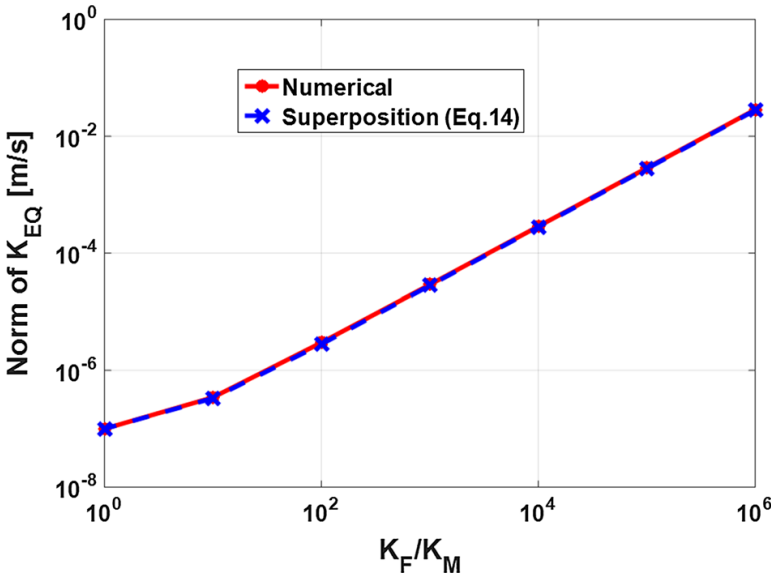

Fig. 9 Log-log plot of the norm of the equivalent hydraulic conductivity tensor as a function of the conductivity contrast (K_F/K_M) for the previous example

or aperture distributions, and without the need for detailed numerical solution of the matrix/fracture flow equations.

4.2 Extension to Finite Size Fractures

The aim of this section is to provide an expression based on the superposition method [i.e., an extension of Eq. (14)], in order to estimate the equivalent conductivity tensor for a large three-dimensional domain (the entire reservoir domain for example) containing only finite size "non-crossing fractures". The term "non-crossing fracture" refers to the case where the fracture diameter is not large enough (compared to the domain diameter) to connect two boundary faces of the parallelepipedic domain. However, depending also on fracture density, it is possible to obtain a percolating cluster formed by the intersection of several finite size "non-crossing" fractures. Generally, with finite size fractures, it is expected that connectivity effects are important for the equivalent hydraulic conductivity, and particularly when the fracture/matrix conductivity contrast (K_F/K_M) is high. In this subsection, the simulation results were obtained with the BIGFLOW code (unless indicated otherwise). Finally, it should be emphasized that only networks with Poissonian and isotropic spatial distributions are tested for the validation of the proposed extensions in this section and the next (Sect. 4.3).

4.2.1 Introduction to "Finite Size" Fracture Networks Characteristics (Critical Density and Percolation)

Our objective is to study connectivity effects by conducting numerical flow experiments in a finite fractured domain, with high conductivity contrast K_F/K_M. Under

these conditions, the hydraulically conductive medium is a network of "finite size"[6] planar disc fractures with negligible matrix permeability. In order to reduce border effects as much as possible, the fracture network has been preprocessed prior to flow experiments, by eliminating all the isolated fractures that intersect at least one edge or one corner of the three-dimensional parallelepipedic domain. This procedure eliminates any single isolated fracture connecting two or more boundary faces.

In this type of configuration (i.e., with a large computational domain containing only small size fractures), it is useful to consider a critical density $\rho_{EX,\boldsymbol{c}}$ by analogy with percolation theory. This quasi-percolation density, or critical density, can be defined, in general, as the fracture density above which the first cluster of fractures connecting two different boundary faces of the domain is formed (initiation of percolation). However, this "critical density" takes here a somewhat different meaning. Mathematical percolation theory deals with infinite domains, while here the computational domain is of finite size. In addition, percolation theory deals essentially with two possible types of conducting networks (site networks, and bond networks), while this work deals with planar disc conductors embedded in a three-dimensional porous matrix. Sahimi (1995) gives a review of percolation theory. Conduction and percolation in fractured media have been studied in Sahimi (1995), Berkowitz and Adler (1998), Mourzenko et al. (2005) and Adler et al. (2012), and others. Finite size effects on percolation phenomena were studied, more recently, by Adler et al. (2012). To sum up, the above-mentioned critical percolation density ($\rho_{EX,\boldsymbol{c}}$) can be a useful concept for extending the superposition method to finite size fracture networks. $\rho_{EX,C}$ will be defined more precisely below, and then it will be used it to take into account two different behaviors of the fractured medium, depending on fracture density. If the fracture density is less than the critical density, the fracture network is not percolating; it does not connect any two different boundary faces of the upscaling domain. If the fracture density is greater than the critical density, it exists one or several percolating clusters connecting two or more boundary faces of the upscaling domain. The use of this critical percolation density ($\rho_{EX,\boldsymbol{c}}$) in the new formulation of the superposition method will be explained below in Sects 4.2.2 and 4.3. Let us focus here on the definition of the appropriate density "ρ_{EX}" via the notion of "excluded volume". The excluded volume is defined, in the general case, as the averaged volume around one object within which a second object must have its center in order for the two objects to intersect (Charlaix et al. 1984). First the "excluded volume" $V_{EX,f}$ of a given fracture "f" is defined. The total excluded volume V_{EX} is then the sum $\Sigma V_{EX,f}$ calculated over all fractures ($f = 1,2,\ldots,N$). Finally, the fracture density "$\rho_{EX,C}$" is obtained by dividing V_{EX} by the volume V_{hom} of the upscaling domain: $\rho_{EX} = V_{EX}/V_{hom}$.

Let us focus now on determining the excluded volume $V_{EX,f}$ of a single fracture "f". The definition of the excluded volume can be illustrated more easily, as shown in Fig. 10, for the case of a set of fracture segments in two-dimensional space. The equivalent of an excluded volume in three dimensions is the excluded area in two dimensions. Fracture diameters in three dimensions are replaced by fracture lengths "L" in two dimensions, and the two orientation angles (θ,φ) in three dimensions are

[6] A *"finite size" fracture* is any planar fracture which does not entirely cross the upscaling domain: the opposite of "infinite sire" fracture mentioned in Sect. 2.

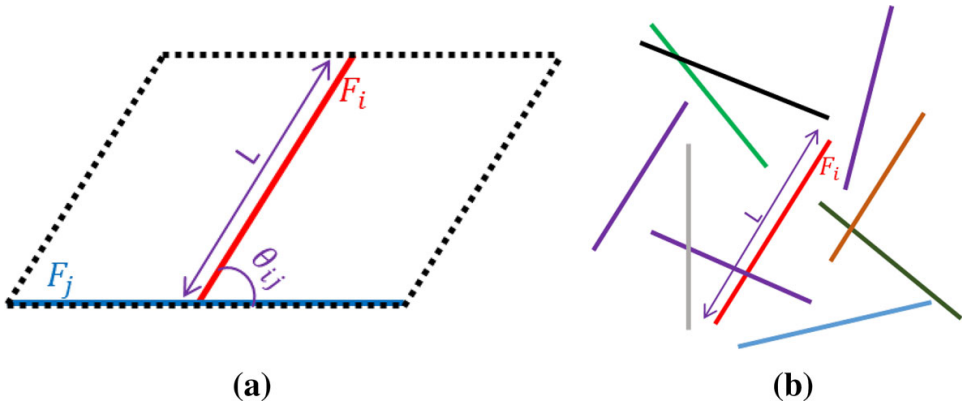

Fig. 10 **a** Representation of two arbitrary fracture segments and of their excluded area, delimited by the black dashed parallelogram (two-dimensional space). **b** Representation of a statistically isotropic network of fracture

replaced by the single angle (θ) in two dimensions. Figure 10a illustrates the calculation of the excluded area for a given fracture "F_i" with its given fracture length "L" and its given orientation θ_i. A second fracture segment F_j is selected, with its given length "L" and its given orientation θ_j. The relative orientation between the segments F_i and F_j is $\theta_{ij} = \theta_i - \theta_j$. The excluded area is obtained, as explained in Balberg et al. (1984), by translating the second segment F_j to all positions such that F_j intersect F_i (relative orientations are not changed). The resulting excluded area of the pair of fractures (F_i,F_j) is the area of the dotted parallelogram ($A_{EX} = L^2 \sin\theta_{ij}$) shown in Fig. 10a. A statistically isotropic network of fracture segments is now considered, with random angle θ uniformly distributed in [0, 2π] and deterministic length "L", as illustrated in Fig. 10b. The mean excluded area of this statistical network is calculated by averaging over all possible orientations θ_{ij} of the random fracture segments. The result, $A_{EX} = 2L^2/\pi$, was obtained by Balberg el al. (1984).

In three dimensions, Adler et al. (1999) studied the excluded volume of planar convex polygonal fractures,[7] each with a given area "A", a given perimeter "P", and orientation angles (Θ,Φ) defined by its normal. Let us consider two such fractures F_i and F_j, with their respective areas, perimeters, and angles. These two planar fractures have a relative angle "φ_{ij}" with respect to each other. Charlaix (1984) and Adler et al. (1999) obtained the excluded volume for two fractures of different sizes; in the special case where A and P are the same for the two fractures, the result is

$$V_{EX}(i, j) = \frac{2 \sin \varphi_{ij}}{\pi} AP. \tag{20.a}$$

For statistically isotropic networks in three dimensions, the average $<\sin \varphi_{ij}>$ is equal to $\pi/4$, and then, the mean excluded volume is

$$V_{EX} = \frac{1}{2} AP. \tag{20.b}$$

[7] The planar disc fractures studied in this work are a special limit form of planar convex polygons as the number of edges goes to infinity.

Finally, the last formula (Eq. 20.b) is used to calculate fracture by fracture the excluded volume, and then to deduce a dimensionless fracture density ρ_{EX} as follows

$$\begin{cases} V_{\mathrm{EX},f} = \frac{1}{2} A_f P_f \\ V_{\mathrm{EX}} = \sum_f V_{\mathrm{EX},f} \\ \rho_{\mathrm{EX}} = \frac{V_{\mathrm{EX}}}{V_{\mathrm{hom}}} \end{cases}, \tag{21}$$

where $\rho_{\mathrm{EX},C}$ is the dimensionless fracture density, V_{EX} and V_{hom} are respectively the total excluded volume of all the fractures, and the total volume of the homogenization domain (upscaling domain). It was demonstrated that for isotropic fracture networks, $\rho_{\mathrm{EX},C}$ is also equal to the mean number of intersections per fracture (Charlaix et al. 1984): this indicates the importance of $\rho_{\mathrm{EX},C}$ is a measure of the degree of connectivity of the fracture network. The critical excluded volume $V_{\mathrm{EX},C}$ is then defined as the excluded volume above which a percolating cluster appears. The corresponding critical percolation density $\rho_{\mathrm{EX},C}$ is finally computed as the critical excluded volume $V_{\mathrm{EX},C}$ divided by the total volume of the domain (Eq. 22)

$$\rho_{\mathrm{EX},C} = \frac{V_{\mathrm{EX},C}}{V_{\mathrm{hom}}}. \tag{22}$$

It is important to highlight here that the latter expressions of ρ_{EX} (Eq. 21) and of $\rho_{\mathrm{EX},C}$ (Eq. 22) are the same as the ones used by Mourzenko et al. (2005) where they found that $\rho_{\mathrm{EX},C}$ was not very sensitive to fracture size in predicting percolation. Finally, this dimensionless density $\rho_{\mathrm{EX},C}$ was found to be only "slightly" sensitive to the orientation distribution of the network in predicting percolation (Mourzenkou et al. 2009). After the presentation of the critical density $\rho_{\mathrm{EX},C}$ and other related quantities, the next part will explain how this critical density $\rho_{\mathrm{EX},C}$ has been numerically determined (Sect. 4.2.1), and how it was used for a new extension of the superposition method that can account for the degree of connectivity of the fracture set (Sect. 4.2.2).

4.2.2 Determination of the Critical Density

The critical density in this work is defined statistically and determined numerically because there are no theoretically exact methods allowing its unique determination in a finite fractured domain (again, recall that this work is not dealing with infinite domain percolation theory). The numerical procedure to determine the critical percolation density consists in conducting a series of numerical flow experiments for a single replicate of the fracture porous medium with increasing fracture density (and a fixed high contrast K_F/K_M). The different densities are obtained by adding fractures from a pre-set of random fractures: $N = 1000$ disc fractures are first generated, the number of fractures are, therefore, increased by sampling into this pre-set of 1000 random fractures. This numerical procedure is equivalent to generating several independent realizations of fractures sets. For instance, in a sequence of 1000 generated fractures, the first subset of 100 fractures is independent from the 2nd subset (fractures N°101 to N°200). The equivalent hydraulic conductivity is then determined for each density by numerical upscaling from the computed flow using CHBC. The critical "percolation"

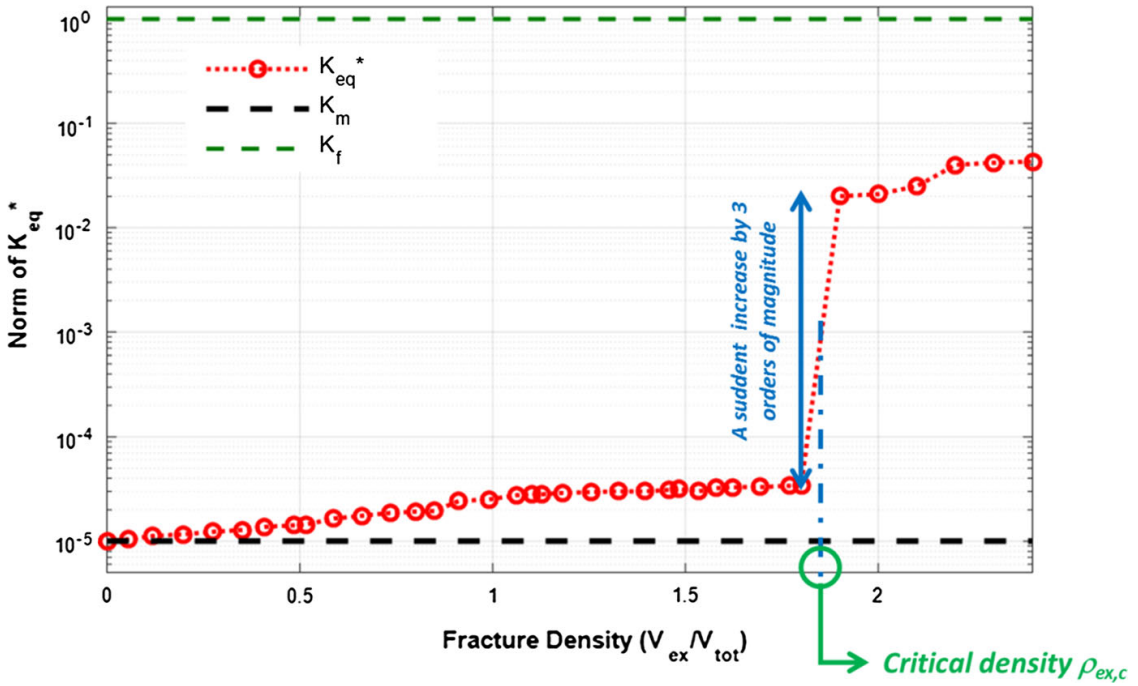

Fig. 11 Plot of $\underline{\underline{K}}_{EQ}$ (norm) as a function of fracture density (ρ_{EX}) for a single realization of a three-dimensional fracture network. A sudden jump of the norm of $\underline{\underline{K}}_{EQ}$ by 3 orders of magnitude is observed; the corresponding density to the jump is the critical density ($\rho_{EX,C}$)

density is detected by a sudden increase of the equivalent hydraulic conductivity with respect to density. The determination of $\rho_{EX,C}$ for a single realization of a three-dimensional fracture network is shown in Fig. 11.

To obtain values of $\rho_{EX,C}$ representative of the percolation behavior of three-dimensional fracture networks, multiple realizations of the network are generated, with constant fracture radius (non-random). For example, $N \times M = 30{,}000$ statistically independent planar disc fractures (isotropic Poissonian) are initially generated. Then, the $N \times M$ fractures are divided into $M = 30$ networks, each containing $N = 1000$ fractures. The previously described procedure to determine the critical density $\rho_{EX,C}$ is then applied to each of the 30 realizations. Finally, the "ensemble mean" critical density $E(\rho_{EX,C})$ is determined over the M realizations of the fracture network (Fig. 12). Note: from now on, the mean $E(\rho_{EX,C})$ will be denoted as "$\rho_{EX,C}$" for short.

As shown in Fig. 12, the mean critical density calculated by the previous procedure is $\rho_{EX,C} \approx 0.75$. However, Mourzenko et al. (2005) have shown that there exists a universal critical density, independent of fracture size: the critical density for disc fractures was found to be $\rho_{EX,C} = 2.31$. To understand this difference, other possible definitions of percolation can be considered. For example, a cluster is counted as "percolating" only if it relates two opposite boundary faces of the three-dimensional parallelepipedic domain. This definition corresponds physically to the application of PBC for the numerical determination of the equivalent hydraulic conductivity tensor. In that case (PBC), the obtained critical density values are found to be close to the value 2.31 obtained by Mourzenko et al. (2005). More specifically, a typical numerical simulation (with Comsol Multiphysics) with permeameter boundary conditions (PBC) is presented in Fig. 13, in which the permeable boundaries are only the top and bottom

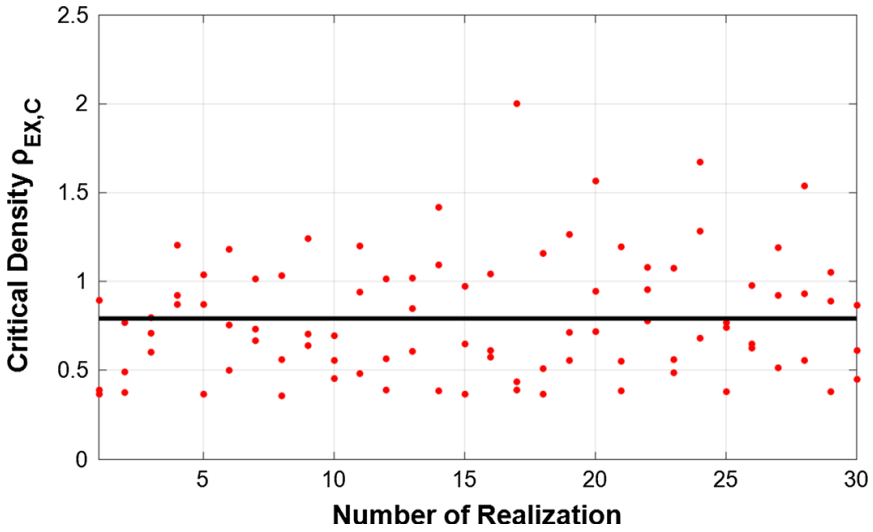

Fig. 12 Determination of the critical density of percolation ($\rho_{EX,C}$) over multiple realizations ($M = 30$). The ensemble mean value of $\rho_{EX,C}$ is retained as the final critical density of percolation. Here $\rho_{EX,C} \approx 0.75$

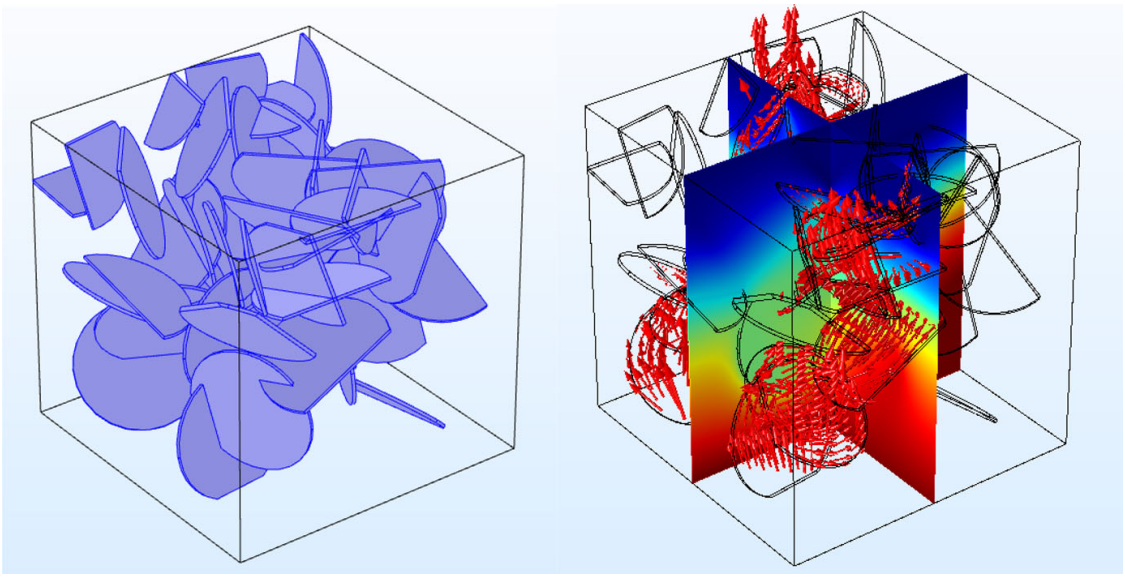

Fig. 13 Left: a 3D isotropic Poissonian fracture network with finite size fractures. Right: representation of the hydraulic head on selected planes (color shading) and of the Darcy velocity (arrows) simulated under PBC. The percolating cluster connects top and bottom faces of the domain

ones. It can be seen clearly, by observing the velocity field represented by arrows, that a percolating cluster of fractures relates the two opposite permeable sides. However, determining the critical percolation density using permeameter boundary conditions (PBC) seems to be very limiting because it considers only the largest clusters of fractures (i.e., the clusters connecting two opposite sides). In fact, other types of clusters can connect faces that are not necessarily opposed (Fig. 14 shows an example of a percolating cluster linking two adjacent sides of the three-dimensional domain). These types of clusters can be detected by using instead the "constant heads boundary conditions (CHBC)" as demonstrated in Fig. 14.

To illustrate these differences, concerning the definition of percolation and the types of boundary conditions, the same three-dimensional fracture network of Fig. 14 has

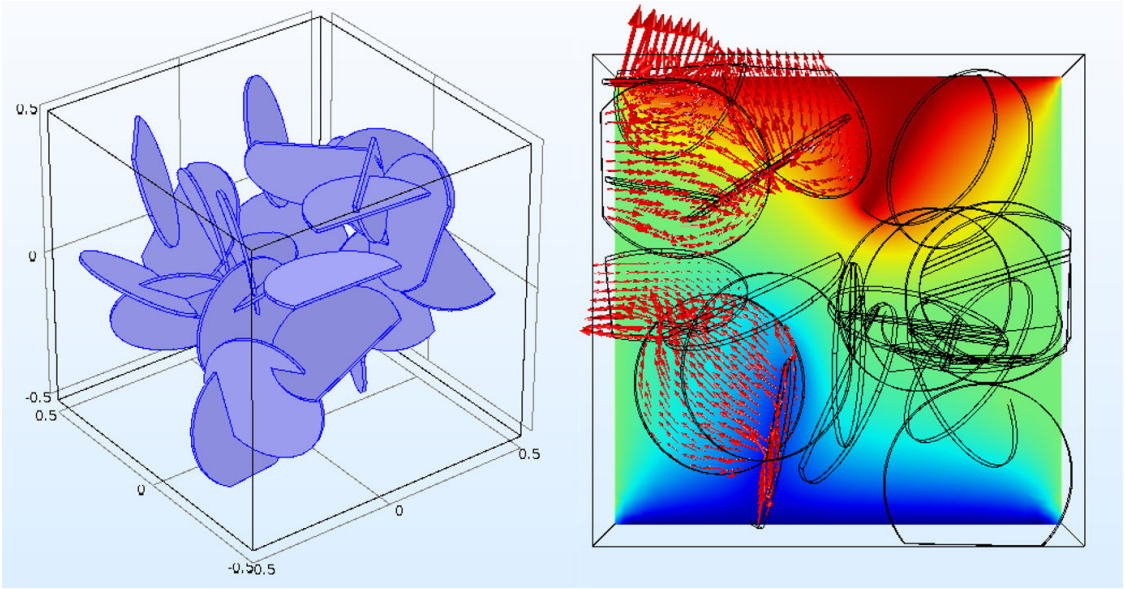

Fig. 14 Left: 3D isotropic network of Fig. 13. Right: an (*XY*) plane view of a detailed simulation on of flow under CHBC: hydraulic head (color shading) and the Darcy velocity (arrows). The percolating clusters are visible from the velocity field. The percolating clusters connect two adjacent faces

been re-used. The equivalent conductivity tensor has been determined numerically, for an increasing fracture density of this same network under two different types of boundary conditions: (1) PBC and (2) CHBC. The results are presented in Fig. 15. As explained before, percolation can be detected as a sudden increase of $\underline{\underline{K}}_{\mathrm{EQ}}$. The critical fracture density $\rho_{\mathrm{EX},C}$ was significantly different for the two boundary conditions $\rho_{\mathrm{EX},C} \approx 0.6$ for the CHBC, and $\rho_{\mathrm{EX},C} \approx 1.9$ for the PBC (Fig. 15). The example of Fig. 15 concerns a single realization of the three-dimensional fracture network. These observations confirm the fact that constant heads boundary conditions (CHBC) permit the detection of clusters relating any two boundaries of the domain, and therefore, percolation is observed early for non-opposite boundaries (small fracture density). On the other hand, permeameter boundary conditions (PBC) detect only the large clusters relating the two opposite faces of the domain, and therefore, percolation is detected at much larger densities (compared to CHBC).

The identification of the critical density of percolation is a relatively sensitive computational process, and the resulting critical density may be qualified itself as a random variable (over the ensemble of finite domain fracture networks of a given type). This uncertainty has been analyzed qualitatively in two ways:

1. How variable is the critical density $\rho_{\mathrm{EX},C}$?

As can be clearly seen from Fig. 16 (left), the degree of variability of the critical percolation density $\rho_{\mathrm{EX},C}$ is not negligible. This variability can be explained by the fact that percolation (under CHBC) can occur in different ways. For example, percolation can occur if two adjacent boundary faces are connected by a small cluster. This case will be the more frequent for "finite size" fractures (otherwise, percolation could also occur as the consequence of a larger cluster connecting two opposite faces). Hence, when one calculates the critical density, the corresponding critical number of fractures

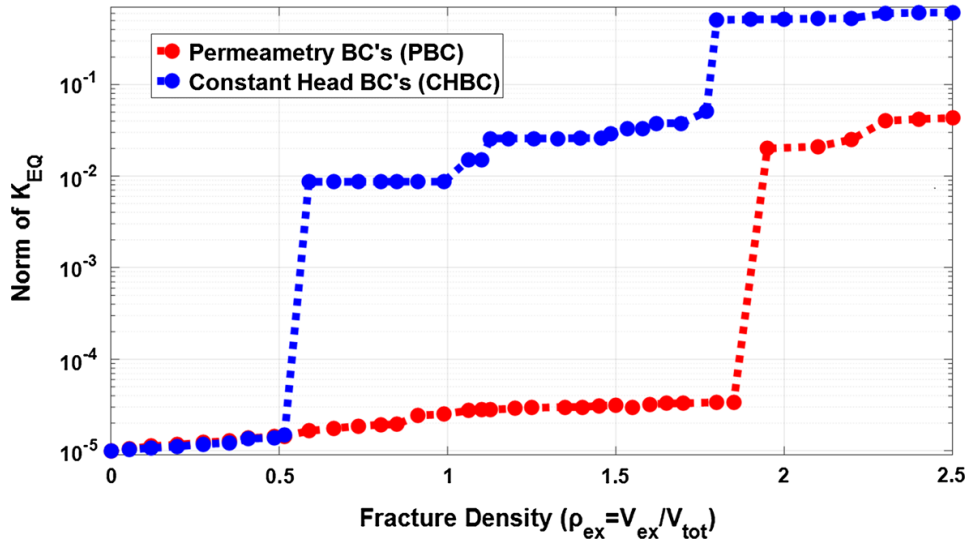

Fig. 15 Example of calculation of $\rho_{EX,C}$ by imposing PBC (red) and CHBC (blue). $\rho_{EX,C}$ corresponds to the density at which a sudden jump of the $\underline{\underline{K}}_{EQ}$ is observed (by 3 orders of magnitudes in this example). The resulting $\rho_{EX,C}$ are different for the two boundary conditions: 0.6 for CHBC and 1.9 for PBC

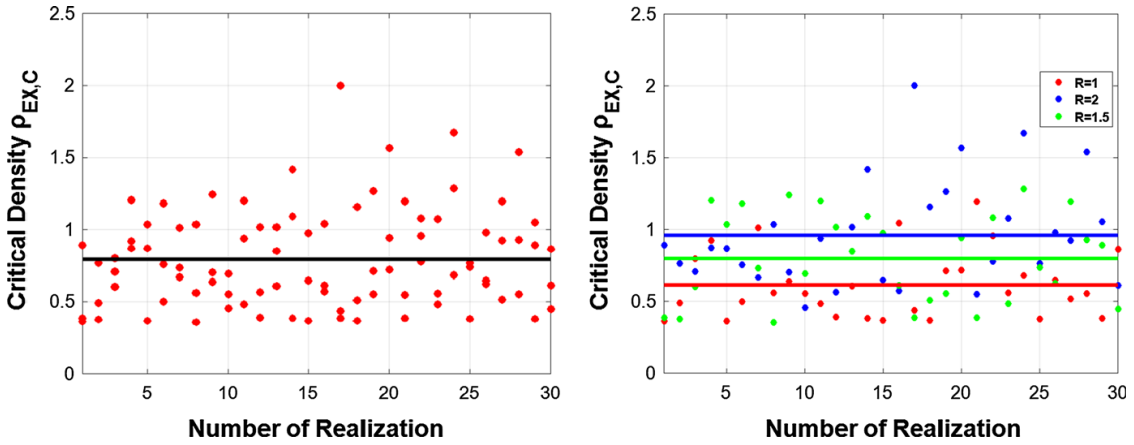

Fig. 16 Critical density ($\rho_{EX,C} = V_{EX,C}/V_{tot}$) for multiple realizations of a three-dimensional isotropic Poissonian fracture network. Left: all realizations combining the 3 radii $R = 1.0$, $R = 1.5$, $R = 2.0$ [m]. Right: same realizations grouped in three sets corresponding to the three fracture radii (with 3 different symbols for $R = 1.0$, $R = 1.5$, $R = 2.0$ [m])

is usually small, and, therefore, a high variability is expected across replicates of the network.

2. Does the critical density $\rho_{EX,C}$ depend on fracture radii?

Figure 16 (right) presents a qualitative analysis of the sensitivity of the critical density with respect to fracture size (radii). The results (Fig. 16 right) were obtained by performing, for different fracture radii, the same procedure for determining $\rho_{EX,C}$ as described earlier at the beginning of this section (Sect. 4.2.2). It can be seen that the critical density increases with fracture radius. This dependence was not revealed on the previously cited results found in the literature, where the critical density of percolation $\rho_{EX,C}$ is stated to be a universal quantity, independent of fracture size distribution (Mourzenko et al. 2005). This size sensitivity is not studied further in the present work; and this topic is kept as a perspective for future investigations. Finally, in the

remainder of this paper, the critical density is assumed to be the mean value obtained from all the realizations in the present work. In conclusion, the critical density to be retained here is found to be $\rho_{EX,C} \approx 0.75$.

4.2.3 Extension of the Superposition Formula for Finite Size Fractures

As mentioned earlier, the hydraulic behavior of the fracture network is radically dependent on the fracture density when fracture diameters are significantly smaller than domain diameter (finite size fractures). Therefore, the critical percolation density ($\rho_{EX,C}$) should play a significant role in the estimation of equivalent hydraulic conductivity. More precisely, it was seen that the increase of fracture density ρ_{EX} does not drastically affect the equivalent hydraulic conductivity as long as fracture density remains smaller than $\rho_{EX,C}$ because, at low density, fractures do not yet form a percolating cluster. When ρ_{EX} reaches the critical density $\rho_{EX,C}$, a percolating cluster of fractures is formed. The increase of fracture density beyond this critical value increases the equivalent conductivity. The fast superposition method, as implemented so far, did not include this critical hydraulic behavior. For this reason, a novel semi-empirical superposition formula is proposed, which would be able to handle a set of finite size fractures for a broad range of fracture density and connectivity. This proposed formula is based on the critical percolation density ($\rho_{EX,C}$) defined in Sect. 4.2.1.

The "fast superposition method" is accordingly modified and extended as follows: for density ρ_{EX} below the critical percolation density ($\rho_{EX,C}$), the fractures do not form percolating clusters. The superposition method is therefore modified to compute the equivalent hydraulic conductivity $\underline{\underline{K}}_{EQ}$ as a harmonic mean over all mono-fracture blocks. This harmonic averaging procedure permits to take into account the hydraulic conductivity of the porous matrix, particularly for non-percolating fracture sets. For density ρ_{EX} over the critical percolation threshold ($\rho_{EX,C}$), a numerical fit between the equivalent hydraulic tensor obtained by numerical upscaling and the one obtained by the initial superposition method of Eq. (14) has been performed, over a large range of fracture densities. Finally a semi-empirical analytical expression for $\underline{\underline{K}}_{EQ}$ is obtained, where the critical density plays an important role.

The procedure is implemented following three steps:

1. First, the equivalent $\underline{\underline{K}}_{EQ}$, tensor obtained either numerically or by superposition, is diagonalized as explained earlier (below Table 1).
2. Then, a search (by a fitting procedure) of an empirical correction factor $f(\rho_{EX})$ that can calibrate the superposition method for densities ρ_{EX} larger than the critical density $\rho_{EX,C}$ is performed. A linear relation is proposed for the empirical correction factor $f(\rho_{EX})$ by

$$f(\rho_{ex}) = \frac{\|K_{\text{numerical}}\|}{\|K_{\text{superposition}}\|} = A\rho_{ex} = 0.68\rho_{ex}, \tag{23}$$

where the fitting was performed by linear regression over a large range of fracture densities (Fig. 17). The result of this linear regression was of the form

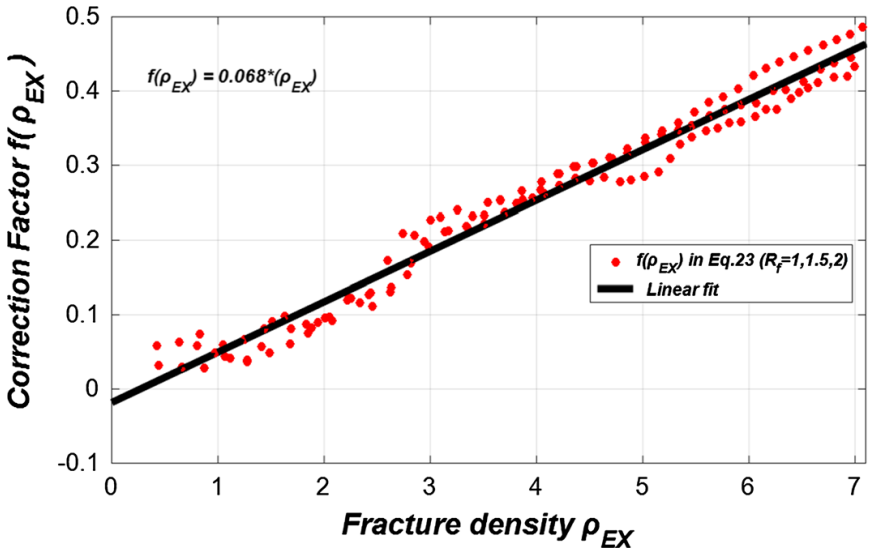

Fig. 17 Linear fit of the correction factor $f(\rho_{\mathrm{EX}})$ as a function of fracture density ρ_{EX}. The linear behavior of $f(\rho_{\mathrm{EX}})$ is roughly the same for different fracture radii ($R = 1.0$ m, 1.5 m, 2.0 m). Determination factor: $R^2 = 0.97$

$$f = AX + B \quad \text{with } B \approx 0. \tag{24}$$

The determination factor is $R^2 = 0.97$, which yields a relative root mean square error $\varepsilon = sqrt(1–R^2) = 0.173$ or 17.3%. This fitting was performed over fracture sets having different fracture radii (constant within each set). It was observed clearly that the correction factor $f(\rho_{\mathrm{EX}})$ depends linearly on fracture density ρ_{EX} in a unique way for all fracture radii (Fig. 17). This confers a "generic" character to the correction factor. In other words, the proposed semi-empirical correction factor is relatively robust. It is worth to note that the linear dependence of $f(\rho_{\mathrm{EX}})$ was observed only for the range of densities studied here

$$0 \leq \rho_{\mathrm{ex}} = \frac{V_{\mathrm{ex}}}{V_{\mathrm{tot}}} \leq 7. \tag{25}$$

Although bounded, this range of density is still relatively large, because it goes from very poorly connected networks to well-connected networks. Larger fracture densities would need more computational capacities and are not studied here.

3. Finally, the "*extended*" fast superposition expression is, therefore, reformulated (for finite size fractures) as

$$\underline{\underline{K_{\mathrm{EQ}}}} = f(\rho_{\mathrm{ex}}) \sum_{f=1}^{f=N_f} \Phi_{\mathrm{bloc}} \underline{\underline{Rot_f}}\, \underline{\underline{K_{\mathrm{bloc}}}}\, \underline{\underline{Rot_f^t}} \quad \text{if } \rho_{\mathrm{ex}} \geq \rho_{\mathrm{ex},c}$$

$$\underline{\underline{K_{\mathrm{EQ}}}} = \left\{ \sum_{f=1}^{f=N_f} \left(\Phi_{\mathrm{bloc}} \underline{\underline{Rot_f}}\, \underline{\underline{K_{\mathrm{bloc}}}}\, \underline{\underline{Rot_f^t}} \right)^{-1} \right\}^{-1} \quad \text{if } \rho_{\mathrm{ex}} < \rho_{\mathrm{ex},c}, \tag{26}$$

where N_f is the total number of fractures in the homogenization domain.

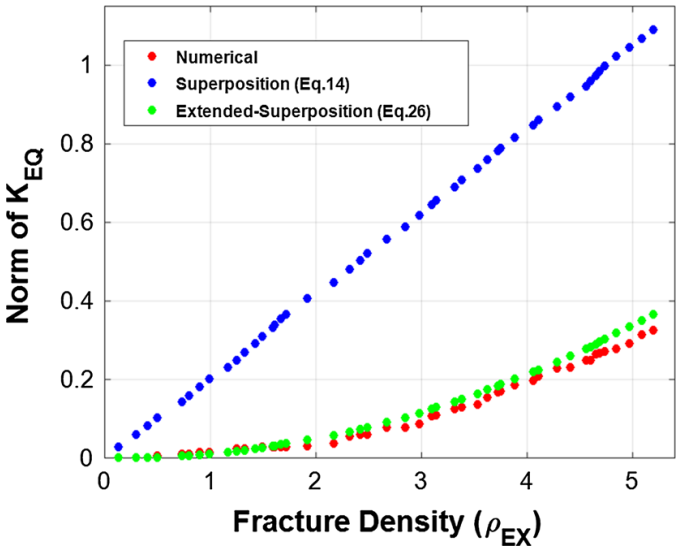

Fig. 18 Comparison of the results of the equivalent hydraulic conductivity as function of the dimensionless fracture density ρ_{EX}. Numerical upscaling (red), initial superposition method of Eq. (14) (blue), and extended superposition method of Eq. (26) (green)

The validity of the above "extended" expression of the superposition method is tested for Poissonian fracture network with isotropic orientation in three dimensions. The size distribution follows a truncated Pareto distribution with lower and upper bound radii, $R_{\min} = 0.5$ m and $R_{\max} = 2.5$ m, respectively. The domain size is $10 \times 10 \times 10\,[\mathrm{m}^3]$; therefore, even the largest fractures are significantly smaller than domain size. The results (Fig. 18) show the relevance of the proposed extended superposition model (Eq. 26) for the range of fracture density studied. The upscaled conductivity results from Eq. (26) represent a very clear improvement of the method compared to the initial version given by Eq. (14). The errors E_1 and E_2 for both superposition methods (the initial version, and the new *extended* version) have been calculated. The errors are calculated as the mean absolute difference between the norm of $\underline{\underline{K}}_{\mathrm{EQ}}$ of reference (obtained numerically) and the $\underline{\underline{K}}_{\mathrm{EQ}}$ calculated by the superposition method. Error E_1 corresponds to the initial superposition method (Eq. 14) and E_2 corresponds to the extended superposition (Eq. 26). Here, the errors are $E_1 = 0.140\ K_F$ and $E_2 = 0.019\ K_F$. The error of the extended method is about seven times smaller than the initial superposition method, for finite non-percolating fractures. Plotting the same results with a logarithmic scale for equivalent conductivity (Fig. 19) allows appreciating the jump in hydraulic conductivity due to the percolation effect on equivalent conductivity. It occurs at a density of 0.51 for the numerical upscaling, and 0.75 for the extended superposition method (Eq. 26). This difference is probably due to the uncertainty on the determination of the critical percolation density, as discussed earlier (Sect. 4.2.2).

4.3 Extension to Mixed Type Networks (Broad Distribution of Fractures Radii)

This section treats a more realistic representation of the porous fractured rock, where both "infinite" and finite size fractures are present. More precisely, the fracture network contains at the same time two types of fractures. The first type of fracture intersects at least two different boundary faces of the homogenization domain, typically, large diameter fractures or faults (labelled "CB" for "connecting boundaries"). The second type of fracture does not connect more than one boundary face of the homogeniza-

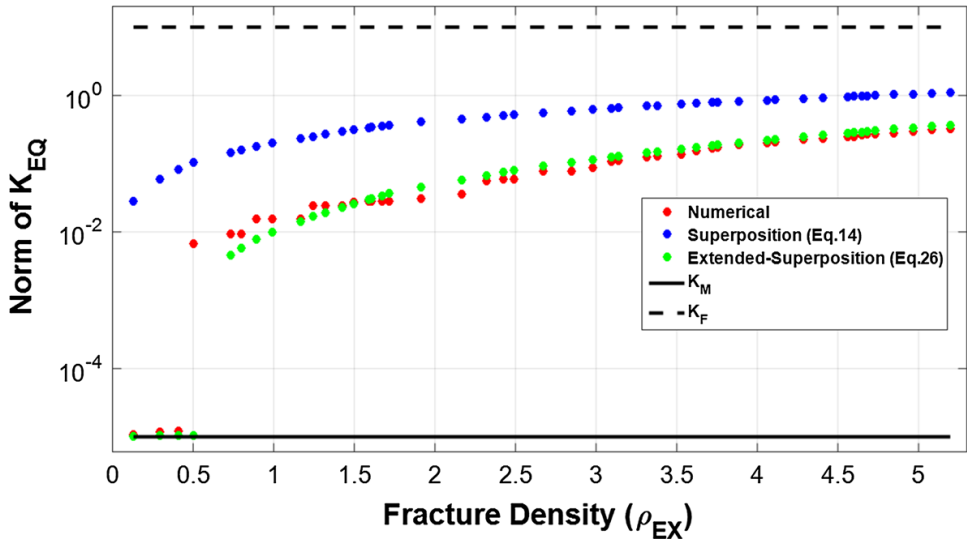

Fig. 19 Semi-log representation of the norm of the equivalent conductivity tensor, as a function of dimensionless fracture density: numerical (red symbols), initial superposition method (blue symbols) and extended superposition method (green symbols). For comparison, matrix and fracture conductivities are also shown: the solid curve represents K_M (matrix conductivity) and the dashed curve represents K_F (fracture conductivity)

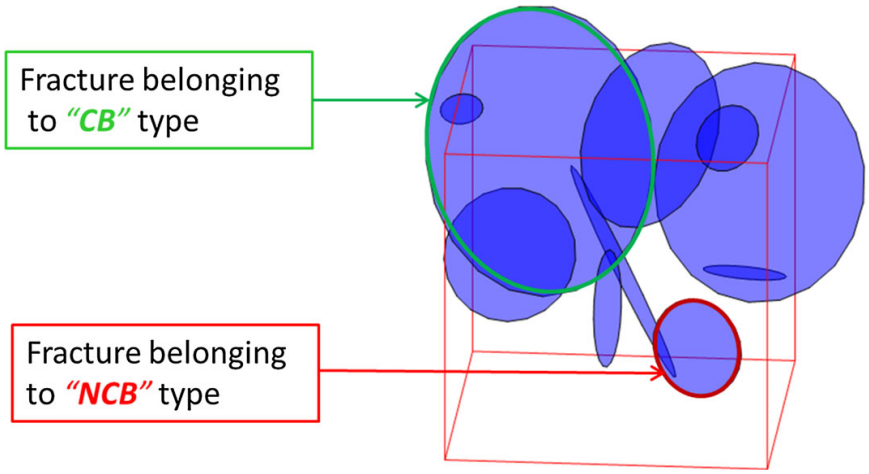

Fig. 20 Representation of the two types of fractures in a mixed network. The red cube is the homogenization domain. The large green fracture belongs to the "CB" type, and its crossing index is $C_f = 3$. The smaller red fracture belongs to the "NCB" type, and its crossing index is $C_f = 0$

tion domain; this includes fractures that do not intersect any boundary at all (this second type is labelled "NCB" for "non-connecting boundaries"). A crossing bounds index, "C_f" is introduced. For each fracture f, "C_f" is the number of intersections of fracture "f" with the boundaries of the homogenization domain. Since the domain is parallelepipedic, "C_f" is a number between 0 and 6 for each fracture. Figure 20 is a schematic representation of the distinction between the two types of fractures ("CB" and "NCB"). The union of CB and NCB constitutes the complete set of fractures.

The aim of this section is to propose a new extended version of the superposition method that can also handle this type of mixed configuration. The new extension works as follows. In the case of a CB fracture ($C_f \geq 2$), this fracture is added to

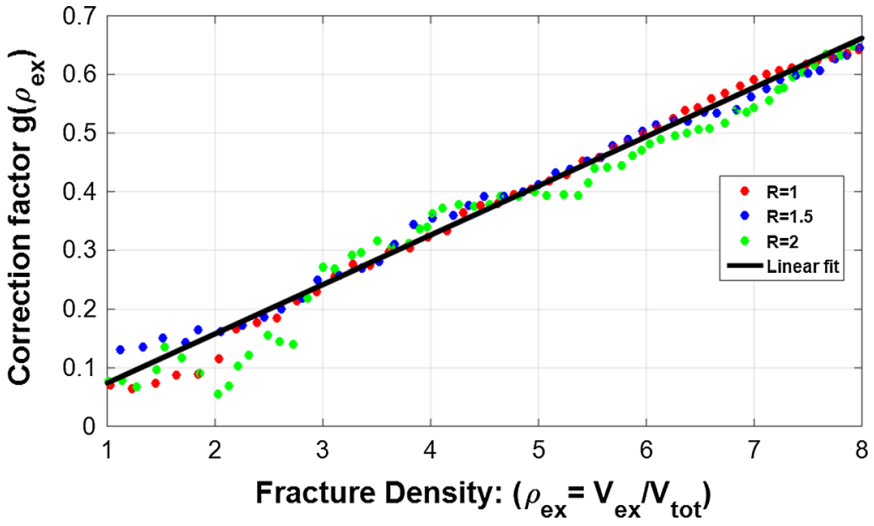

Fig. 21 Plot of $g(\rho_{\mathrm{EX}})$ as a function of the density ρ_{EX}. The linear behavior of $g\ (\rho_{\mathrm{EX}})$ is nearly the same for three different fracture radii: $R=1.0$, $R=1.5$, $R=2.0$ [m]. The determination coefficient is $R^2=0.965$

the superposition algorithm (without any correction factor). In the case of a NCB fracture ($C_f \leq 1$), this fracture is added to the superposition algorithm multiplied by a correction factor $f(\rho_{\mathrm{EX}})$ obtained empirically in a manner similar to Sect. 4.2.3. The new correction factor $f(\rho_{\mathrm{EX}})$ is defined, taking into account differently the CB and NCB type fractures, as follows

$$\left\|K_{\mathrm{EQ}}\right\| = \|K_{\mathrm{CB}}\| + f(\rho_{\mathrm{ex}})\,\|K_{\mathrm{NCB}}\| \Rightarrow f(\rho_{\mathrm{ex}}) = \frac{\left\|K_{\mathrm{EQ}}\right\| - \|K_{\mathrm{CB}}\|}{\|K_{\mathrm{NCB}}\|}, \tag{27}$$

where K_{CB} and K_{NCB} are, respectively, the equivalent conductivity tensor of the "CB" fractures and of "NCB" fractures, respectively, and $\underline{\underline{K}}_{\mathrm{EQ}}$ is the equivalent conductivity tensor of the entire fracture network. Let us now define another connectivity index "$\rho_{EX,NCB}$" (Eq. 28), which represents the connectivity between the non-crossing fractures (NCB),

$$\rho_{\mathrm{ex,NCB}} = \frac{V_{\mathrm{ex,NCB}}}{V_{\mathrm{tot}}}, \tag{28}$$

where $V_{\mathrm{EX,NCB}}$ is the excluded volume of the "NCB" subset of fractures. The former correction factor of Eq. (27) divided by $(\rho_{\mathrm{EX,NCB}})^2$ as a function of ρ_{EX}, plotted in Fig. 21, is given by

$$g(\rho_{\mathrm{ex}}) = \frac{f(\rho_{\mathrm{ex}})}{(\rho_{\mathrm{ex,NCB}})^2} = A\rho_{\mathrm{ex}} + B. \tag{29}$$

A linear behavior is observed for all the fracture sizes studied here, and this is confirmed by a linear regression fit, as shown in Fig. 21. The relative independence of this linear fit with respect to fracture radius confers a generic character to this linear fit. It is relatively robust, and it can be applied with confidence to various fracture radius distributions, at least in the range of radii investigated here (from 1/10 to 1/5 the size

of the homogenization domain). Hence, the final extended superposition expression for the equivalent conductivity tensor that takes into account the two types of fractures "CB" and "NCB" is

$$\underline{\underline{K_{\mathrm{EQ}}}}(\rho_{\mathrm{ex}}) = \sum_{f=1}^{f=N_{\mathrm{CB}}} \Phi_{\mathrm{bloc}}\, \underline{\underline{Rot_f}}\, \underline{\underline{K_{\mathrm{bloc},f}}}\, \underline{\underline{Rot_f^t}} + g(\rho_{\mathrm{ex}})\,.\,(\rho_{\mathrm{ex,NCB}})^2\,.\, \sum_{f=1}^{f=N_{\mathrm{NCB}}} \Phi_{\mathrm{bloc}}\, \underline{\underline{Rot_f}}\, \underline{\underline{K_{\mathrm{bloc},f}}}\, \underline{\underline{Rot_f}}^t, \tag{30}$$

where N_{CB} and N_{NCB} are the number of fractures in the homogenization domain belonging respectively to "CB" and "NCB" types (as shown in Fig. 20), and g($\rho_{\mathbf{ex}}$) is a correction factor that depends linearly on fracture density $\rho_{\mathbf{ex}}$, and finally, $\rho_{\mathrm{ex,NCB}}$ is the density of the subset of NCB fractures that do not intersect more than one boundary face.

In order to validate Eq. (30), a three-dimensional fracture network with Poissonian distribution of fracture position and with isotropic orientation has been chosen. The radius distribution is a truncated Pareto law with $R_{\mathrm{min}} = 0.5$ [m] and $R_{\mathrm{max}} = 3$ [m]. The domain of homogenization is a parallelepiped of size $10 \times 10 \times 10$ [m]. The results (Fig. 22) demonstrate a clear improvement in comparison with the initial superposition method (Eq. 14) for the whole range of fracture density studied. The extended superposition method (Eq. 30) predicts the equivalent conductivity tensor with considerable accuracy, at least in terms of its norm. The errors E_1 and E_2 are calculated for both superposition methods: the initial version (Eq. 14), and the new extended version (Eq. 26). The errors are $E_1 = 0.16\ K_F$ for the initial version of the superposition method, and $E_2 = 0.02\ K_F$ for the extended version. Here, the extended method (Eq. 30) yields an error 8 times smaller than the initial superposition method, for a mixed type of network with both percolating and non-percolating fractures.

Finally, it was observed that the typical computation time to obtain the equivalent conductivity tensor $\underline{\underline{K_{\mathrm{EQ}}}}$ by the quasi-analytical superposition method of the synthetic samples studied in this paper (all samples evoked in Sect. 4) was only a few seconds. In comparison, to obtain $\underline{\underline{K_{\mathrm{EQ}}}}$ numerically (by direct simulations and numerical upscaling), the typical computation time was of the order of 30 min. Furthermore, direct numerical simulations are very limiting in practice: (i) the meshing procedure can fail if fracture aperture is very small, and (ii) the CPU time for solving very large algebraic systems may become impractical (typically, the three-dimensional grids may have to involve hundreds of millions of cells).

5 Conclusions

In this paper, a computationally efficient superposition method for upscaling the hydraulic conductivity of a three-dimensional porous and fractured rock sample is proposed. The proposed superposition method is used without recourse to detailed flow simulations except for connectivity and critical density calculations.

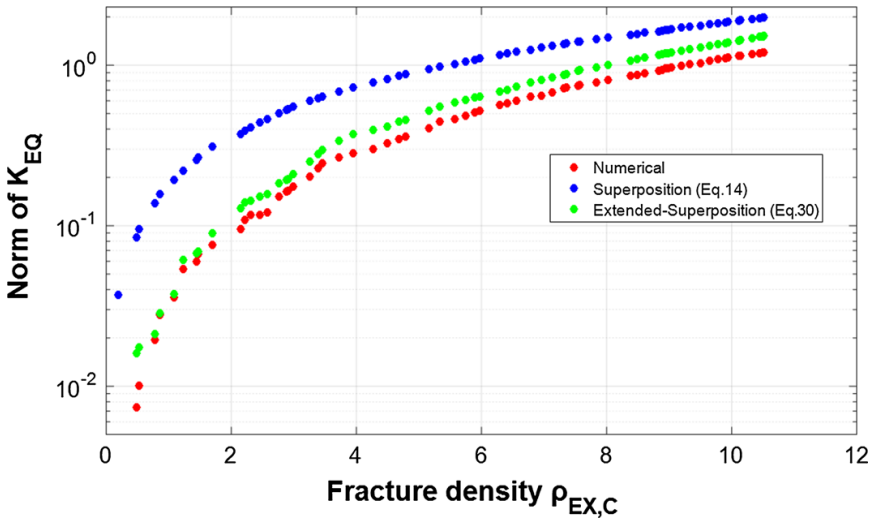

Fig. 22 Semi-log representation of the equivalent hydraulic conductivity norm as a function of the dimensionless fracture density ρ_{EX}. Numerical (red), original superposition method (Eq. 14) (blue) and extended superposition method (Eq. 30) (green)

The superposition method presented in this paper is based on a flux superposition method (Ababou et al. 2011), which was a useful and efficient upscaling tool, but had several limitations: (i) it did not explicitly formulate the conductivity as a volume weighted combination of fracture/matrix conductivities; (ii) the approximate flux superposition yields essentially a weighted arithmetic mean conductivity tensor; and (iii) it did not take into account the connectivity of the fracture network. This initial upscaling method is improved as follows: (i) the volumetric contributions of each mono-fracture block are now explicitly taken into account; (ii) in the case of non-percolating network, the initial superposition is replaced by a volumetric weighted harmonic mean of mono-fracture blocks; and (iii) semi-empirical connectivity factors are introduced as a function of fracture density and of a critical percolation density. This improved upscaling method yields a three-dimensional tensorial equivalent conductivity $\underline{\underline{K}}_{\mathrm{EQ}}$, which represents hydraulically the fractured porous rock as an equivalent continuum. The present upscaling method only requires, for its implementation, the geometry of the fractures (diameters, orientations, and apertures from probabilistic models or fracture set data), and the hydraulic conductivities of the fractures K_F and of the surrounding porous matrix K_M. In addition, approximate connectivity indexes had to be determined semi-empirically by linear regression from numerical flow experiments. These indexes improved the upscaling method for different types of fracture networks embedded in a porous matrix.

For validation and verification of the upscaling by this enhanced superposition method, detailed flow simulations were implemented on a parallelepiped domain (millions of cells). Our numerical upscaling was based on the volume averaged flux as an equivalence criterion, and on particular boundary conditions called CHBC (constant heads boundary conditions), which has been compared to other boundary conditions.

Numerical upscaling, which is computationally demanding, yields an equivalent conductivity tensor to be compared to the faster superposition methods.

Promising results were obtained for the equivalent hydraulic conductivities calculated by the new superposition method in this paper (Sect. 4), for different configurations of fracture networks. The results were in good agreement with those obtained numerically for different fracture radius distributions. Also, these results were obtained for a wide range of hydraulic conductivity contrasts K_F/K_M in the case of "infinite" fractures. On the other hand, for finite size fractures or mixed networks, our study focused on very high K_F/K_M contrasts, and this, for various configurations in terms of fracture sizes and density of Poissonian isotropic networks. Overall, the new *extended* methods (Eqs. 26, 30) yield an absolute error (E_2) seven to eight times smaller than the error (E_1) of the initial superposition method (Eq. 14), relative to the numerically upscaled conductivity used as the reference.

In summary, our partially validated superposition method provides a computationally efficient algorithm for determining the equivalent continuum hydraulic conductivity tensor for a three-dimensional sample of porous fractured rock. This equivalent tensor serves as input for reservoir flow simulation on larger scales in deep geologic formations like geothermal reservoirs.

Several issues remain worth investigating based on the progress results presented in this paper (ongoing work). The main issues are: (i) a more accurate statistical determination of the critical percolation density $\rho_{\mathrm{EX},\boldsymbol{c}}$ (its sensitivity to fracture diameters, and its variability across replicates of random networks); (ii) investigation of denser fracture networks (limited due to computational capacities); and finally, (iii) unifying into a single formulation the various subcases of the new superposition method with its semi-empirical density-dependent factors (finite/infinite fracture diameters; percolating/non-percolating networks; etc.).

Acknowledgements The first three authors wish to acknowledge the financial support of ADEME (France) in the framework of the GEOTREF project "GÉOThermie haute Énergie en REservoirs Fracturés" (www.geotref.org). We thank the anonymous reviewers for their careful reading of the manuscript and for their insightful comments and suggestions.

References

Ababou R (1990) Identification of effective conductivity tensor in randomly heterogeneous and stratified aquifers. In: Bachu S (ed) Proceedings Fifth Canadian–American conference on hydrogeology: parameter identification and estimation for aquifers and reservoirs, Calgary, Alberta, Canada, Sep. 18–20, 1990. Nat. Water Well Assoc., Water Well Journal Publish. Co., Dublin, Ohio, 1990, pp 155-157

Ababou R, Bagtzoglou AC(1993) BIGFLOW: a numerical code for simulating flow in variably saturated, heterogeneous geologic media (theory & user's manual, Version 1.1). Report NUREG/CR-6028, U.S. Nuclear Regul. Commission, Gov. Printing Office, Washington, DC

Ababou R., Renard P (2011) Equivalent permeability tensor in fractured media: an algebraic approach. In: Amaziane B, Barrera D, Mraoui H, Rodriguez ML, Sbibih D (eds) Proceedings MAMERN11: 4th internat. conf. on approx. methods and numer. model. in envir. and natur. resour. (Saïdia, Morocco, May 23–26, 2011). Univ. Granada (2011), ISBN: 078-84-338-5230-4, 2011

Ababou R, McLaughlin D, Gelhar LW, Tompson AF (1989) Numerical simulation of three-dimensional saturated flow in randomly heterogeneous porous media. Transp Porous Media 4(6):549–565

Ababou R, Millard A, Treille E, Durin M, Plas F (1994) Continuum modeling of coupled thermo-hydro-mechanical processes in fractured rock. In: Peters XA et al (eds) Computational methods in water resources. Kluwer Academic Publishers, Netherlands, pp 651–658

Ababou R, Cañamón Valera I, Poutrel A (2011) Macro-permeability distribution and anisotropy in a 3D Fissured and fractured clay rock: 'Excavation Damaged Zone' around a cylindrical drift in Callovo-Oxfordian Argilite (Bure). J Phys Chem Earth (Spec. Issue "Clays in Natural & Engineer. Barriers for Radioact. Waste Confin.": CLAYS 2010, Nantes, 29 March–1st April 2010). 36(17–18):1932–1948. ISSN 1474-7065. https://doi.org/10.1016/j.pce.2011.07.032

Adler PM, Thovert J-F (1999) Fractures and fracture networks. Kluwer Academic Publishers, Dordrecht

Adler PM, Thovert J-F, Mourzenko VV (2012) Fractured porous media. Oxford University Press, Oxford

Balberg I, Anderson CH, Alexander S, Wagner N (1984) Excluded volume and its relation to the onset of percolation. Phys Rev B 30:3933

Bamberger A (1977) Approximation des coefficients d'opérateurs elliptiques, stables pour la G-convergence. Rapport du Centre de mathématiques appliquées, École polytechnique, n° MAP/15

Berkowitz B, Adler PM (1998) Stereological analysis of fracture network structure in geological formations. J Geophys Res [Solid Earth] 103:15339–15360

Bouwer H (1969) Planning and interpreting soil permeability measurements. J Irrig Drain Div, ASCE 95:391–402

Brown SR (1987) Fluid flow through rock joints: the effect of surface roughness. J Geophys Res 92(B2):1337–1347. https://doi.org/10.1029/JB092iB02p01337

Budiansky B (1965) On the elastic moduli of some heterogeneous materials. J Mech Phys Solids 13:223

Cañamón I (2006) Analysis and modeling of coupled thermo-hydro-mechanical phenomena in three-dimensional fractured media. PhD thesis, Institut National Polytech. de Toulouse & Univ. Politécnica de Madrid

Cardwell WT, Parsons RL (1945) Average permeabilities of heterogeneous oil sands. Trans Am Inst Mining Metall Pet Eng 160:34–42

Charlaix E, Guyon E, Rivier N (1984) A criterion for percolation threshold in a random array of plates. Solid State Commun 50(11):999–1002

Dagan G (1979) Models of groundwater flow in statistically heterogeneous porous formations. Water Resour Res 15(1):47–63

Desbarats AJ (1992) Spatial averaging of hydraulic conductivity in three-dimensional heterogeneous porous media. Math Geol 24(3):249–267

Deutsch C (1989) Calculating effective absolute permeability in sandstone/shale sequences. SPE Form Eval 4:343–348

Dimitrakopoulos R, Desbarats AJ (1997) Geostatistical modelling of grid block permeabilities for 3D reservoir simulators. SPE Reservoir Eng 8:13–18

Farmer CL (2002) Upscaling: a review. Int J Numer Meth Fluids 40:63–78

Hashin Z, Shtrikman S (1963) A variational approach to the theory of elastic behaviour of multiphase materials. J Mech Phys Solid 11:127–140. https://doi.org/10.1016/0022-5096(63)90060-7

Journel AG, Deutsch, C, Debarats AJ (1986) Power averaging for block effective permeability: SPE 15128, presented at the 56th California Regeonal Meeting of the SPE, Oakland, California, April 2–4, 1986

Kfoury M, Ababou R, Noetinger B, Quintard M (2006) Upscaling fractured heterogeneous media: permeability and mass exchange coefficient. J Appl Mech (JAM), Trans ASME 73(1):41–46

Kiraly L (1969) Anisotropie et hétérogénéité de la perméabilité dans les calcaires fissurés. Eclogae Geol Helv 62(2):613–619

Lang PS, Paluszny A, Zimmerman RW (2014) Permeability tensor of three-dimensional fractured porous rock and a comparison to trace map predictions. J Geophys Res Solid Earth 119:6288–6307. https://doi.org/10.1002/2014JB011027

Le Loc'h, G (1988) An efficient strategy for combining the permeabilities: practical application on a simulated reservoir. In: Proc. of the 3rd internat. Geostatistics congress, Avignon, Sept 5–9

Li L, Zhou H, Gómez-Hernández JJ (2011) A comparative study of three dimensional hydraulic conductivity upscaling at the macro-dispersion experiment (MADE) site, Columbus Air Force Base, Mississippi (USA). J Hydrol 404:278–293. https://doi.org/10.1016/j.jhydrol.2011.05.001

Long JCS, Remer JS, Wilson CR, Witherspoon PA (1982) Porous media equivalents for networks of discontinuous fractures. Water Resour Res 18(3):645–658

Marchant.J (1977) Sur la résistance équivalente d'un réseau aléatoire de structure irrégulière. CR Acad Sci Paris, t.284, Série B-85:88

Matheron G (1967) Eléments pour une Théorie des Milieux Poreux. Masson et Cie, Paris, p 166
Mourzenko VV, Thovert JF, Adler PM (2005) Percolation of three-dimensional fracture networks with power-law size distribution. Phys Rev E 72:036103
Mourzenko V, Thovert J-F, Adler PM (2009) Proceedings of the international conference on rock joints and jointed rock masses, Tucson, Arizona
Oda M (1985) Permeability tensor for discontinuous rock masses. Géotechnique 35(4):483–495. https://doi.org/10.1680/geot.1985.35.4.483
Oda M (1986) An equivalent continuum model for coupled stress and fluid flow analysis in jointed rock masses. Water Resour Res 22(13):1845–1856
Pouya A, Fouché O (2009) Permeability of 3D discontinuity networks: new tensors from boundary-conditioned homogenization. Adv Water Resour 32:303–314
Pozdniakov S, Tsang C-F (2004) A self-consistent approach for calculating the effective hydraulic conductivity of a binary, heterogeneous medium. Water Resour Res 40:W05105. https://doi.org/10.1029/2003WR002617
Renard P, de Marsily G (1997) Calculating equivalent permeability: A review. Adv Water Resour 20:253–278
Renard P, Ababou R (2009) Relation between the definition and properties of the equivalent permeability tensor in heterogeneous and fractured porous media. In: Amaziane B et al (eds) Proceedings MAMERN 09: 3rd international conference on approximation methods and numerical modeling in environment and natural resources (Pau, France, 8–11 June 2009), Editorial Univ. de Granada, ISBN: 978-84-338-5006-5
Renard Ph, Le Loc'h G, Ledoux E, de Marsily G, Mackay R (2000) A fast algorithm for the estimation of the equivalent hydraulic conductivity of heterogeneous porous media. Water Resour Res 36(12):3567–3580
Sævik PN, Berre I, Jakobsen M, Lien M (2013) A 3D computational study of effective medium methods applied to fractured media. Transp Porous Media 100(1):115–142
Sahimi M (1995) Flow and transport in porous media and fractured rock. VCH, New York
Snow DT (1969) Anisotropic permeability of fractured media. Water Resour Res 5(6):1273–1289
Tsang YW (1984) The effect of tortuosity on fluid flow through a single fracture. Water Resour Res 20:1209–1215
Vanmarcke E (1983) Random fields (analysis and synthesis). The MIT Press, Cambridge
Warren JE, Price HS (1961) Flow in heterogeneous porous media. Soc Pet Eng J 1:153–169
Wen XH, Gomez-Hernandez JJ (1996) Upscaling hydraulic conductivities in heterogeneous media: an overview. J Hydrol 183:ix–xxxii
Wiener O (1912) Abh. Math.-Phys. Klasse Königlich Sächsischen Des Wiss. Leipzig 32:509–604
Zinn B, Harvey CF (2003) When good statistical models of aquifer heterogeneity go bad: a comparison of flow, dispersion, and mass transfer in connected and multivariate Gaussian hydraulic conductivity fields. Water Resour Res 39(3):1051. https://doi.org/10.1029/2001WR001146

2.3 Conclusion

This is an extended conclusion to the paper by Rajeh et al. (2019)[2]. A fast upscaling approach based on the superposition principal is presented in this chapter. The proposed approach presents an important improvement for this type of methods. The connectivity of the fracture network is taken into account, in the superposition formulation, by multiplicative connectivity factors. These connectivity factors are determined empirically from direct numerical simulation over various fractured porous synthetic samples. Although these improvements, the superposition method still have strong limitations. The main two limitations are related to two main issues: (i) the detection of percolation and (ii) the connectivity of the fracture network.

Firstly, concerning the percolation detection, the method used in the previous work is based totally on detailed flow simulations on the 3D fractured media. For the determination of the fracture density, one has to add fracture by fracture to the 3D media and run detailed flow simulation, for each iteration, until percolation. This methodology is computationally very expensive and it is limited to low number of fractures in the DFN (1,500 fractures was the maximum number of fractures treated in the previous paper). Hence, due to the computational cost, the percolation detection was limited to several realizations of the network.

Secondly, concerning the fracture network connectivity, the presented method is about a general estimation of the number of intersections per fracture. Similar to the percolation detection, the connectivity factor determination needs numerous detailed flow simulations in 3D fractured media rendering this task very computationally expensive. Moreover, the presented method is incapable of determining detailed interconnections analysis of the networks: one cannot have insightful details about the connection between all the fractures in the DFN.

Aware of these limitations and willing to improve our capabilities of treating more dense and more connected 3D fracture networks, a set of numerical tools for geometrical and topological analysis of DFN have been developed (the toolbox is in continuous improvement and extension of its capabilities). The two previous issues (percolation and connectivity) present the initial motivation to the development of the tools although more important applications can be derived from it. The set of the geometrical and topological tools are presented in details in the following chapter 3 and their uses regarding percolation, connectivity and upscaling are presented in chapter 4.

[2]Erratum. Equation EQ.2 in the paper represents the Hashin and Shtrikman (HS) bounds in the one dimensional case (1D). Hence, the general formula (for 1D, 2D and 3D) is obtained by replacing "$1 - f_0$" by "$m - f_0$" and "$1 - f_1$" by "$m - f_1$" in equation (EQ.2) where "m" is the dimension of space (m=1 for 1D, m=2 in 2D and m=3 in 3D).

Chapter 3

Topological Analysis of 3D Fracture Networks

3.1 Introduction

It can be understood from the previous chapters that fractures form the principal pathway for flow in subsurface rocks with low matrix permeability. Using the discrete fracture network (DFN) approach is the most accurate method to simulate flow and transport in 3D fracture networks as it incorporates explicitly all the attributes of 3D planar fractures (aperture, size, permeability etc.). However, the DFN approach is numerically very expensive (in terms of CPU time and memory). As an example, [Karra et al. (2018)] presented some computational capabilities of a recently developed DFN flow simulation tools. In their work, they presented a DFN containing 7,147 fractures of moderate density. The corresponding mesh of this DFN contains 15,178,277 elements and the CPU time for meshing operations is about 81,392 [s] (nearly a 1 day). The CPU times reported in [Karra et al. (2018)] correspond to runs with 1 processor on a 32 core, 2 thread per core, AMD Opteron(TM) Processor 6,272 with 528 GB RAM. One can note that the DFN of about 7,000 fractures is a very moderate network compared to real case applications. Additionally, for quantifying uncertainty, through a probabilistic approach of the DFN, hundreds of realizations of the DFN may have to be run. Hence, the DFN approach is generally limited to moderate (in term of density) fracture networks.

The DFN approach has been studied since 2 decades [Adler et al. (2012)]. The approach was quickly found to be very limited due to computational capacities even with the increasing of calculation power of modern computers. To increase the efficiency of the DFN approach, important efforts have been devoted recently in improving DFN meshing ([Fourno et al. (2019)] [Hyman et al. (2014)] among others). Recently, a graph approach was used as an alternative to simulate larger DFN [Karra et al. (2018)]. However, approximations have to be made which reduce the accuracy of the DFN approach. There is an increased need for frameworks capable of handling 3D DFN and extracting the exact percolating clusters with the appropriate calculations of intersections and traces lengths. [Huseby et al. (1997)] was among the first to propose such algorithmic methodology for 3D fracture networks. Recently, [Alghalandis (2017)], [Hyman et al. (2017)], separately proposed a set of algorithms enabling this analysis in 2D and 3D configurations and have constructed the equivalent graph of the DFN.

Motivated by the necessity of effecient tools to assess percolation and connectivity of the 3D fracture networks (as explained in the conclusion of the previous chapter), we propose

in this chapter a complete algorithmic approach to pre-treat the 3D fracture network in order to determine and analyze all its geometrical and topological features. It is worthy to note, at this stage, that all the 3D fracture networks treated in the present chapter are formed by 3D planar fractures with two shapes, discs and ellipses. The present set of algorithms is capable of (i) calculating all possible intersections in the 3D network, lengths of the resulting traces, fracture areas inside a parallelipipedic domain and other geometrical attributes of the DFN, (ii) extracting the percolating clusters and eliminating dead end clusters and (iii) constructing the corresponding graph of the 3D fracture networks. These three aspects are detailed in separate sections of this chapter. A flowchart describing the organization of the proposed tools is given in Fig.(3.1).

All the analytical calculations implemented in the algorithms have been validated by various methods including direct numerical simulations, which increases the confidence in our algorithm methodology. Additionally, examples of important applications (other than the study of percolation and connectivity phenomena, which were the main initial motivations for this work) are briefly mentioned in each part of the algorithms.

The present chapter is organized as follows based on the three major aspects of our algorithmic approach. Firstly (Sect.1), the algorithms to calculate analytical intersections, areas and traces lengths are described. These calculations allow the construction of the Adjacency matrix (to be defined later) of the DFN. The set of algorithms of this section are called, hereafter, "Connectivity Algorithms". Secondly, original methods for cluster identification, percolating clusters extraction and dead-end clusters eliminations are explained in Sect.2. The set of algorithms of the second section are called, hereafter, "Clustering Algorithms". Thirdly, the construction of the corresponding graph of the DFN is depicted in Sect.3. The set of algorithms of the third section are called, hereafter, "Graph Algorithms".

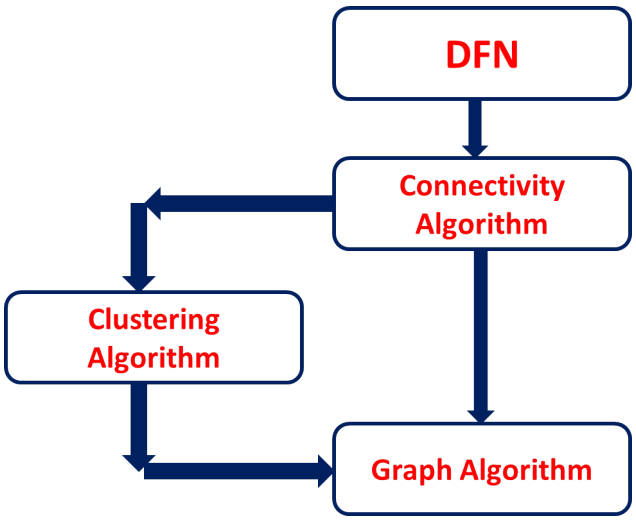

Figure 3.1: Flowchart of the topological analysis of DFN. The hierarchy of the algorithms is indicated by directed arrows.

3.2 Connectivity of 3D fracture networks

3.2.1 Description of the connectivity algorithms

The method developed in this part, denoted the "Connectivity algorithm", is organized as follows. The starting point is a DFN file. For example, a fracture network generated stochastically (as adopted in the present work) or generated by any other generation method, as explained in chapter1, presents the input to this set of algorithms. To perform the geometrical analysis of the DFN, the algorithm uses the geometrical attributes of the fractures constituting the DFN as an input (location, size, orientation etc.) and calculates (i) areas of the circular or elliptical planar fractures intersecting a 3D parallelipipedic domain, (ii) all the possible intersections between any pair of fractures in the network , (iii) lengths of the intersecting traces 'Tij' and the coordinates of the middle points (Nodes) of the traces, and finally (iv) the adjacency matrix FF of the DFN which is a square matrix of the size of the number of fractures N_F where $FF(i,j) = 1$ indicates that fracture F_i intersects fracture F_i and $FF(i,j) = 0$ indicates that the two fractures do not intersect.

At first, a domain have to be chosen (e.g., the interior cubic domain with black frame, shown in Fig.(3.2)). In a DFN with N planar fractures, there are $N(N-1)/2$ possible intersections. Intersections with boundaries are taken into account in the algorithm by adding explicitly the six faces of the parallelipipedic domain. To reduce the computational time (reminder: the number of operations is proportional to the square of the number of fractures) and for efficiency gain, a filtering procedure has been performed at first. This filtering has been implemented on three levels.

1. First filtering level: all fractures whose circumscribed sphere does not intersect the 3D domain are eliminated from the searching list of fractures. For example, fractures F_{20} and F_9 are eliminated from the search by this exclusion test (Fig.(3.2)).

2. Second filtering level: if the distance from the center of fracture F_i to the plane of fracture F_j is bigger than fracture F_i radius or vice versa, then the fracture pair formed by F_i and F_j is eliminated from the search. For example, in Fig.(3.2), the pair of fractures formed by F_{13} and F_2 is eliminated from the search by this exclusion test.

3. Third filtering level: if fracture F_i plane intersects the fracture F_j but fracture F_i is completely outside the sphere containing fracture F_j, then the pair (F_i, F_j) is eliminated from the search. For example, in Figure 3.2, the pair of fractures(F_5, F_{11}) is eliminated from the search by this exclusion test.

This preliminary filtering is computationally fast but does not account for all non-intersecting fractures. A more explicit calculation of the intersections is then performed over the remaining fractures. To obtain the adjacency matrix, the follwing six main steps have to be realized (for seek of clarity, the details of calculations of steps 1, 2, 3 and 4 are not presented and only the important elements are highlighted):

- Step1. The intersection line L_{ij} of the two planes containing the two fractures F_i and F_j is calculated. The straight line L_{ij} is obtained by solving the following system of equations in the local frame of fracture F_i

$$\begin{cases} ax + by + cz + d = 0 \\ z = 0 \end{cases} \tag{3.1}$$

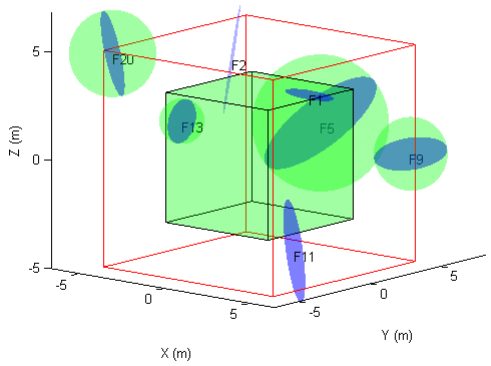

Figure 3.2: Example of filtering tests. The parellilepipedic domain is the inner black cube. Fractures are in blue and their circumscribed spheres are presented in green.

where a, b, c, d are the coefficients of the plane containing fracture F_j, expressed in the local coordinate frame of fracture F_i.

- Step2: the intersection points of the two fractures F_i and F_j with line L_{ij} are calculated by solving the following system of equations in the local frame of fractures F_i and F_j respectively:

$$\begin{cases} x = -(d + by)/a \\ y = \left(-bd \pm \sqrt{b^2d^2 - e(d^2 - a^2R_{F_i}^2)}\right)/e \\ z = 0 \end{cases} \tag{3.2}$$

where $e = (a^2 + b^2)$ for circular fractures and $R_{F_i}$is the radius of fracture F_i. Note that parameters a, b, c, d, e are geometrical coefficients containing fracture coordinates and orientations and the ellipsoidal shape factor (ratio of large to small radii). There are up to four solutions $(x, y, 0)$ to Eq. (3.2).

- Step3: Only the case with 4 real solutions of the previous system of equations (Eq. (3.2)) provides possible intersections. In all other cases, the two fractures do not intersect. In the case of four real solutions, the relative positions of the four intersection points $(P1, P2, P3, P4)$ determine whether the two fractures intersect or not (Fig.(3.3)). If intersection occurs, the length of the corresponding trace T_{ij} is then calculated.

- Step4: Once all the traces of fracture-fracture intersections are calculated, the total area of fractures intersecting the 3D domain is computed (The resulting contour of a fracture inside the 3D cubic domain contains either discs or convex polygons with both straight and/or curved sides). Straight sides are the intersections of the fracture with the boundaries of the domain, and curved sides are parts of the fracture border inside the domain. In the case of elliptical fractures, intersecting area is computed

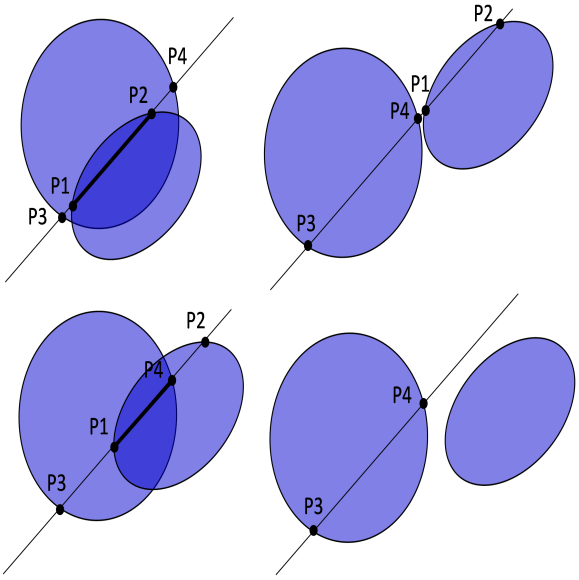

Figure 3.3: All possible configurations of the fractures regarding their intersection.

by means of the affinity relation between the area of an ellipse and its circumscribed circle.

- Step5: The adjacency matrix (also called Fracture-Fracture matrix FF) is finally constructed. In graph theory, an adjacency matrix is a square matrix used to represent a finite graph. The elements of the matrix are zeros and ones, indicating whether pairs of vertices (fractures) are adjacent or not (intersecting or not) in the graph. $FF(i,j) = 0$ indicates that fractures F_i and F_j do not intersect.

- Step6: Given the adjacency matrix and the results of traces calculations, other topological matrices are derived. We present here the most two important ones for the sake of clarity. (i) The first one is the trace to trace matrix (TT) in which the value of one means that two traces T_i and T_j are connected by a fracture and a zero value means that T_i and T_j are not connected directly. The second important matrix is the Link to Trace matrix (LT). In each line i of LT matrix there are only two values different from zero indicating that the two traces (T_i and T_j) correspond to the link (L_i). The TT matrix is square, and its size is the number of traces in the 3D DFN. Example of such traces can be seen in Fig.(3.3): the pair of nodes $(P1, P2)$ in the upper left, and $(P1, P4)$ in the lower left of the figure.

The main outputs of the Connectivity algorithms are illustrated on a simple illustrative example in Fig.(3.4). In this example, a DFN composed of five fractures generated randomly in a 3D domain of size $10 \times 10 \times 10[m]$ is presented. The principal outputs of the Connectivity algorithm are depicted. Algorithm.(1) illustrates in a simplified manner the geometrical analysis of the DFN. This algorithm was developed using vectorization and pointers in Matlab (without "for" loops). The "worst case" computational cost of this algorithm in terms of CPU time is $T_{CPU} \propto N^2/2$ where N is the total number of fractures of the network. Briefly, this worst case estimate is obtained by the following argument:

the worst case scenario is where any fracture is connected to all the remaining fractures in the network. Hence, N^2 intersection calculations are needed. However, if F_i and F_j intersection is calculated at a given step, then the intersection calculations for F_j and F_i is not necessary and hence the division by 2 in the previous estimation of the CPU time.

Algorithm 1 Connectivity Algorithm

Load the DFN with N fractures

Initializing Adjacency matrix: FF=0

Preliminary Filtering: N←number of remaining fractures

For i=1 to N

  Calculate the area inside the domain

  For j= i +1 to N

    Perform intersection steps (1, 2, 3, 4)

    Perform step 5: if F_i intersect F_j then $FF(i, j) = 1$

  End for

End for

Fill in the output matrices

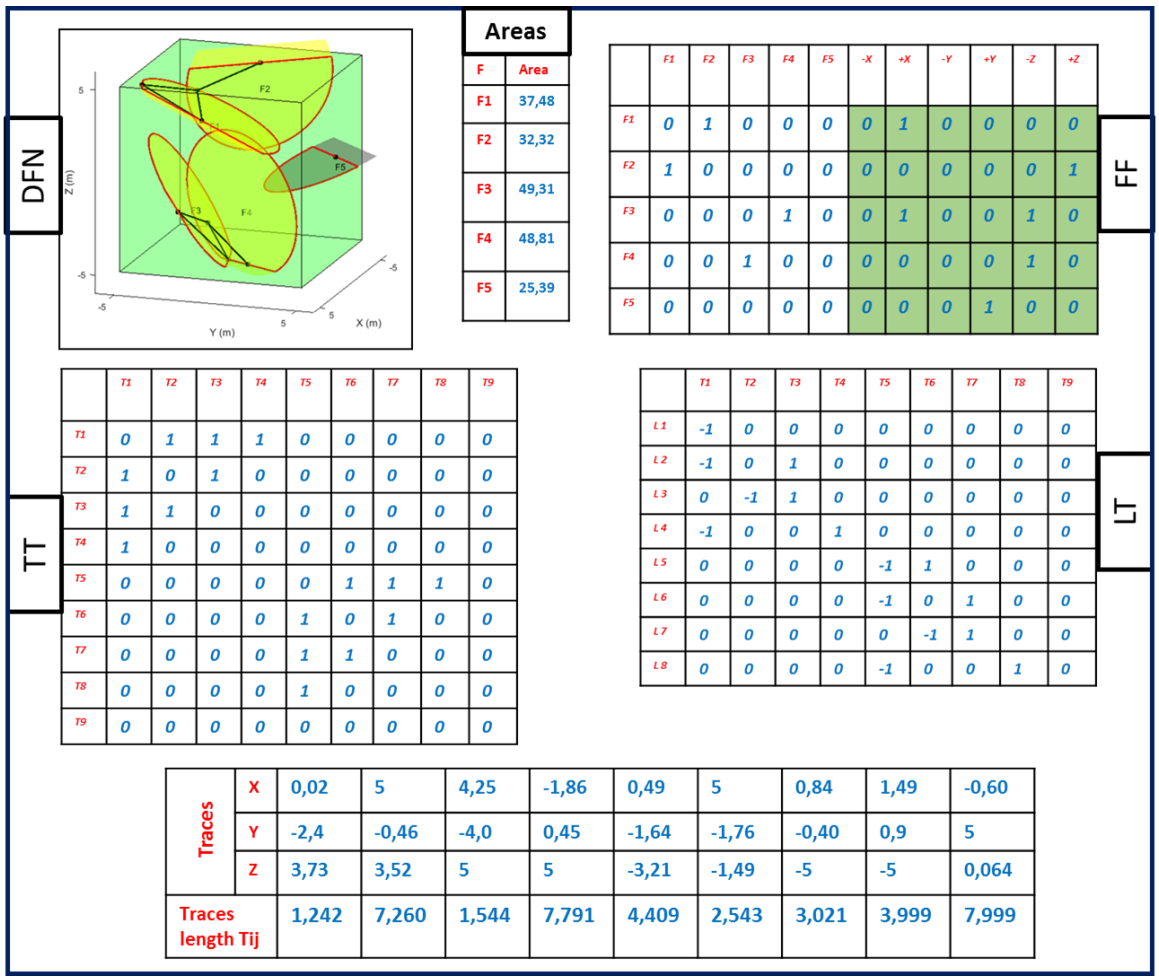

Figure 3.4: Output of the Connectivity Algorithm: the DFN containing five fractures, the adajacency matrix (FF), the trace-to-trace matrix (TT), the links-to-traces matrix (LT), the traces mid-points coordinates (T) and the traces vector (T_{ij})

3.2.2 Validation and numerical performance of the connectivity algorithm

3.2.2.1 Validation of the connectivity algorithm

The aim of this section is to perform a series of validation tests to verify the correctness and the accuracy of the developed algorithmic methods in predicting the geometrical and/or the topological properties of a DFN. Although all the mathematical relations implemented in the Connectivity Algorithm are based on analytical solutions (except an approximate relationship for the calculation of the perimeter of ellipses), the validation is always necessary in such algorithmic approaches. Once validated, the outputs of the Connectivity Algorithms can be used, with high degree of confidence, as inputs to the Clustering and Graph algorithms (next sections 3.3 and 3.4). Specifically, geometrical calculations of intersections (nodes) and trace lengths are of great importance as they are the building blocks of the next algorithms.

This task has been performed over a large variety of examples with increasing complexity. To validate the proposed algorithm, a numerical platform has been elaborated based on a combination of the commercial software Comsol Multiphysics and Matlab. The comparison between the results of the Connectivity Algorithm and the results of the software Comsol Multiphysics constitutes a benchmark test. It is worthy to note at this stage that the software Comsol Multiphysics is usually used as a simulation toolbox; here only its "Geometry" module is used for this benchmark.

The general idea behind validation is as follows: upon a variety of DFN, several topological properties like "nodes", "traces lengths", etc. are calculated at first by the Connectivity Algorithm and then verified numerically by Comsol Multiphysics. For the sake of clarity, we choose to show two relevant examples of validations concerning the correctness of calculation of nodes and traces lengths.

As mentioned in the description of the Connectivity Algorithm, the fracture intersections and trace lengths (T_{ij}) are determined analytically and then implemented in the algorithm. To verify the precision of the analytical calculations (intersections, traces and areas) and the correctness of their algorithmic implementation, we have performed a comparison with numerical calculations upon meshed geometry in Comsol Multiphysics. A typical result of comparison is presented in Fig.(3.5). For a network of N=30 fractures, the intersections (nodes) and the traces lengths have been determined by the two methods; firstly by the analytical method implemented in algorithm and secondly by the exact numerical calculations by Comsol Multiphysics. The results of ComsolMultiphysics are taken here as reference. As it can be clearly seen from Fig.(3.5), the Connectivity Algorithm detects any intersection in the DFN and calculates exactly the correct trace length. For the sake of completeness, we note that some some pathological examples could be wrongly detected by the algorithm. For example, extremely small intersections with the domain corner could be imprecisely calculated. However, these cases are extremely rare and their influence can be neglected. On the other hand, the algorithms are under constant improvements.

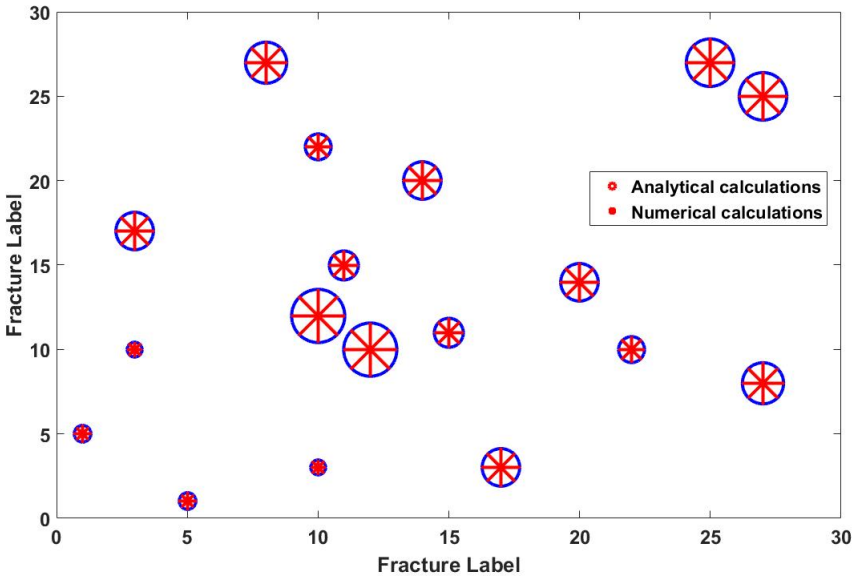

Figure 3.5: Fracture intersections and traces lengths calculations: each intersection is plotted by a symbol (blue circle when an intersection is captured by the Connectivity Algorithm and a red star if an intersection is captured by the Comsol software (our reference)). The sizes of the symbols are proportional to the traces lengths.

3.2.2.2 Numerical performance of the connectivity algorithm

The numerical efficiency of the algorithm isimportant because the proposed method is intended to sharply reduce the computational time for the simulation of flow and/or transport in fractured media. A preliminary analysis of the CPU time can be easily developed from the pseudo-codes (Algorithm.1). The number of operations for the Connectivity Algorithm is proportional to N^2 in the worst case scenario (i.e., very dense network in which every fracture can intersect any other fracture). The computational performance can be investigated regarding two essential parameters (i) the number of fractures and (ii) the intersection density. Fig.(3.6) presents the evolution of the CPU time as function of the intersection density (here is expressed as the mean number of intersections per fracture). Three different regions can be distinguished from Fig.(3.6). At low intersection density, fractures are so disconnected from each other that the three filtering procedures (described earlier) will eliminate many fractures, and hence, the CPU time is relatively small. The second region corresponds to an important increase in CPU time as function of intersection density: the density is high enough that an increasing amount of pairs of fractures has to be checked, and furthermore, the role of filtering decreases with increasing density. Finally, at some point, the intersection density is high enough that the algorithm has to check the possibility of intersection of all the pairs of fractures, and the filtering tests become roughly unnecessary.

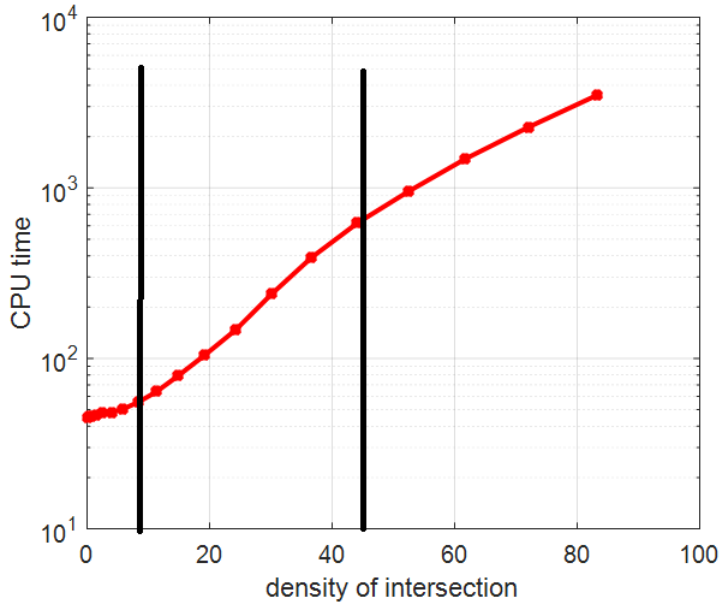

Figure 3.6: CPU time needed for the Connectivity Algorithm as function of the mean number of intersections per fracture.

Other benchmark tests could be considered, e.g., comparing our algorithms with similar algorithms or tools described in the literature. However, only a few algorithms have been published, and their numerical efficiency is not always highlighted. A recently published work [Dong et al. (2018)] presents a new technique for calculating fracture intersections in 3D called bounding box and sweeping line (BBSL) method. They tested their original method and compared it with more classical methods for intersection calculation. An example of 3D fracture network containing 10,000 fractures with specific density of 0.0625 $[m^{-1}]$ was tested and, the CPU time needed for the intersection detection was 2.63 [s]. The same case is generated in the present work and treated for comparison. Our Connectivity Algorithm takes 48 [s] to treat the same case. One should emphasize here that the CPU time in the work of Dong et al. 2018 concerns only the intersection detection. However, the CPU time of 48 [s] needed for the Connectivity Algorithm includes, other than the intersection detection, all the related operations (Areas, Links, etc. as in Fig.(3.4)) as explained in the description of the algorithm.

As conclusion, a benchmark exercise is needed to compare the Connectivity algorithm to other similar algorithms with the aim of improvement. This task is kept as a perspective to the actual work.

3.2.3 Application of the connectivity algorithm

In this section, some immediate applications of the Connectivity Algorithm are presented. It is important to recall, at this stage, that the initial purpose of the Connectivity Algorithm is to construct the inputs of the next numerical steps (Clustering algorithms (Sect.3.3) and Graph algorithms (Sect.3.4)). The presented examples in this section are several applications of the connectivity algorithms concerning mainly the analysis of the geometrical properties of DFN, in relation with the review presented in the first chapter. For the sake of brevity and clarity, two applications are shown as follows.

- Application 1: Traces and trace length distribution

In this study, traces are the lines resulting from the intersection of two planar fractures in 3D. One has to distinguish between traces and nodes, as nodes are the midpoints of traces. It is obvious that the distribution of traces and trace lengths are important in characterizing the behavior of 3D fracture networks concerning flow and transport: the longer the lengths of the traces are, the easier the fluid can flow throw the fracture network. Hence, characterizing the traces and the trace length distribution is crucial in this context. The Connectivity Algorithm is a very suitable tool to accomplish this analysis. To illustrate this point, Fig.(3.7) depicts the histogram of the traces midpoint coordinates (the nodes) and the histogram of the trace lengths (T_{ij}). These results come from a statistically isotropic DFN containing 30,000 disc fractures of equal radius $R_F = 0.7$ [m] in a cubic domain of size $10 \times 10 \times 10$ [m]. As the fractures are distributed uniformally between $X_{min} = -5[m]$ and $X_{max} = 5[m]$, the traces coordinates are also distributed uniformly between X_{min} and X_{max}. Boundary effects can also be seen from the distribution (left of Fig.(3.7)) as the probability to find an intersection at the domain boundary is low.

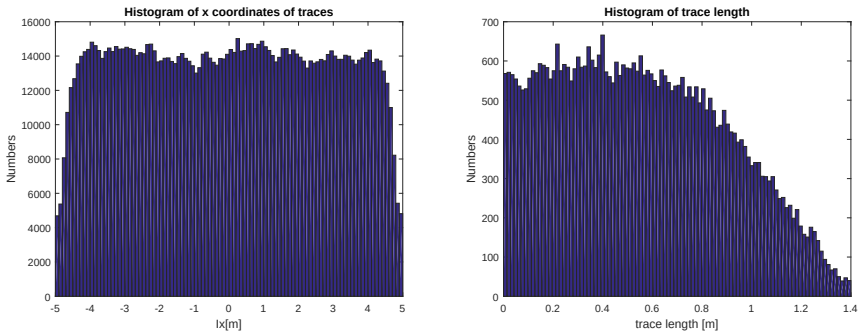

Figure 3.7: Left: histogram of the x-coordinates of the trace's midpoint (nodes). Right: histogram of traces lengths. The results come from a statistically isotropic DFN containing 30,000 disc fractures of equal radius $R_F = 0.7$ [m] in a cubic domain of size $10 \times 10 \times 10$ [m]. This network has a density of 95 intersections per fractures (a very high density).

Another interesting application concerns the cumulative trace lengths of a fracture network. The cumulative trace length is the sum of all the traces lengths in a network and (after proper normalization) it represents a measure of the degree of interconnection of the network. As an example, Fig.(3.8) depicts the relationship between the cumulative trace length and the intersection density ρ (the mean number of intersections per fracture), for the same network used in the previous Fig.(3.7). A linear trend is observed between the intersection density ρ and the cumulative trace length. This relationship (ρ vs. cumulative trace length) is interesting regarding the construction of the 3D fracture network from 2D observations. The subject of DFN geometrical analysis is under recent extensive research , especially concerning the generation of 3D fracture networks from outcrops (2D) and well observation (1D) observations [Weiwi et al. (2019)]. Hence, the developed Connectivity Algorithm could be a suitable tool for more theoretical and practical investigations on the subject.

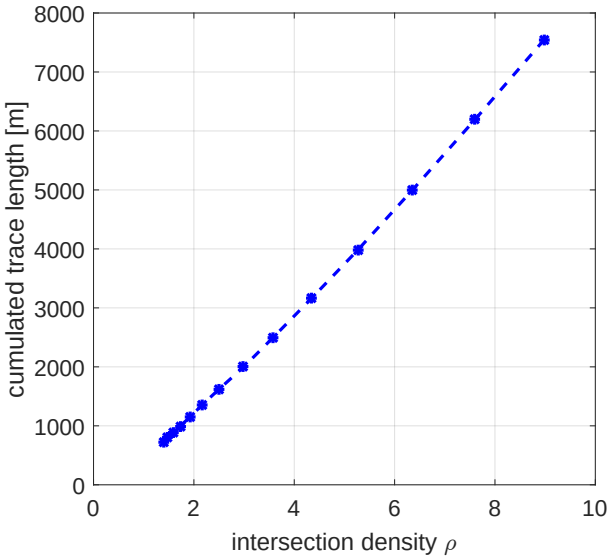

Figure 3.8: Evolution of cumulated trace length as a function of the intersection density ρ (dimensionless). These results were obtained for the case of a statistically isotropic DFN in a cubic domain of size $10 \times 10 \times 10$.

- Application 2: Correlations between intersection density and excluded volume

In chapter 2 (Rajeh et al. 2019), the notion of excluded volume has been introduced and its capability of measuring the connectivity of a fracture network has been detailed. The relation Eq.21 in chapter 2 presents a calculation of the mean number of intersections per fracture. However, two precautions have to be taken into account: (i) the number of intersections of fractures in the domain is high enough to reduce statistical fluctuations, and (ii) boundary effects due to the finite domain of study have to be taken onto account correctly. However, in some situations, these two assumptions may not be verified. The effect of the fracture to domain size ratio is, now, investigated using the Connectivity Algorithm. Let us recall the definition of the intersection density as defined based on the excluded volume:

$$V_{EX,f} = \frac{1}{2} A_f P_f \tag{3.3}$$

where A_f and P_f are respectively the area and perimeter of the fracture. The effect of fracture to the 3D domain size and of the statistical fluctuation on the prediction of the intersection density ρ is depicted if Fig.3.9. As it can be shown in the figure, when the 3D upscaling domain is equal to the generation domain (i.e. there is fractures that are not entirely inside the upscaling domain), the exact intersection density as calculated by the connectivity algorithm is over-estimated by the intersection density as calculated by the excluded volume formula. Also, when the upscaling domain is small in comparison with the generation domain (for ratios smaller than 0.4 in Fig.3.9), there exists a slight difference between the two intersection densities which is due to the statistical fluctuations as the mean is calculated over a realtively samll number of fracture intersections. Between

the two extremes, the intersection density is exactly predicted by the excluded volume formula. In general, to avoid boundary effects while using the excluded volume formula (3.3) for intersection density , the upscaling domain should be at least smaller than the generation domain minus the size (diameter D_{Fmax}) of the largest fracture in the DFN. In terms of domain size and largest fracture diameter D_{Fmax}, this can be expressed as: ($D_{upscaling} = D_{generation} - D_{Fmax}$). This caution is very important in order to ovoid artificial effects due the domain size while studying percolation phenomena (Chapter4).

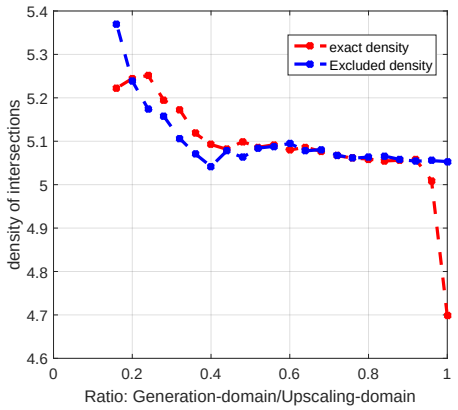

Figure 3.9: The evolution of the intersection densityρ as function of the ratio between the generation and the upscaling domain. The intersection density as calculated exactly by the connectivity algorithm (red) and as predicted by the excluded volume formula (blue).

In some case for numerical studies, there would be some fractures that will intersect the 3D domain boundaries. In that case (a fracture intersecting the boundary), the previous formula of the excluded volume could be modified to take into account the fact that only a part of the area of the fracture is inside the domain. As the exact area of a fracture inside the domain can be calculated by the Connectivity algorithm, the exact area of the part of the fracture inside the domain can be used instead of the total area. So the excluded volume formula can be modified as

$$V_{EX,f} = \frac{1}{2} A_{Exact,f} P_{EQ,f} \tag{3.4}$$

where $A_{Exact,f}$ is the exact area calculated by the Connectivity algorithm, and $P_{EQ,f}$ is calculated using an equivalent radius $R_{EQ,f}$ of the fracture area inside the domain:

$$\begin{cases} R_{EQ,f} = \sqrt{\frac{A_{Exact,f}}{\pi}} \\ P_{EQ,f} = \pi R_{EQ,f} \end{cases} \tag{3.5}$$

The modified formula (Eq.3.4) of the excluded volume predicts more accurately the intersection density (the mean number of intersections per fracture).

3.3 Search of clusters in 3D fracture networks

The second part of this set of algorithms consists on a suite of algorithms for clustering and percolation analysis called “Clustering Algorithms”. A cluster is a group of fractures

in which each fracture is connected to all the other fractures directly or indirectly. A percolating cluster is a cluster that connects at least two opposed boundaries of the 3D domain. We recall that in this thesis the term percolation is somehow different from the more theoretical definition in percolation theory (this point has already been discussed in chapter 2).

The adjacency matrix FF determined by the Connectivity Algorithm is now the input of the Clustering Algorithm. A new efficient method is now presented for the search of clusters and the determination of the percolating sub-network (percolating cluster). A method for the search of dead-end clusters is also introduced.

3.3.1 Description of clustering algorithms

This algorithm computes the clusters in a given DFN composed of circular or elliptical fractures (or both). It is based in the multiple labeling technique described in Hoshen and Kopelman (1976). In the Hoshen-Kopelman algorithm, the connectivity of a 2D regular mesh-grid of binary elements (e.g., pixels) was computed while minimizing the number of operations. We propose an original adaptation of the Hoshen-Kopelman approach algorithm as a way to determine the percolating clusters in a 3D fracture networks of planar fractures.

The Clustering Algorithm consists of three main steps:

- Step 1: Clusters search

We have generalized the Hoshen-Kopelman Multiple Labeling Clustering (MLC) technique to 3D planar objects (fractures) which do not lie onto a regular grid, but are irregularly located in space. In addition, the neighboring criterion corresponds in our case to the geometrical intersection of fractures in 3D (the adjacency matrix). Each new cluster appearing in the search is called "proper cluster", and it is labeled using the lowest number of all the fractures forming that cluster. Cluster classification information is summarized in one vector of length equal to the number N_f of fractures in the DFN. The vector called "P" is constructed as follows. If $P(i) = a$, where "a" is a positive value, then the fracture "i" is a proper cluster that contains "a" fractures. If $P(i) = -a$, where "$-a$" is a negative value, then the fracture "i belongs to the proper cluster number "a". The following pseudo-code gives a simple explanation of the cluster search by MLC technique. Algorithm.(2) illustrates the implementation of clustering calculations. This algorithm was developed using vectorization in Matlab.

Algorithm 2 MLC algorithm

Load the adjacency matrix FF from algorithm 1
Fracture "1" is chosen ⇒ it defines proper cluster "1"
For i=2 to N
  If fracture "i" do not intersect "i-1" , then:
    fracture "i" is a new proper cluster labeled "i"
  else
    fracture "i" belongs to proper cluster "i-1"
  End if
End for
Fill into output matrices

- Step 2: Percolation detection

To define percolation, two opposite faces of the 3D domain have to be at first designated ([-X +X], [-Y +Y], [-Z +Z]). In this step any proper cluster intersecting any face of the domain is checked. The result is saved in a matrix of size $[N_F \times 6]$, in which a positive value "1" in row i and column j indicates that cluster "i" intersects the corresponding boundary face j, according to [-X +X -Y +Y -Z +Z] column format.

- Step 3: elimination of dead-end fractures and dead-end clusters

A dead-end fracture of the percolating cluster is identified if it only intersects one other fracture. The search of dead-end clusters starts by finding fractures of the percolating cluster with only two intersections: this is obtained by inspection of the adjacency matrix. Then, successive intersecting fractures are pursued until intersection with boundaries is reached. If no boundary is reached, this set of fractures will define a dead-end cluster, which is then eliminated from the percolating cluster. The following pseudo code (Algorithm.3) illustrates the algorithm of dead-end clusters elimination. This algorithm was developed using vectorization in Matlab.

Algorithm 3 Dead-end Clusters Elimination algorithm

Eliminate fractures intersecting only one other fracture (dead-end fractures)
Identify fractures intersecting only two other fractures N_{F2}
For i=1 to N_{F2}
  For j=1 to 2
    Identify set of fractures S_j intersecting fracture j
    While S_j is not empty
      If any fracture in F touches frontiers Then
        Not a dead-end cluster
      End if
    Update S_j with set of fractures intersecting fractures in F
    End while
  Eliminate dead-end cluster found if any
End for

To summarize the main outputs of the proposed Clustering Algorithm, Fig.(3.10) shows an example of the input DFN (a), the resulting percolating cluster (b) and the final cluster without dead-ends (c).

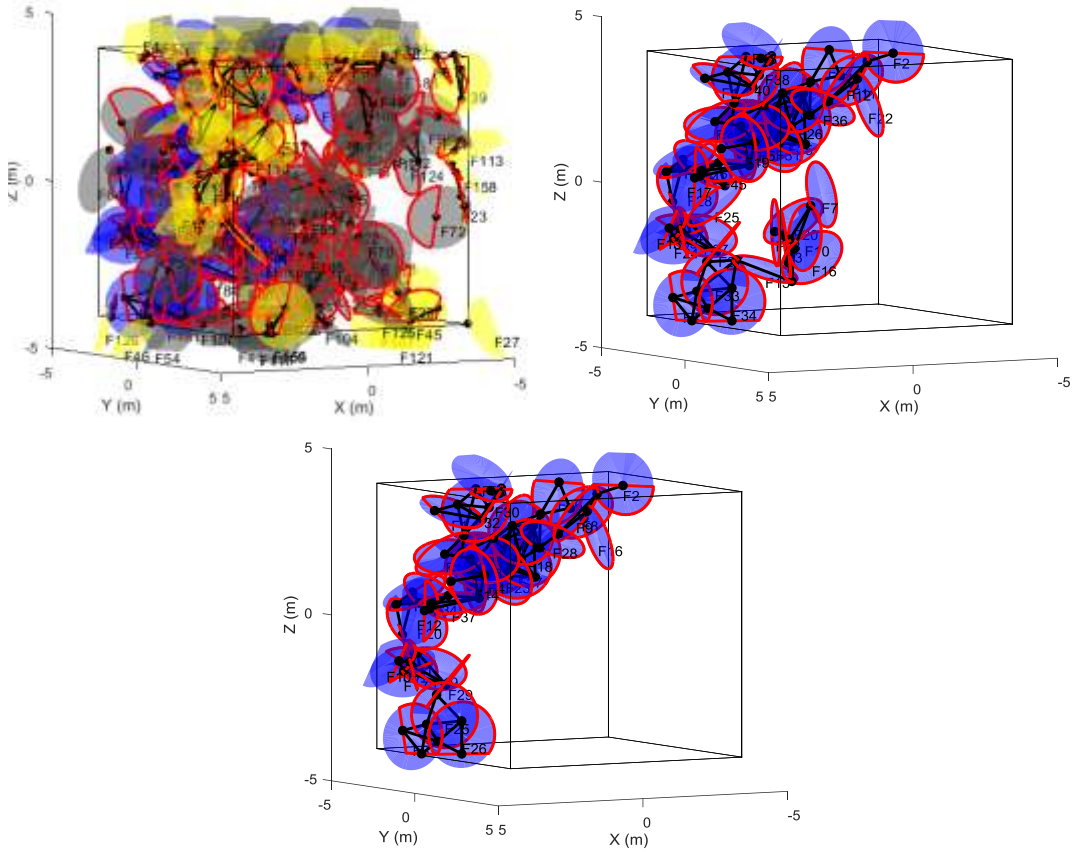

Figure 3.10: Example of fractured medium with Nf=200 fractures in a domain of $8 \times 8 \times 8$ m3: (a) the initial DFN; non-percolating clusters and isolated fracture are in yellow. (b) blue: fractures forming the percolating cluster corresponding to [-Z,+Z]; the black points (•) represent the nodes and black segments (—) represent the links.(c): The percolating cluster after the elimination of the dead-end clusters.

3.3.2 Validation and numerical performance of the clustering algorithm

3.3.2.1 Validation of the clustering algorithm

The aim of this section is to a perform series of validation tests to verify the correctness and the accuracy of the Clustering algorithm in predicting the clusters formation and the percolation. The validation is carried out by comparing the percolation density as predicted by the Clustering Algorithm (more precisely Algorithm3.2) and the percolation density calculated numerically by detailed flow simulation performed on the software Comsol Multiphysics (as in chapter 2). One of the procedures of validation is as follows: at each realization of the 3D fracture network, the critical density of percolation is calculated in the 3 directions by the Clustering Algorithm. Once the number of fractures necessary to reach percolation is obtained, the numerical flow simulation is performed twice: the first time, with the predicted percolating network diminished by one fracture (just before percolation) and the second time with the predicted percolating network. If the Clustering algorithm calculates exactly the critical density of percolation, we expect that the flow rate in each realization will present a jump from zero in the first simulation (one fracture before percolation) to a positive non-zero flow rate in the second simulation (at percolation). As illustrated from Fig.(3.11), the jump of the flow rate is observed, indeed, for each realization of the 3D DFN and for all the three directions (X, Y and Z) as expected. This important accuracy of the results demonstrates the ability of the Clustering algorithm proposed in this section to calculate "exactly" the critical density of percolation for various 3D fracture networks (many other tests have been performed over various fracture sizes and shapes and similar positive results have been obtained).

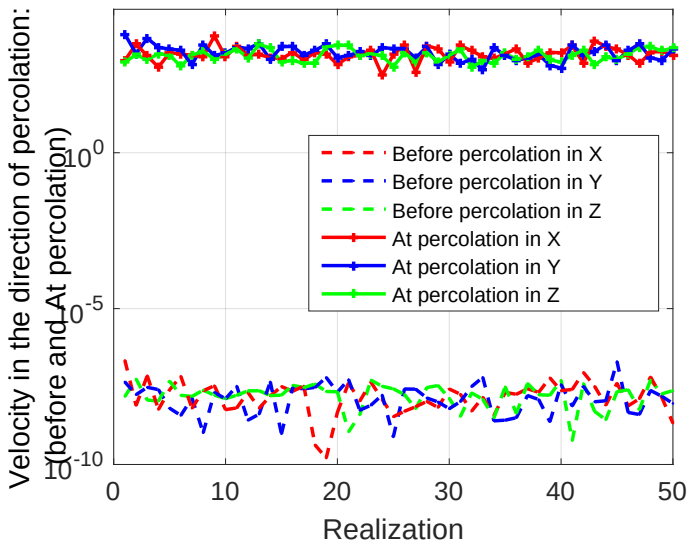

Figure 3.11: Flow rate calculated in the opposed permeable faces: the discontinuous lines represent the flow rate just one fracture before percolation as predicted by the algorithm, and the continuous lines represent the flow rate at percolation. The 3 colors refer to the three directions (X, Y, and Z)

3.3.2.2 Numerical performance of the clustering algorithm

The numerical performances of the Clustering Algorithm are investigated now.

A preliminary analysis of the CPU time can be easily seen from the two pseudo-codes (Algorithm.2 and Algorithm.3). The number of operations for cluster search algorithm is proportional to N_F. It is seen that the computation time depends on both the number of fractures N_F in the DFN and more importantly on the number of intersections (Nodes) in the system. To check out this point, Fig.(3.12) shows the CPU time of the clustering algorithm (Algorithm.2) as function of the number of fractures in the DFN (X axis) and the mean number of intersection per fracture (Y axis). In most of the cases, below the percolation density (around 2 intersections per fracture) and for less than 5,000 fractures, all the computation times stay below one second. Even for very dense and large fracture networks (100,000 fractures with 10 intersections per fracture, which presents a very dense and large networks typical for engineering applications), CPU time does not surpass 100 seconds (in a personal compuet of 32 G of RAM, 2.2 GHz) for the clusters search and for percolation detection.

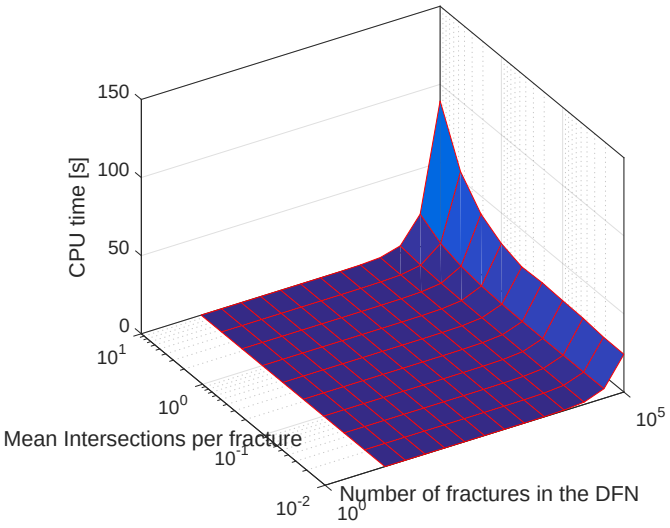

Figure 3.12: CPU time for the cluster search as a function of the number of fractures (X axis) and the mean number of intersections per fracture(Y axis).

Parallel to the MLC method originally developed in this work, we have implemented another algorithm for clusters search called "Deep First Search (DFS)". The DFS algorithm is not detailed here as it can be found in the literature [Macé (2006)]. A benchmark is performed using the two methods (MLC Versus DFS). This task can be seen as (i)a validation test and (ii)a computational efficiency comparison. This comparison highlights the numerical efficiency of the MLC method because in all tested cases the CPU time of the MLC was smaller than the CPU time of the DFS algorithm. A typical benchmark test is presented in Fig.3.13. The SpeedUp (CPU_{DFS}/CPU_{MLC}) was calculated for various DFN (N_f=1000; 10,000; 100,000 fractures) with increasing intersection density.

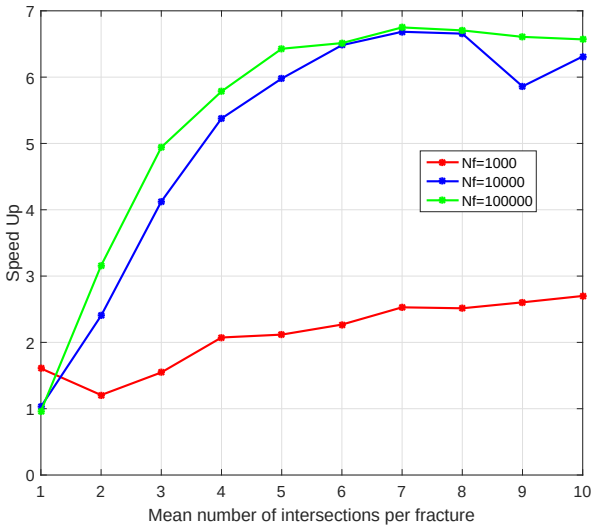

Figure 3.13: SpeedUp (CPU_{DFS}/CPU_{MLC})) as a function of intersection density for various sizes of the DFN. The number of fractures N_F is one thousand, ten thousands, and one hundred thousands, respectively.

3.3.3 Applications of the clustering algorithm

In this subsection we explore possible applications of the Clustering Algorithms in DFN's. Let us at first remind that the initial motivation of the development of theses tools was the two issues highlighted in the conclusion of chapter.2 (i.e,. connectivity of the DFN and percolation detection). It is obvious now that the Clustering algorithm developed in this section is very suitable to address the second issue (Percolation). The Percolation in DFN will be addressed in more details in the next chapter. Here, some other interesting uses of the Clustering algorithm have arisen while developing the tool are presented.

Flow simulations in DFN are a crucial task for modeling the hydraulic behavior of a fractured rock. Flow in the fractured medium will pass only through the percolating clusters from source to target in a typical simulation. With the Clustering algorithms, the percolating clusters can be easily and quickly determined. Hence, the Clustering algorithm is used as a pre-processing before flow simulation. Without this pre-processing, each flow simulation has to be performed upon the total DFN containing N_F fractures which leads rapidly to great difficulties in meshing and/or flow simulation. However, when using the pre-processing, the number of fractures and the number of intersections are drastically reduced. Note that the meshing difficulties are mostly related to treating fracture intersections. We explore the usefulness of the Clustering algorithm in the following manner. Given an initial DFN, we perform a numerical simulation of flow between two opposite boundary faces of the 3D domain,(e.g., [-X,+X]). The Clustering algorithms are used to check only the percolating clusters and eliminating all the rest of the DFN (isolated fractures, isolated clusters, dead-end fractures , dead end clusters). Then, the same flow simulation between the two domain boundaries is performed on the "cleaned" DFN (only percolating clusters). One can expect to see that the flow rate resulting from the two simulations will be the same (as the non percolating clusters do not participate in flow). The important point to highlight here is that the pre-processing of the DFN by the Clustering Algorithms permits

a considerable reduction in meshing and flow computational efforts while keeping the same flow rates results. Fig.(3.14) presents an example of this CPU reduction expressed as the gain in the number of fractures and in CPU time. In this example a DFN is generated in a domain of size $10 \times 10 \times 10$[m] and the fracture radius is changed from 2[m] to 0.6[m]. Flow simulations are performed over each of these DFNs and the gains (in Fracture number reduction and in CPU time speedup) are reported. One can note that for high density of the DFN, the speed up in CPU time for flow simulations surpasses 100.

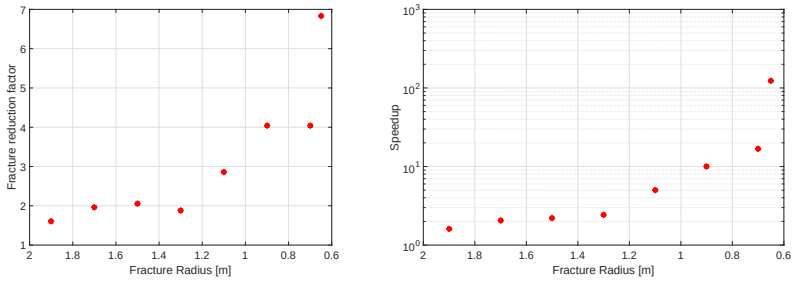

Figure 3.14: Left : fracture reduction factor vs. fracture radius, showing the reduction in the number of DFN fractures gained by the Clustering Algorithms. speed up vs. fracture radius ; this shows the CPU time gained in the numerical flow calculations (meshing and flow simulations). $SpeedUp = CPU_{All,DFN}/CPU_{Percolatingclusters}$.

3.4 Graph of the DFN

3.4.1 Introduction to graphs and graph theory

As a concept, a graph is formed by vertices and edges connecting the vertices. A rigorous formal definition of a graph can be stated as a pair of sets (V,E), where V is the set of vertices and E is the set of edges, formed by pairs of vertices. Fig.(3.15) depicts an example of the graph structure taken from Entryphone (2013). The graph theory is used as a new approach [Valentini et al. (2007)] to treat fracture networks, which allows us to move beyond complicated direct description of geometric parameters of the DEN (e.g. orientation, size, position etc.).

The vertex set of a graph V(G) is

$$V(G) = \{v_1, v_2, v_3, ..., v_m\}$$

where m represents the vertices number. Usually, v_i is represented by its spatial coordinates (X, Y, Z). The edges set of a graph E(G) is

$$E(G) = \{e_1, e_2, e_3, ..., e_n\}$$

A graph is associated to an adjacency matrix $M[mxm]$ defined as follows

$$M(i,j) = \begin{cases} 1 & if\ v_i\ is\ connected\ to\ v_j \\ 0 & otherwise \end{cases}$$

Introductory textbooks to graph theory can be found in the literature [Wallis (2007)]. Graph theory finds its applications in different domains like urban engineering, social

networks, natural networks, economy etc. Our aim in this section is to give a graph representation of the 3D fracture networks. The final motivation of this approach is to benefit from the theorems and algorithms well established by graph theory and to apply them for insightful analysis of DEN with focus on flow and transport through fractured rocks.

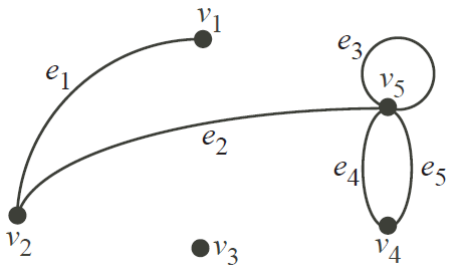

Figure 3.15: The structure of a graph. Vi represent the vertices (dots) and Ei represent the edges (lines).

3.4.2 Graphs of fracture networks

To construct the corresponding graph of a 3D fracture network, the two matrices trace-trace (TT) and Link-trace (LT), introduced in the description of the Connectivity Algorithm (Sect.3.2) are used. Given NN and LN matrices, one can easily deduce a graph representation of the DFN. The nodes (the mid-points of the traces) correspond to the vertices in a graph representation. The link (a link is the fracture that relates two nodes) is the edges in a graph representation of DFN. The adjacency matrix FF of the first illustrative example given in Sect.1 (Fig.(3.4)) is given by

$$FF = \begin{pmatrix} 0 & 1 & 1 & 1 & 0 & 0 & 0 & 0 & 0 \\ 1 & 0 & 1 & 0 & 0 & 0 & 0 & 0 & 0 \\ 1 & 1 & 0 & 0 & 0 & 0 & 0 & 0 & 0 \\ 1 & 0 & 0 & 0 & 0 & 0 & 0 & 0 & 0 \\ 0 & 0 & 0 & 0 & 0 & 1 & 1 & 1 & 0 \\ 0 & 0 & 0 & 0 & 1 & 0 & 1 & 0 & 0 \\ 0 & 0 & 0 & 0 & 1 & 1 & 0 & 0 & 0 \\ 0 & 0 & 0 & 0 & 1 & 0 & 0 & 0 & 0 \\ 0 & 0 & 0 & 0 & 0 & 0 & 0 & 0 & 0 \end{pmatrix}$$

Note that a graph based on the TT matrix is similarly defined. The difference between graphs based on the FF matrix and the TT matrix is used in the next chapter while resolving the flow problem on the graph. An example of the calculation of FF the graph representation is given in Fig.(3.16).

Given the previous graph representation, one has all the tools, theorems, algorithms of the graph theory that can be used for insightful analysis of the fracture network and its geometrical,topological and physical properties. An interesting example of application of graph theory to DFN is given in the next subsection.

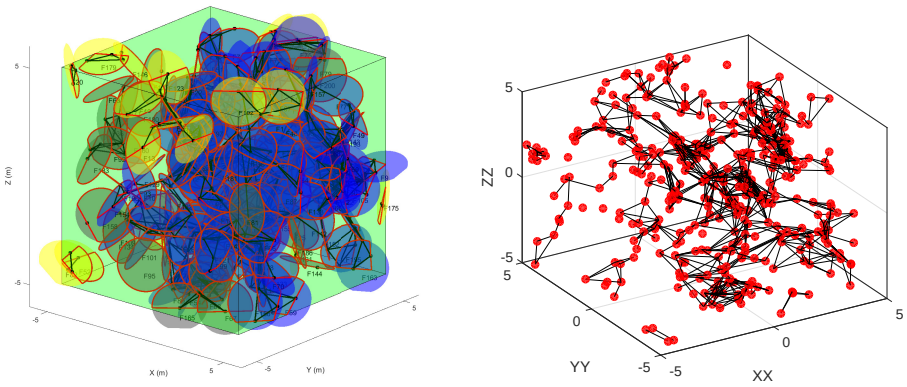

Figure 3.16: Graph representation of DFN of 200 fractures. Left: the DFN; the isolated fractures and the non-percolating clusters in yellow and the percolating cluster in blue. Right: the corresponding graph; the red dots present the intersections (nodes) and the black straight lines represent the links.

3.4.3 Shortest path in a DFN based on graph theory

The shortest path algorithm determines the shortest way to connect two vertices (source "S" and a target "T"). The shortest path is determined by the Dijkstra algorithm. The Dijkstra algorithm is implemented but not described here. More details on the Dijkstra algorithm can be find in Wallis (2000). Fig.(3.17) depicts the shortest path between the sources (here we have chosen to present the flow between the two opposite faces X- and X+). The method consists on searching all the nodes that intersect the face X- and consider them as sources and searching all the nodes intersecting the face X+ and consider them as targets. The procedure is applied on the previous network (200 fractures) and the result is the following (Fig.(3.17)).

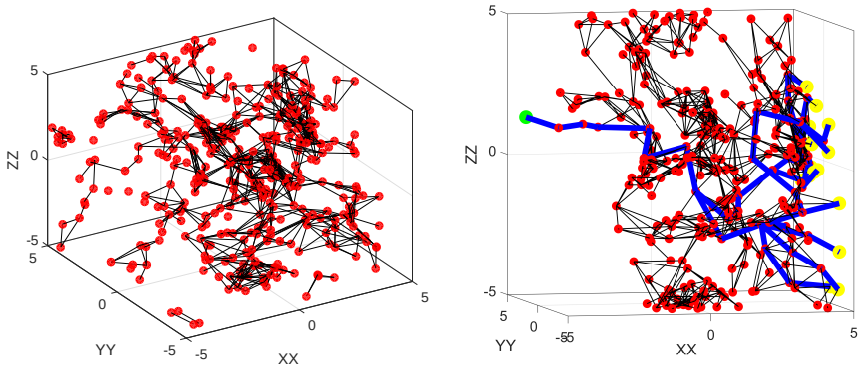

Figure 3.17: Graph representation of DFN of 200 fractures. Left: representation of the complete graph as in Fig.(3.16). Right: the shortest path for flow between faces X- and X+. Here, a single source is found: only one node intersects X- (in green) and 17 targets (17 nodes are intersecting the face X+ yellow).

3.5 Conclusion

In this chapter, a numerical framework for geometrical and topological analysis of three-dimensional fracture networks is presented. The numerical framework is composed of three main sets of algorithms:

- Connectivity Algorithms capable of calculating all the geometrical attributes of the DFN (e.g., areas, intersections etc.)
- Clustering Algorithms capable of determining all the clusters in the DFN, detecting the percolating clusters and eliminating dead end clusters.
- Graph Algorithms capable of constructing the corresponding graph of the DFN and allowing the application of several interesting algorithms from graph theory, like the determination of the shortest path between sources and targets in the DFN. Other algorithm like the maximum flow algorithm are also of important interest for graph representation of DFN.

The algorithms have been validated in detail and their originality and their computational efficiencies have been highlighted. Furthermore, possible interesting uses of each set of the developed algorithms are given and some examples of applications are presented.

As a conclusion, this set of algorithms is a response to an initial motivation mentioned in the conclusion of chapter two concerning two issues (percolation and connectivity in DFNs). However, while developing these tools a lot of other interesting applications have arisen concerning wide range of aspects of DFN like trace analysis, graph theory etc. These tools changed drastically our view of DFN as our capabilities of analyzing such networks are now much more stronger than at the beginning of this thesis. Some of the new way of treating DFN regarding connectivity, percolation and upscaling are addressed in the following chapter. Other ideas regarding DFN analysis are kept as perspectives to the present thesis.

Chapter 4

New Approaches on Percolation, Clustering and Upscaling Based on DFN's Topology

4.1 Introduction

This chapter presents new approaches on the analysis of 3D fracture networks concerning three main issues: (i) the percolation, (ii) the geomorphological description of the clustering process and (iii) the equivalent permeability estimation of the DFN based on the graph approach. As mentioned in the conclusion of the previous chapter, the developed tools concerning the connectivity, clustering and graph of the DFN provide new capabilities for treating the percolation, clusters identification, connectivity and flow in a computationally efficient way.

This chapter could be viewed as a response to the limitations of the superposition method mentioned in the conclusion of chapter 2. We remind here the two limitations mentioned in that conclusion. The first limitation concerns the determination of the critical percolation density $\rho_{EX,C}$, because it is a computationally expensive task and the methodology used can lead to non-accurate values due to the relatively large standard deviations observed around the mean value of $\rho_{EX,C}$. The second limitation concerns the difficulty to assess the degree of connectivity of the network which leads automatically to an inaccuracy on the determination of the equivalent permeability of the 3D fractured medium. Using the toolbox described in chapter three (Connectivity, Clustering and Graph algorithms), these and other issues will now be addressed addressed more efficiently leading more insightful analysis and conclusions. This constitutes the purpose of this chapter.

The dimensionless density based on the concept of excluded volume is a key parameter in analyzing fracture networks as it gives to the analysis a universal character. The equivalence between the dimensionless density based on the excluded volume ρ_{EX} and the exact intersection density ρ (as calculated by the Connectivity algorithm) has been examined in the previous chapter where the effects of finite domain and of statistical fluctuations have been highlighted.

In Sect. (4.2), the percolation phenomenon in DFN is studied and the critical percolation density is determined for mono-disperse isotropic networks. Then, in Sect. (4.3), the geomorphological description of the process of clustering (i.e., the formation of clusters of fractures) in a DFN is analyzed and a modified Rayleigh law is proposed as a unifying law for the clustering in DFNs. In Sect. (4.4), new approaches for flow and equivalent

permeability estimation of fractured rocks are proposed based essentially on the graph representation of DFN and the topological properties determined by the topological analysis of Chapter 3.

4.2 Percolation in DFN

4.2.1 Methodology

The methodology of determining the critical percolation density is similar to the one used in chapter 2. It consists on generating numerous realizations of 3D fracture networks. The parameters of the network (orientation distribution, size distribution etc.) are unique for each critical density determination and hence are the same for all the realizations. For example, if the sensitivity of the critical percolation density on the fracture size is investigated, a determination of critical density has to be performed for each fracture size.

The different realizations are obtained by adding fractures from a pre-set of random fractures: N=1000 disc fractures are first generated, the number of fractures being therefore increased by sampling into this pre-set of 1000 random fractures. This numerical procedure is equivalent to generating several independent realizations of fractures sets. For instance, in a sequence of 1000 generated fractures, the first subset of 100 fractures is independent from the 2nd subset (fractures N=101 to N=200).

The numerical procedure to determine the critical percolation density consists in conducting a series of Connectivity analysis for a single replicate of the fracture network with increasing fracture density.

For each density, the Clustering algorithm is used to determine if a percolating cluster do exist. As fracture density of the DFN increases, a percolating cluster relating two opposite faces of the 3D domain will be formed. This density corresponds to the critical percolation density. This procedure is repeated for several realizations and the mean value of the critical percolation density is retained.

This procedure of determination of the critical percolation density is different from the one used by [Mourzenko et al. (2005)]. In their work, the percoaltion is calculated in fracture networks with fixed number of fractures (fixed density of the network) for multiple realizations. However, in the present work ,the percolation is viewed as a dynamic process where the density of the network gradually increases (either by adding new fractures to the network or by increasing the radius of the existing fractures in the network).

4.2.2 Results of critical percolation density

In this subsection, the determination of the critical percolation density using in a sequential manner the Connectivity and the Clustering algorithms is addressed.

Our aim is to replicate, in the objective of comparison, the studies of [Mourzenko et al. (2005)] in terms of critical percolation density for a Poissonian isotropic mono disperse (constant radius) fractured network. An analyzing domain of $8\times8\times8m^3$ has been used, and radius of the fractures has been varied from R=1 m to R=0.3 m (i.e., for each radius, the procedure of the determination of the critical percolation density is applied over multiple realizations). The number of realizations that have been performed is different for each radius. The number of realizations increases as the radius increases. For the smallest radius $R_F = 0.3m$, the number of realizations is 50. For the maximum radius $R_F = 1$, the number of realizations is 1000. Figure 4.1 shows the average and the standard deviation

of the critical percolation density ρ_C, as function of the fracture to domain size ratio, calculated with Connectivity and Clustering algorithms (exact calculations).

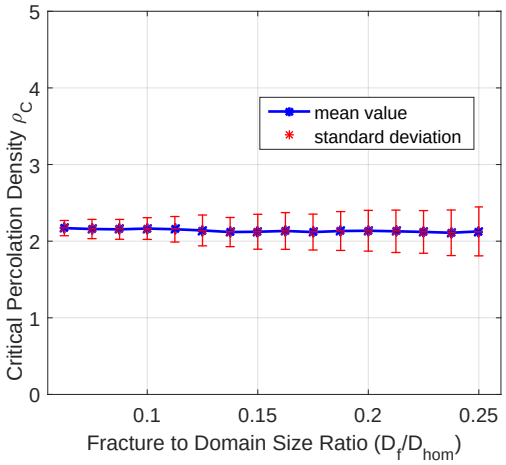

Figure 4.1: Evolution of the critical density ρ_C (dimensionless) as function of the fracture to domain size ratio (D/D_{Hom}).

It can be concluded from the results the following.

- The variation of the critical percolation density with respect to the fracture to domain size ratio is very small. The difference between the two extreme points is $\Delta\rho \approx 0.05$.
- The standard deviation around the mean value of the critical percolation density is explained by (i) the statistical fluctuation, especially if the number of fractures at percolation is small and (ii) the finite size effects of the domain of study (D_{hom}).
- If we take the value of ρ_C for the smallest fracture to domain size ratio (Fig. 4.1, we obtain $\rho_C \approx 2.35$ which is close to the value of $\rho_{EX,C} \approx 2.41$ found in [Mourzenko et al. (2005)]. The slight difference between the results can be attributed to the fact that the circular fracture shape in [Mourzenko et al. (2005)] is approximated by polygons with numerous sides. In the present work, the circular shape of the fracture is analytically taken into account in the calculation of intersections.

On another side, an interesting quantity, at the percolation, is the ratio of the area of the percolating cluster to the total area of DFN. In the previous critical percolation study, we have reported the area of the percolating cluster at the percolation (by the Connectivity and Clustering algorithms). The results are shown in Fig. (4.2).

It can be seen that the percentage of the area of the percolating cluster at percolation decreases when the fracture to domain size ratio decreases. In all cases, the area of the percolating cluster is always less than half the area of the DFN. This quantity (the area of the percolating cluster) is of considerable importance from a hydraulic point of view. After percolation, only the percolating cluster is of interest for the fluid flow through the fractured medium. Hence, the area of the percolation cluster presents an indication of the amount of volume through which the fluid will circulate and hence gives an idea about the permeability of the DFN. Furthermore, a linear decreasing of the ratio of the percentage of

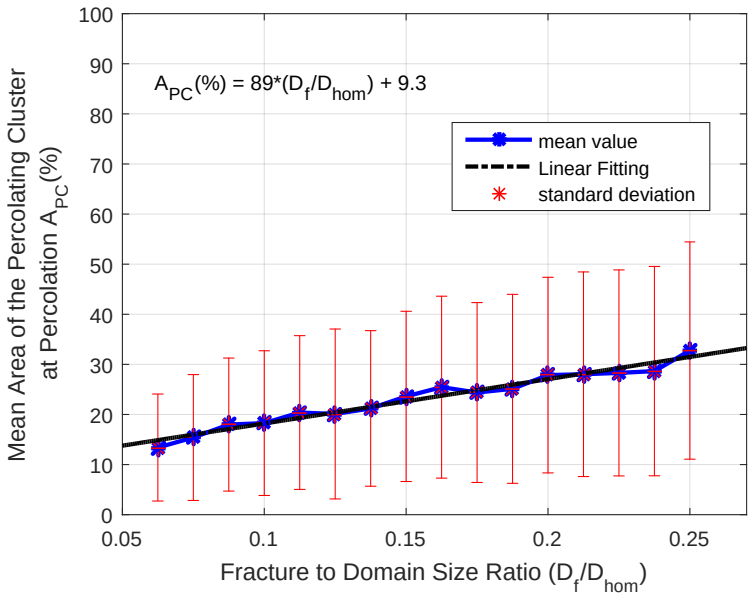

Figure 4.2: Area of the percolating cluster (A_{PC} = % of the total area of the DFN) as function of the fracture to domain size ratio.

the area of the percolating cluster is seen from Fig. (4.2). One can expect from the linear fitting that for an infinite domain, the area of the percolation cluster, at percolation, will be only about 9.3%. However, the fluctuation of the values of the percentage of the area percolating cluster is high and the linear fitting have to be taken with caution.

4.3 The clustering process in DFN

Given the Connectivity and the Clustering algorithm, the clustering process of 3D fracture networks is now analyzed in details. It is meant by the clustering process the formation of clusters from fractures. It consists on the agglomeration of fractures to form clusters and then the agglomeration of clusters to form bigger clusters and so on. It is worthy to notice at this stage that the clustering as addressed in this thesis is a geomorphological observation and it does not take into account the mechanical aspects behind the formation and the propagation of fractures and clusters.

Clustering can give insightful understanding of the connectivity of the fracture network. If there exists a lot of independent clusters in the network, the network is weakly interconnected. However, as the number of clusters decreases, the network become more interconnected until a point where all clusters collapse into one big cluster spanning the entire domain. This subject is important for the hydraulic behavior of the DFN (the main subject of the present thesis). More generally, the clustering process is a research area especially for geo-mechanics trying to understand the evolution of natural and/or engineered fractures and their clustering process. This section analyses two quantities of interest in a DFN: (i) the evolution of the density of clusters in a DFN and (ii) the evolution of the

size of the largest cluster in a DFN.

4.3.1 Evolution of the density of clusters in DFN's

Let us start by defining the Cluster density

$$\rho_{CL} = \frac{N_{CL}}{N_F} \tag{4.1}$$

where $N_{CL}$is the total number of clusters in the DFN and N_F is the total number of fractures in the DFN. Note that if more than two fractures are connected together are counted as a cluster and isolated fractures are not taken into account.

In order to study the evolution of ρ_{CL}, the following procedure has been implemented based on the tools developed in chapter 3.

At first, 3D random fracture networks are generated with varying number of fractures N_F. Let us say, for example, N_F=5,000; 10,000, 15,000 and 20,000. For each fixed number of fractures in the DFN (fixed N_F), multiple realizations of the same DFN are generated to realize statistically meaningful study. Then, for each realization of a DFN, the density ρ (reminder: ρ is the mean number of intersections per fracture) is increased gradually by increasing the radius of the fractures in the DFN. At each density ρ, the Connectivity and Clustering algorithms are used to determine all the existing clusters in the DFN and their proper sizes. A typical study involving a DFN with a fixed number of fractures N_F needs to run the Connectivity and Clustering algorithms about $N_{run} = 200$. Hence, one can imagine the amount of computational efforts needed to realize this study by multiplying the number of runs by the CPU time of each run (The CPU time corresponds to the Connectivity and the Clustering algorithms on DFN's containing N_F fractures).

The following Fig. (4.3) presents the evolution of the density of clusters $\rho_{CL} = \frac{N_{CL}}{N_F}$ in the DFN as a function of the mean number of intersection per fracture ρ. Note that, for fixed number of fractures N_F, each curve (i.e., each color) is the mean value of 20 independent realizations and the standard deviations are marked in the figure. The size of the DFNs used to obtain Fig. (4.3) are resp. N_F =5,000; 10,000; 15,000 and 20,000.

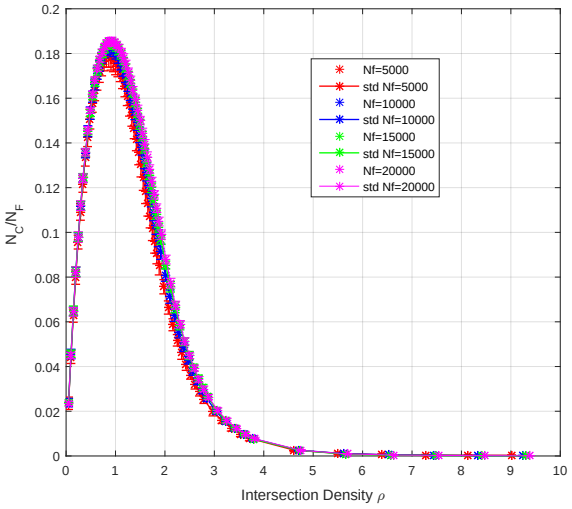

Figure 4.3: Evolution of the density of clusters $\rho_{CL} = N_{CL}/N_F$ with respect to the density ρ. The different colors correspond to different number of fractures in the DFN. The bars correspond to the standard deviation at each density.

The evolution of the density of clusters depicted in Fig. (4.3) is roughly independent from the number of fractures in the DFN. This result shows that when using ρ as a measure of the density of the DFN, a "quasi-universal" behavior of the clustering process can be easily deduced. Independently from the number of fractures in the DFN, the clustering process is the same, when the density ρ increases, the fractures collapse together forming small groups of fractures called clusters. The number of clusters rapidly increases until a critical density σ (not to confound with the critical density of percolation ρ_C) is attained, at which the clusters begin to agglomerate together and form larger clusters. For densities smaller than the critical density σ, the formation of new clusters from isolated fractures is the dominant mechanism of clustering. However, for densities larger than σ, the agglomeration of existing clusters to form larger clusters is the dominant mechanism and the formation of new clusters from isolated fractures begin to be a marginal process . Hence, the number of clusters rapidly decreases until all the fractures belong to a single large (or infinite) cluster.

Another important consequence from Fig.(4.3) concerns the shape of the curve of $\rho_{CL} = f(\rho)$. It can easily be seen that a Rayleigh law can describe this evolution.

The standard Rayleigh law is written as

$$\rho_{CL} = \frac{\rho}{\sigma} \exp(\frac{-\rho^2}{2\sigma^2}) \tag{4.2}$$

where σ is the parameter of the Rayleigh law and it should be a positive number. σ can be easily determined from data (similar to Fig. (4.3)) by determining the coordinates of the maximum value of $\rho_{CL} = f(\rho)$. The robustness of the Rayleigh law to describe the data came from the fact that a single parameter σ is needed to calibrate the Rayleigh Law.

The task of determining the coordinate of the critical point $(\sigma\ ,\ f(\sigma))$ is performed over a large number of DFNs with varying $2,000 \leq N_F \leq 30,000$. To do so, the same procedure as in Fig. (4.3) has been performed for each DFN for several realizations. The step $\Delta\rho$ by which the density is increased is set to $\Delta\rho = 0.01$ enabling a precise determination of

the coordinates of the critical points $(\sigma\ ,\ f(\sigma))$. Each determination of the critical point is performed over 20 independent realizations. Then, the mean value is obtained and the standard deviation is evaluated. The results of the determination of the critical point are depicted in Fig. (4.4).

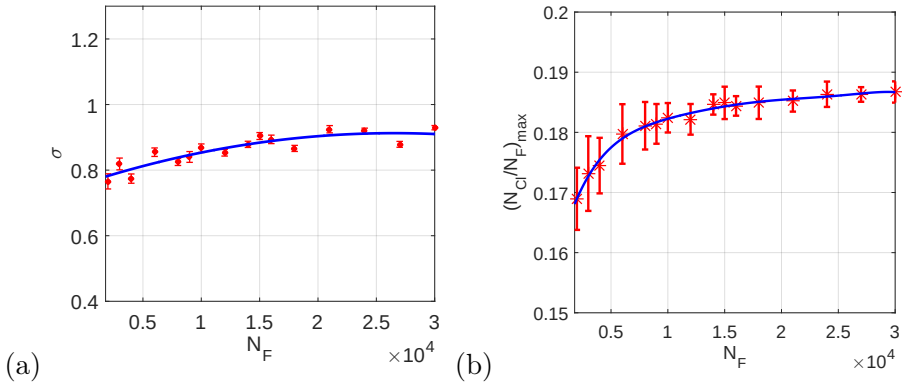

Figure 4.4: Evolution of the coordinates of the critical point as function of the number of fractures N_F in the DFN. (a) the critical density σ and (b) the maximum cluster density $\rho_{CL,max}$.

It can be seen that the variation of the coordinates of the critical point is small. One can report the narrow range of variation of the coordinate of the critical point from the previous analysis as

$$\begin{cases} 0.7657 \leq \sigma \leq 0.9294 \\ 0.1689 \leq \rho_{CL}(\sigma) \leq 0.1867 \end{cases} . \tag{4.3}$$

More interestingly, Fig. (4.4) shows clearly that the coordinates of the critical point converge toward a fixed value as the number of fractures in the DFN increases. This enforce the possibility of using Rayleigh law to describe the process of clusters evolution in a DFN.

Finally, one can compare the ability of a Rayleigh law in describing the evolution of clusters in a DFN by scaling the normalized Rayleigh law (Eq. (4.2)) by the coordinates of the maximum point. An example of comparison is depicted in Fig. (4.5).

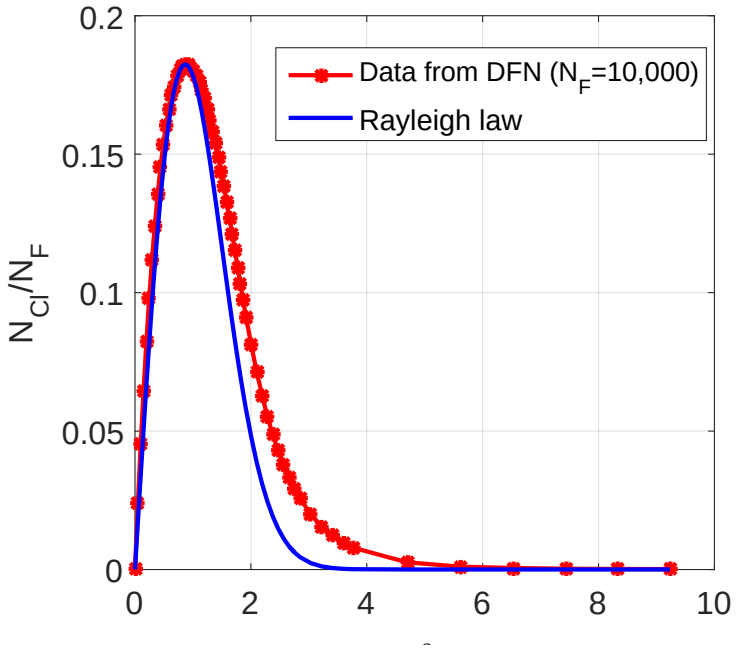

Figure 4.5: Rayleigh law for describing the cluster evolution in a DFN. The DFN contains 10,000 fractures.

As it can be seen, the Rayleigh law (in blue) is predictable in the increasing phase of clustering. However, the Rayleigh law under-estimates the cluster density on the decreasing phase (one can attribute this underestimation to the square exponential decreasing rate of the Rayleigh law). It is always possible to perform a fitting in the decreasing phase of clustering to obtain a modified Rayleigh law capable of precisely describing the clustering process in all the phases. This task demands a considerable computational time and it is, therefore, an ongoing work. Here, only the principles of the method of describing the clustering process by a Rayleigh law (or a modified Rayleigh law) are being presented.

Moreover, the clustering process can result from two different mechanisms [McClure and Horne (2014)]: (i) through induced slip on pre-existing fractures (shear stimulation: increasing the size of existing fractures) and (ii) by creating new fractures using hydraulic fracturing technique (opening mode: increasing the number of fractures in the DFN), or by a combination of the two mechanisms. In the present work, beside the fact that our analysis is purely geomorphological, it alos considers only the first mechanism (increasing the size of fractures in a preexisting DFN). The second mechanism (adding new fractures to the DFN to increase the density) is also under investigation and constitutes, with the fitting procedure of the Rayleigh law, two main tasks in an ongoing work.

4.3.2 Size of the largest cluster in DFN

The distribution of the size of clusters is related to the previous analysis about the distribution of the cluster number. Our focus here is on the size of the largest cluster. From a hydraulical point of view, only the percolating larger clusters are of interest. In Fig. (4.6), the evolution of the size of the largest cluster in the DFN as function of the mean number of intersections per fracture ρ is presented.

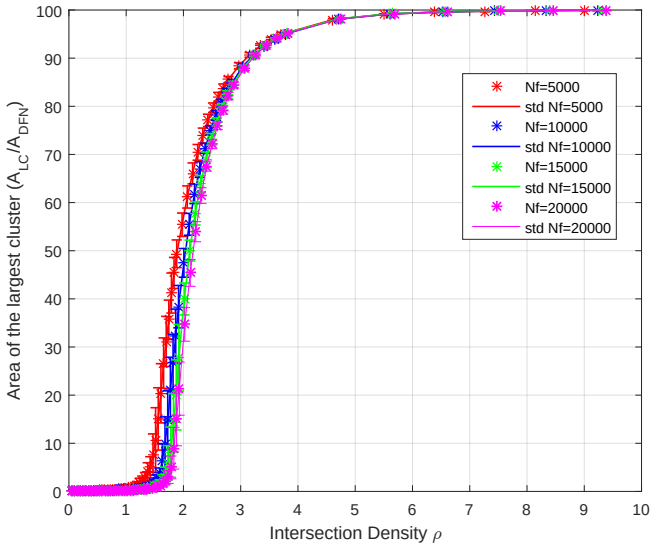

Figure 4.6: Evolution of the relative size of the largest cluster in a DFN with respect to the density ρ of the DFN.

The DFNs used are the same as in Fig. (4.3). The size of the largest cluster is presented as the percentage of the area of the largest cluster (A_{CL}) over the total area of fractures (A_{DFN}) in the DFN. Similar evolution have been observed for all DFN sizes (N_F= 5000; 10,000; 15,000 and 20,000 fractures).

Several conclusions could be made while interpreting Fig. (4.6). The first one , and the most obvious, concerns the fact that just as the density ρ become larger than the critical point σ, the size of the largest cluster increases rapidly which is coherent with the fact that the number of clusters is decreasing at similar rate (Fig. (4.3)): as the density ρ increases, the clusters collapse to form larger clusters and hence the size of the largest cluster increases. The second conclusion concerns the fast rate at which the area of the largest cluster attain roughly 100% of the total area of the DFN. As it can be seen from Fig. (4.6), at density $\rho \simeq 3$, the area of the largest cluster represents already 90% of the total area. This observation indicates that just after percolation, (remind that the critical percolation density was for mono-disperse network $\rho_C \simeq 2.178$) all the DFN will collapse in a single large cluster. This fact has an important implication on the hydraulic behavior of the DFN. It also implicates that just after percolation the majority of the network participate to the flow and hence the superposition principle for permeability upscaling could be used with the appropriate fitting.

An immediate perspective of this cluster area analysis concerns the possibility of using the repartition function of Rayleigh law (or the modified Rayleigh law) to describe the evolution of the size of the largest cluster. The idea is coherent with the previous results concerning the capability of Rayleigh law to describe the evolution of the clusters in a DFN. As mentioned earlier, these points constitute an ongoing work and only the idea and the methodology are highlighted.

4.4 Graph approach for flow simulations in DFN

Performing detailed flow simulations on the 3D fracture network is computationally very expensive. [Adler et al. (2012)] give a detailed evaluation of the CPU time needed for meshing DFNs. [Karra et al. (2018)], [Fourno et al. (2019)] also presented the computational limitations of their tools for meshing DFN. Due to these limitations, performing flow simulation on the corresponding graph of the DFN is a promising option ([Hyman et al. (2017)], [Alghalandis (2017)]). The objective of this section is to conceptualize and then implement the flow simulation on the corresponding graph of a DFN. The final purpose is to use the graph flow simulation as an alternative tool for upscaling permeability.

4.4.1 graph approach for flow: the principle of the method

The graph construction from DFN was explained in the previous chapter 3. As mentioned, two possible graph representations, corresponding to two adjacency matrices (TT for trace-trace matrix and FF for fracture-fracture matrix), can be considered. In our case, all the technical work needed to construct the corresponding graph of a DFN is already accomplished as presented in the different tools of the previous chapter. Hence, the implementation of flow simulation on the graph is presented here. The aim of the following reasoning is to present a formulation of the flow problem on each graph representation of the DFN. For clarity, the procedure is only explained for the TT graph and one can extrapolate the same procedure to the FF graph type. The differences, regarding the graph flow formulation, between the two types (TT and FF) are mentioned at the end of this subsection.

For the TT type of graph, each intersection between two fractures is a vertex. Any two vertices V_{Ti} and V_{Tj} belonging to the same fracture are connected and the the corresponding fracture presents the edge E_{ij} in a graph notations. Figure (4.7) presents an example of three fractures in a DFN and their corresponding graph attributes.

The figure is printed from a flow simulation on a DFN under Comsol. The purpose of presenting the graph attributes of a DFN in a flow simulation result is to relate the abstraction of the graph approach to the realism of direct numerical simulations. The central fracture has two intersections. The midpoint of each trace (the intersection line) represents the vertices (V_{T1} and V_{T2}). The Euclidean distance between V_{T1} and V_{T2} is the length of the edge E_{12} relating the two vertices (V_{T1} and V_{T2}). The same convention is applied to all the vertices and edges of the TT graph.

Now, let N be the number of nodes in the TT graph. If a steady state flow is assumed in the fracture network, the mass balance of fluid for any vertex V_{Ti} in the graph can be written as:

$$\sum_{j} Q_{ij} = 0 \tag{4.4}$$

where j is any vertex adjacent (connected) to the vertex i. Q_{ij} is the volumetric flow rate $[m^3/s]$ between the vertices i and j. A Darcy law is used to relate the flow rate Q_{ij} and the pressure gradient $(P_i - P_j)$ between vertices V_{Ti} and V_{Tj} through the following equation

$$Q_{ij} = \frac{K_{ij}\, A_{ij}}{\mu} \frac{(P_i - P_j)}{\Delta ij} \tag{4.5}$$

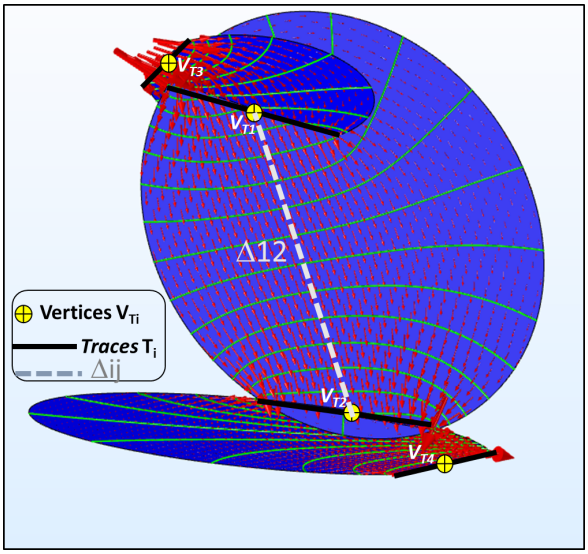

Figure 4.7: Schematic representation of the TT graph of a DFN containing only 3 fractures. The schema was taken from real flow simulation of the DFN. The red arrows represent the Darcy velocity field; the green lines represent the iso-pressures. The straight lines are the traces (fracture intersections). Yellow circles present the vertices of the TT graph. Gray discontinuous lines are the edges of the TT graph.

where $K_{ij}\,[m^2]$ is the permeability of the fracture relating V_{Ti} and V_{Tj}, $\mu\,[Pa.S]$ is the fluid viscosity, Δ_{ij} is the Euclidean distance between V_{Ti} and V_{Tj} and A_{ij} is the transverse area throw which the fluid flows between vertices V_{Ti} and V_{Tj}. The choice of the area A_{ij} is assumed similar to [Karra et al. (2018)] by the following approximation

$$A_{ij} = a_{ij}\frac{(L_{Ti} + L_{Tj})}{2} \tag{4.6}$$

where a_{ij} is the aperture of the fracture connecting the two vertices V_{Ti} and V_{Tj}, L_{Ti} and L_{Tj} are the lengths of the traces T_i and T_j.

Now, combining Eq. (4.4) and Eq. (4.5), a unified equation relating the pressures at the vertices of the graph is obtained as follow

$$\begin{cases} \sum_j w_{ij}(P_i - P_j) = 0 \\ \\ where \quad w_{ij} = \frac{K_{ij}A_{ij}}{\mu\Delta_{ij}} \end{cases} . \tag{4.7}$$

The terms w_{ij} are the weights of the graph edges E_{ij}. Now, one can define the weighted adjacency matrix A_{TT} of the TT graph as

$$\begin{cases} A_{TT}(i,j) = w_{ij} & if\ V_{Ti}\ and\ V_{Tj}\ are\ connected \\ \\ A_{TT}(i,j) = 0 & elsewhere \end{cases} . \tag{4.8}$$

To obtain an algebraic formulation of the flow problem, a diagonal matrix D_{TT} con-

taining the degrees of the vertices is defined as follow

$$D_{TT}(i,i) = \sum_{j} A_{TT}(i,j) \tag{4.9}$$

Now, an algebraic formulation of Eq. (4.7) is obtained by

$$(D_{TT} - A_{TT})\, P = 0 \tag{4.10}$$

where P is a $[N\, X\, 1]$ vector presenting the pressures at the vertices of the graph (the unknowns). The matrix $(D_{TT} - A_{TT})$ of size $[N\, X\, N]$ is also called the Laplacian of the graph. Finally, the resolution of the steady state flow problem on the TT graph consists on the resolution of the previous linear system. To do so, one has to provide the boundary conditions. For example, if a pressure gradient is imposed between two opposed faces of the 3D domain, Dirichlet boundary conditions have to be imposed on all the vertices that intersect these opposed faces. The assignment of boundary conditions is done by adding the adequate value of pressures in the second member of Eq.(4.10). The flow on graph procedure is implemented in a suit of scripts and has been linked to the set of algorithms developed in chapter 2 for automatization purposes.

To resume the whole procedure of resolution of the steady state flow on the associated TT graph of a typical DFN, the Fig. (4.8) depicts an example of a DFN containing $N_F = 200$ fractures, statistically oriented and randomly located in the 3D domain. The results of steady state flow simulations on the DFN are presented and their analogy with the TT graph flow simulation is presented.

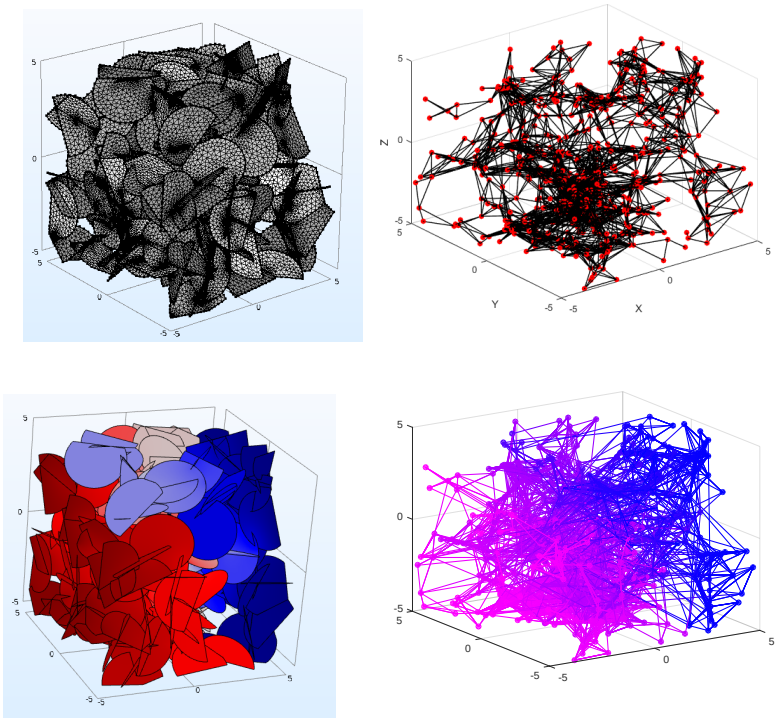

Figure 4.8: DFN and its corresponding TT graph. Top-Left: the DFN containing 200 fractures is meshed. Bottom-Left: The steady state flow simulation results: the color map corresponds to the pressure field in the DFN. Top-Right: the corresponding TT graph of the DFN (red dots represent the vertices and the black straight lines represent the edges of the graph). Bottom-Right: the results of the flow simulation on the TT graph (the color map represents the pressure field in the graph).

Once the graph flow approach is implemented, one can evaluate the gain in CPU time for flow simulations if the graph approach is used instead of the detailed flow simulation. The gain in CPU time came essentially from the fact that the meshing procedure is a very time consuming task as revealed in recent studies ([Adler et al. (2012)]; [Karra et al. (2018)]; [Fourno et al. (2019)]). In fact, the CPU time for meshing the DFN is a power function of the density of the DFN [Adler et al. (2012)], Eq.8.1). On the other hand, with the graph approach, there is no need of meshing procedure as the vertices and the edges of the graph are already determined by the Connectivity algorithm. Finally, the graph approach results on a number of degrees of freedom (DOF) orders of magnitudes lower than the DOF of the meshed DFN. The gain in CPU time by using graph approach is discussed in [Karra et al. (2018)] and here we present a simple example of similar study of CPU time gain. A 3D random DFN is generated with statistically isotropic orientation and with constant fracture radius. At first, a steady state flow simulation with imposed pressure gradient is run on a finite element simulator (ComsolMultiphysics). Then, the equivalent graph is used to run the same steady state flow simulation. The speed up is plotted in Fig.(4.9).

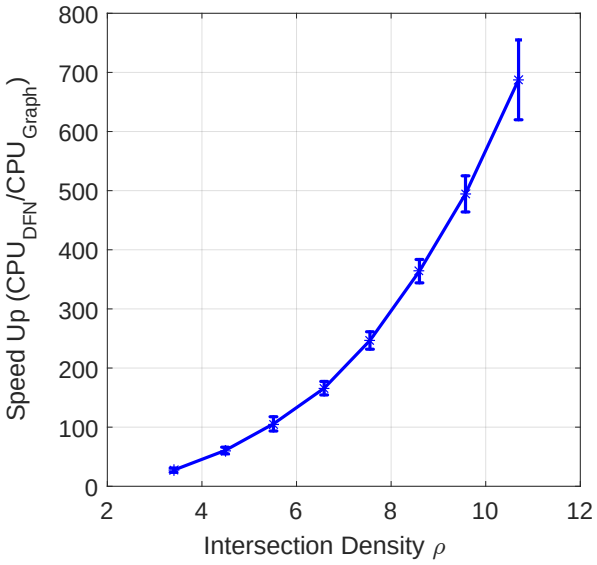

Figure 4.9: Speed up from using graph flow instead of detailed simulations in DFN. The CPU time for DFN simulation includes meshing and solving flow equation. The CPU time of graph flow simulation includes the CPU time of the Connectivity and Clustering algorithms and the resolution of the flow system.

One should emphasize at this stage that the speed up mentioned in the present study do not reveal the strength of the graph approach as we are limited (due mainly to meshing failure) to a small number of fractures (the maximum number of fracture used in the example of Fig. (4.9) was $N_F = 400$ fractures) and the maximum density was $\rho = 10$ [intersections per fracture]). We expect that the speed up will attain larger orders of magnitudes if the meshing tool used in the present study is able to handle denser and larger DFNs. The limitation of the meshing procedure in Comsol consists on a failing of the mesh even for "moderate" densities.

After this detailed presentation of the flow on the TT graph, the implementation of the

flow problem on the FF graph is now discussed with a focus on the fundamental differences between the two graph approaches (TT .Vs. FF).

At first, one can remind the main limitations of the TT graph approaches due mainly to some over simplifications. In the previous TT graph approach, the pressure is assumed to be constant at the fracture intersection. This hypothesis is not verified as it can be seen clearly from Fig.(4.7). At the vertex V_{T1}, the pressure gradient is not zero (in contrast, a large pressure gradient is observed in that intersection (see the iso-pressure green lines)). This observation was also mentioned in the work of [Karra et al. (2018)] in the context of tracer transport in graphs and they have mentioned that this under-estimation of the pressure gradient at the intersections leads to order of magnitudes under-estimation of the particle travel time in DFNs. To overcome this over-simplification, we propose a different flow approach based on the FF graph. The concept of the present approach is similar to the work of Cacas et al. (1990) with new definition of the coordinates of the vertices.

In the present version of graph (FF), the vertices are no longer the midpoints of the traces as in the TT graphs. Each fracture on the FF graph is presented by a single vertex. The coordinate of the vertex V_{Fi} is the barycenter of the traces belonging to the fracture F_i weighted by their respective trace lengths. Fig. (4.10) gives a schematic representation of the location of the vertices V_F.

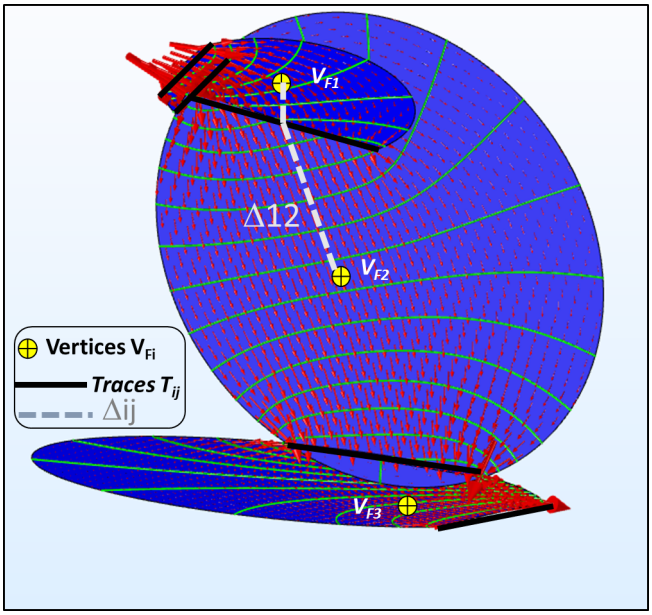

Figure 4.10: Schematic representation of a FF graph for flow on the same DFN as in Fig. (4.7)

The procedure for the implementation of the steady state flow in the FF graph is exactly the same as the on the TT graph except for the flow equation (Eq.(4.5)). In the FF graph, the new parameters of Eq.(4.5) are as follows:

- The distance Δ_{ij} is defined as the distance between V_{Fi} and V_{Fj} passing throw the midpoint of the trace T_{ij} connecting the two fractures F_i and F_j. An example of such distance Δ_{12} is presented in Fig. (4.10) with the dashed gray line.

- The permeability K_{ij} is defined as the harmonic mean of the permeabilities of the

corresponding fractures F_i and F_j weighted by the distances from the vertices (V_{Fi} .resp.V_{Fj}) to the midpoint of the trace T_{ij}.

- The flow area A_{ij} is now the trace length L_{Tij} multiplied by the arithmetic mean of the apertures (a_i and a_j) weighted by the distances from the vertices (V_{Fi} .resp.V_{Fj}) to the midpoint of the trace T_{ij}.

The new approach of FF graph is, a priori, physically more coherent with the detailed flow observation in the DFN. In contrast to the previous TT graph approach, the locations of the vertices in the FF graph are far away from the important pressure gradient observed at the fracture intersections. In this way, the hypothesis of a constant pressure at the vertices is more realistic. This physical argument was our main motivation to implement the FF graph approach to compare with the recently used TT graph approach [Karra et al. (2018)]. Once the two approaches (flow on the graphs TT and FF) are introduced and implemented, the accuracy of each approach can be revealed by comparison with detailed steady state flow simulations. This point will be highlighted in the following subsection with a focus on the ability of the two approaches to predict the equivalent permeability on the DFN in 3D.

4.4.2 Permeability estimation based on graph flow

The flow simulation on graph is performed under several approximations. These approximations concern mainly the important reduction of the number of DOF in comparison with the DFN: the pressure on each fracture in the DFN is now represented by a single value (in the FF graph) or by a limited number of pressure values proportional to the number of intersections per each fracture (in the TT graph). Approximations concern also the weights of the edges used in the two graph approaches.

The aim of this section is to compare the capabilities of the two graph approaches in estimating the equivalent permeability of 3D fracture network. To evaluate the accuracy of the graph approaches, the equivalent permeability of synthetic DFNs are first computed by direct numerical simulations using the finite elements software Comsol Multiphysics. Then, the results of the equivalent permeability are compared to the upscaled permeabilties obtained by the two variants of the graph flow approach. To obtain the upscaled equivalent permeability of 3D fracture networks from detailed numerical simualtions under Comsol, the same numerical procedure used in chapter 2 (Rajeh et al. 2019) is used. For the graph approach, the velocity field is calculated in all the edges by assuming a Darcy law relating the pressures difference between the vertices. The remaining of the upscaling procedure is the same as in chapter 2. The results of the comparisons are depicted in Fig. (4.11).

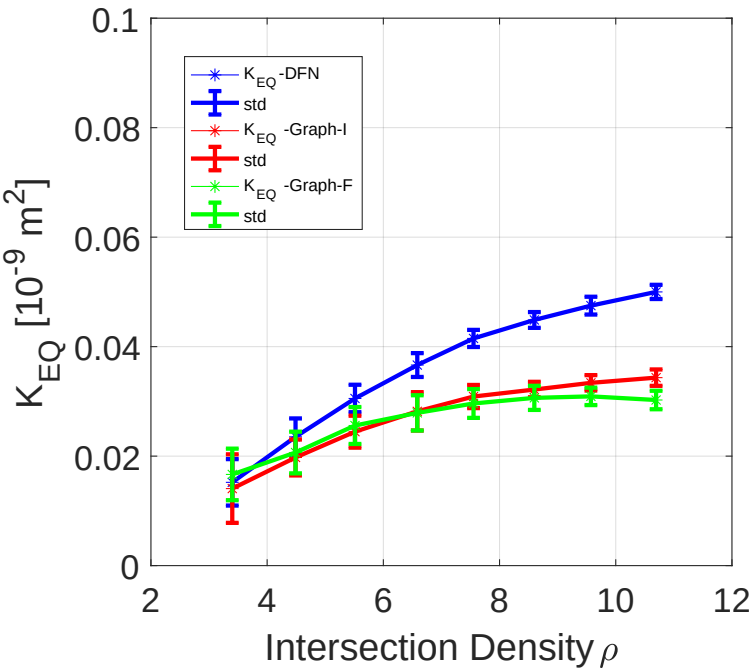

Figure 4.11: Comparing the equivalent permeability estimations: blue (DFN), red (graph of traces: TT), green (graph of fractures: FF)

The evolution of the equivalent permeability with respect to density ρ depicted in Fig. (4.11) shows that the comparison between TT and FF graphs can be separated into two regions with respect to the densityρ.

- For low densities, the FF graph estimates equivalent permeability in a relatively more precise way compared to the TT graph. This is due to the physical argument presented earlier (i.e., the location of the vertices in the FF graph are far away from the large pressure gradient zone (the intersections zone)).

- For more important densities, ($\rho \leq 5$) in Fig. (4.11), the equivalent permeability estimation by the TT graph is more accurate compared to the FF graph estimations. This can be explained by the fact that the number of DOF in the TT approach is proportional to the density ρ, however the number of DOF in the FF graph depends only on the number of fractures. In this way, in large densities, the FF graph can be seen as an over simplification of the DFN. For that reason, the values of the permeability estimated by the FF graph begin to diverge from the permeability estimated from detailed flow simulations.

- In all the density range studied here, the graph approach under-estimates the equivalent permeability of the 3D fractured medium.

To sum up, the advantages of the FF graph approach seems to be limited to low to moderate densities. However, for larger densities, the classical TT graph is more accurate in estimating the equivalent permeability of DFN in 3D. A more insightful revision of the FF approach has to be investigated in order to add more DOF to the FF graph. The

analytical solutions presented by [Noetinger and Jarrige (2012)] could be a starting point to this goal. This point is kept as perspective of this thesis.

4.5 Conclusion

As a conclusion of this chapter, topological and graph analysis are demonstrated to be powerful tools for analyzing percolation and connectivity aspects of DFN. The important conclusion can be listed as follows:

- The equivalence between the density of DFN based on the concept of excluded volume ρ_{EX} and the exact DFN density ρ is investigated. It comes out from this investigation that the equivalence ($\rho_{EX}.versus.\rho$) is sensitive to two parameters: (i) the number of fracture in the the network N_F and (ii) the fracture to domain size ratio D_F/D_{Hom}).

- The critical density of percolation was determined for mono-disperse networks. The effects of the 3D domain boundaries has been highlighted. Also, the value of the critical density $\rho_{EX,C}$ for "infinite domain" is coherent with the value found in [Mourzenko et al. (2005)] although the differences in the method of the determination of the percolaiton between their work and the present study. The difference is explained by the fact that [Mourzenko et al. (2005)] approximate circular fractures with regular polygons.

- A Rayleigh law is proposed to describe the evolution of the clustering process in fractured rocks. The physical interpretation of the clustering process and its relation to geomechanic process are highlighted.

- Steady state flow in DFN is now formulated and implemented on the equivalent graphs of DFN. Two major graph representations of the DFN are used: (i) TT graph where the vertices of the graph correspond to the traces of fracture intersections in the DFN and (ii) the FF graph where the vertices correspond to the fracture barycenters. The flow simulation on graph are used as a tool for upscaling the permeability of DFN. The results are compared to detailed flow simulation and the speed up is evaluated. It comes out that, although the graph approach is gaining recently an important interest and it is under intensive research efforts, it underestimates the equivalent permeability of 3D fractured media. More efforts on the formulation of the graph flow problem have to be adressed in the future.

Finally, one can reconfirm that the set of algorithms developed in chapter 2 present an efficient tool for analyzing the topological aspects of the DFN and enable us to make more insightful conclusion about the geometrical, topological, graph and hydraulic attributes of 3D fracture networks. The developed tools open more possibilities to investigate various aspects of DFN (percolation, clustering etc.).

Chapter 5

Application: Reservoir Scale Thermo-Hydraulic Simulations

5.1 Introduction

This final chapter treats another separate aspect of fractured rock modeling: the reservoir scale simulation. In real applications, the following consecutive tasks have to be addressed in order to model a geothermal reservoir: (i) fractured rock characterization, (ii) upscaling the physical properties of the rock and (iii) performing reservoir scale simulation to test the availability of the resource and the production scenarios.

This chapter could be viewed as the upstream of the previous fractured porous rock analysis (the consecutive analysis including the numerical generation of fractured rocks samples (chapter1), percolation analysis and upscaling (chapters 2, 3, 4)). The objective, here, is the preparation of a reservoir scale simulation toolbox (taking into account the specificity of the upscaled properties: heterogeneity and anisotropy) with a future perspective of application to a realistic case presented by the ongoing GEOTREF project.

Reservoir simulation is a crucial task in the development of geothermal energy extraction projects. The most known tool and widely used in geothermal reservoir simulations is THOUGH2 [Pruess et al. (1999)]. TOUGH2 is built on the base of a FORTRAN code and the current version 2.0 dates to 1999. While the TOUGH2 is the principal industry standard for geothermal energy simulations, many research groups have been developing alternative tools to overcome many of the THOUGH2 limitations like the lack of a proper well simulator. As an example, [Franz (2015)] proposes an alternative toolbox, called OOMPFS, for reservoir and power plant simulation adopted for geothermal energy. More recently, [Salimzadeh et al. (2018b)] published tools for modeling and simulating coupled thermo-hydro-mechanical behavior for deformable fractured geothermal systems. [Pandey et al. (2018)] have given a state of the art of the existing codes for reservoir simulation adapted to geothermal energy. The methodology and the specifications of each code are also presented.

There is a clear evidence for extreme structure heterogeneity and variations in thermo-hydraulic properties in hydrothermal systems in general [Matthäi et al. (2007)]. Similarly, in EGS (Enhanced Geothermal Systems) there is a great variability and heterogeneity in permeability due to the fracturing process. Hence, there is a particular need for the treatment of reservoir heterogeneity and anisotropy. Hence, the purpose of this chapter is to develop a numerical code for reservoir thermo-hydraulic simulation capable of taking into account these two aspects (i.e., heterogeneity and anisotropy). The code developed

in the present work, called hereafter GeothFoam, is developed using the open source code OpenFoam. The presentation of the code and its capabilities is the subject of a dedicated section in this chapter.

In the previous chapters, our focus was on the analysis of the geometrical and topological properties in the aim of obtaining equivalent properties of the fractured medium at large scale (i.e., the reservoir scale). Before performing numerical simulation at reservoir scale to describe the functionality of the geothermal reservoir, one have to address the mathematical formalism to model flow and heat transfer at reservoir scale with the upscaled properties. The system of equations modeling the flow and heat transfer in equivalent fractured porous media is obtained by the volume averaging theory [Whitaker (1986)]. The details are not shown here as the theoretical derivation of these macroscale equations is not the focus of this chapter.

This chapter is presented as follow. First (Sect. (5.2)), the macroscale (reservoir scale) equations for modeling the flow and heat transport are presented. Also, a scale analysis is presented in order to understand the physical mechanisms described by the mathematical model. The "GeothFoam" thermo-hydraulic solver developed with the toolbox OpenFoam is presented in Sect. (5.3) with several benchmark tests for validation. Finally (Sect. (5.4)), a typical hypothetic example of geothermal system containing injection and production wells is presented.

5.2 Macro-scale governing equations of flow and heat transport

5.2.1 Mathematical model for flow and heat transport:

Before dealing with the governing equations, a scale separation has to be addressed. As it is mentioned in the first chapter, fractures can be found at various scales from mm to km. Two essential scales can be introduced: (i) the local scale and (ii) the macro scale. The local scale (the green box in Fig. (5.1)) has a typical size of a single fracture including its surrounding porous matrix. The large scale (the black box in Fig. (5.1)) corresponds to the reservoir scale (i.e. all the fractured rock containing a large number of fractures (e.g., millions) and a large volume of the surrounding rock ($\sim Km^3$).

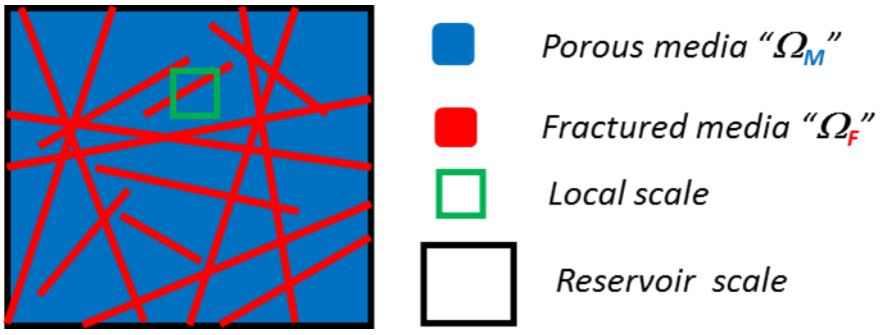

Figure 5.1: Schematic representation of the different scales of the problem

5.2.1.1 At local scale:

The governing equations for flow are derived by applying the mass conservation principle and the Darcy law for velocity. The resulting system of equations representing the two

medium and local scale (porous and fractures) is the following

$$\begin{cases} C_M\,\theta_M\,\frac{\partial P_M}{\partial t} = div\left(-\frac{K_M}{\mu}\,grad\,(P_M)\right) + Q_M & in\,\Omega_M \\ \\ C_F\,\theta_F\,\frac{\partial P_F}{\partial t} = div\left(-\frac{K_F}{\mu}\,grad\,(P_F)\right) + Q_F & in\,\Omega_F \end{cases} \tag{5.1}$$

where

1. C_M, C_F are the compressibility coefficients $[Pa^{-1}]$ for matrix, resp. fracture.
2. θ_M, θ_F are the porosity [-] for matrix, resp. fracture.
3. P_M, P_F are the pressures $[Pa]$in matrix, resp. fracture.
4. K_M, K_F are the permeabilities $[m^2]$ of matrix, resp. fracture. At this scale, the permeabilities are scalar for the porous matrix and a diagonal tensor for the fracture.
5. μ is the fluid viscosity $[Pa.s]$.
6. Q_M, Q_F are the source term $[s^{-1}]$ for matrix, resp. fracture.

In the previous equations, Ω_M and Ω_F represent the matrix and fracture domain respectively.

The coefficients "C" are specific storage coefficients, or "capacities". They express the capacity of the media to store or drain due to a unit variation of pressure, caused solely by compressibility effects. Thus, it is assumed that both media ("matrix" and "fractures") react like elastic isotropic continuum to pressure changes. An increase in pressure P_M allows storing more water in the matrix medium; and an increase in pressure P_F allows storing more fluid in the fracture system.

The governing equations for heat transport are derived from the energy conservation principle in porous media formulated with the advection diffusion equation. The resulting system of equation at local scale is the following

$$\begin{cases} \rho\,\theta_M\,Cp_M\,\frac{\partial T_M}{\partial t} = div\,(\theta_M\,\lambda_M\,grad\,(T_M)) - \,div\,(\rho\,Cp\,V_M\,T_M) + H_M & in\,\Omega_M \\ \\ \rho\,\theta_F\,Cp_F\,\frac{\partial T_F}{\partial t} = div\,(\theta_F\,\lambda_F\,grad\,(T_F)) - \,div\,(\rho\,Cp\,V_F\,T_F) + H_F & in\,\Omega_F \end{cases} \tag{5.2}$$

where

1. Cp_M, Cp_F are the specific capacity $[\frac{KJ}{Kg.K}]$ of matrix, resp.fracture.
2. ρ is the fluid density $[\frac{Kg}{m^3}]$.
3. λ_M, λ_F are the thermal conductivity $[\frac{w}{m.K}]$ of matrix, resp.fracture. At this scale, the thermal conductivities are scalar for both media.
4. V_M, V_F are the darcy velocity $[\frac{m}{s}]$ in matrix, resp. fracture.
5. T_M, T_F are the temperature $[K]$ of the matrix, resp. fracture.
6. H_M, H_F is the heat source term in $[\frac{w}{m^3}]$.

Note that, in the previous heat transfer formalism, only the heat conduction and the advection mechanisms are taken into account. The hydrodynamic dispersion is therefore not taken into account. Elaborated models for hydrodynamic dispersion in heat transfer can be found, for example, in [Kaviany 1995].

5.2.1.2 At macro scale (reservoir scale)

At macroscale, two superposed medium are represented by dual-medium models.

The dual model was first theoretically developed by [Barenblatt et al. (1960)] in the context of flow in highly connected fracture network imbedded in a porous matrix of low permeability (Fig. (5.2) on the left). [Warren and Root (1963)] were the first to introduce the concept of dual-porosity models into petroleum reservoir engineering. Their idealized model of a highly interconnected set of fractures which is supplied by fluids from numerous small matrix blocks is shown in Fig. (5.2) on the right. Their model was later extended by [Odeh (1965)]. [Kazemi et al. (1976)] has incorporated the dual-porosity concept into a numerical model, with application to fluid flow on a large scale.

It is important to mention that the dual porosity-dual permeability models was proposed initially in an empirically manner. It is later that theoretical development by [Whitaker (1986)] established mathematically the dual model. Some simplified models from this original expression are generally used. We can mention here the most known: the Dual porosity-simple permeability model. In the latter one, the permeability of the matrix K_M is neglected.

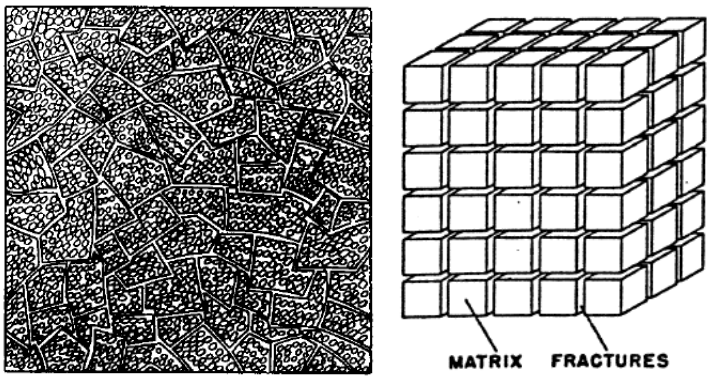

Figure 5.2: The dual medium model of fractured porous rocks as represented initially by [Barenblatt et al. (1960)] (left) and as idealized by [Warren and Root (1963)] (right)

To move from local to reservoir scale system of equations; an upscaling procedure has to be performed. The theoretical procedure of upscaling can be found in the work of ([Whitaker (1986)] among others). Here, only the mathematical dual models at reservoir scale are presented.

The governing equations for flow at reservoir scale are

$$\begin{cases} C_{M,EQ}\,\theta_{M,EQ}\,\Phi_m \frac{\partial\{P_M\}}{\partial t} = div\left(-\frac{K_{M,EQ}}{\mu}\,grad\left(\{P_M\}\right)\right) & in\ \{\Omega_M\} \\ -\alpha_H\left(\{P_M\}-\{P_F\}\right)+\{Q_M\} & \\ & \\ C_{F,EQ}\,\theta_{F,EQ}\,\left(1-\Phi_m\right)\frac{\partial\{P_F\}}{\partial t} = div\left(-\frac{K_{F,EQ}}{\mu}\,grad\left(\{P_F\}\right)\right) & in\ \{\Omega_F\} \\ +\alpha_H\left(\{P_M\}-\{P_F\}\right)+\{Q_F\} & \end{cases} . \tag{5.3}$$

The subscripts "EQ" mean that the concerned property is an equivalent property that has been upscaled from local scale to reservoir scale. Specifically, the equivalent permabilities are expected to be tensorial fields as a result of the upscaling

Note that we have distinguished here volume fractions Φ from porosities θ. The pressures "$\{P\}$" [Pa] in the matrix and fractures are averaged over the upscaled unit volume or block. The intrinsic permeabilities "K_{EQ}"[m2] are the equivalent upscaled permeabilities for each continuum, defined over the same scales as pressure. They are here positive second rank tensors. The new term $\alpha_H[Pa^{-1}s^{-1}]$ represents the mass exchange coefficient between fractured and porous medium. It quantifies how much volume of fluid is exchanged between fractures and matrix blocks as a result of a unit pressure difference $\{P_M\} - \{P_F\}$ between the fractured and the porous medium.

The research of the suitable fracture-matrix exchange coefficient α_h has been under intensive research effort in recent decades. Several methods have been used and can be classified in four major types, as suggested by [Landereau (2000)], depending on the method used to estimate the exchange coefficient:

- Asymptotic analysis([Huyakorn et al. (1983), Dykhiusen (1990)],
[Ziemmerman et al. (1993), Lim and Aziz (1995)]etc.)
- Volume averaging([Whitaker (1986)],
[Quintard and Whitaker (1996), Landereau (2000)]etc.)
- Laplace transformation ([Van Genuchten et al. (1984), Barker (1985)],
[Gerke and Van Genuchten (1993)]etc.)
- Random walk [Noetinger et al. (2001)]

The governing equations for heat transport at reservoir scale can be written as

$$\begin{cases} \rho\,\theta_{M,EQ}\,Cp_{EQ}\,\Phi_m\frac{\partial\{T_M\}}{\partial t} = div\left(\theta_{M,EQ}\,\lambda_{M,EQ}\,grad\left(\{T_M\}\right)\right) & in\,\Omega_M \\ -div\left(\rho\,Cp_{EQ}\,\{V_M\}\,\{T_M\}\right) - \alpha_T\left(\{T_M\} - \{T_F\}\right) + \{H_M\} & \\ & \\ \rho\,\theta_{F,EQ}\,Cp_{EQ}\,\frac{\partial\{T_F\}}{\partial t} = div\left(\theta_{F,EQ}\,\lambda_{F,EQ}\,grad\left(\{T_F\}\right)\right) & in\,\Omega_F \\ -div\left(\rho\,Cp_{EQ}\,\{V_F\}\,\{T_F\}\right) + \alpha_T\left(\{T_M\} - \{T_F\}\right) + \{H_F\} & \end{cases} . \tag{5.4}$$

Similarly to hydraulic system of equations, the subscripts "EQ" mean that the concerned property is an equivalent property that has been upscaled from local to reservoir scale. Specifically, the equivalent thermal conductivities are expected to be tensorial fields as a result of the upscaling.The temperatures "$\{T\}$" $[K]$ in the matrix and fractures are averaged over the upscaled unit volume or block.

Note that the dual medium models (for flow or heat transport) are only possible mathematical models to describe the flow and transport phenomena at large scale. Their applicability's are debatable. The dual models as presented here constitute the generalized models and it is always possible to extract more simplified model by deleting the exchange term in one or both systems and hence obtain an equivalent single medium model. The choice of the model is dependent on a priori scale analysis.

5.2.2 Scale analysis

Given the systems of equations presented in the previous section, several dimensionless numbers can be defined in order to perform a scale analysis. The scale analysis concerns the comparison between different time and length scales corresponding to different physical phenomena that may occur in geothermal problems. The scale analysis permits to differentiate different competing phenomena. Here, two types of scale analysis are discussed:

- Hydraulic time scale

In general, the hydraulic time scale can be expressed as $t_H = \frac{L}{U}$, where L is a characteristic length of the medium (fracture or matrix) and U is Darcy velocity (for fracture or matrix). This time scale gives an idea about how fast the flow occurs in a particular medium. The hydraulic time scale for both systems is expressed by the physical properties of the medium as follow:

$$\begin{cases} t_{H,M} = \frac{\mu C_M L_M^2}{K_M^2} \\ \\ t_{H,F} = \frac{\mu C_F L_F^2}{K_F^2} \end{cases} \tag{5.5}$$

The importance of this time scales can be highlighted while addressing the applicability of the dual medium model: the dual model is used under the three following hypothesis: (i) the fracture network is highly connected (dense networks), (ii) the matrix blocks present the quasi totality of the volume and (iii) the relaxation time scales for fracture (t_F) must be very low compared to the relaxation time of matrix (t_F) (i.e., $t_F << t_M$). Hence, the comparison of the hydraulic time scales of fractured and porous media is a key factor in order to use or not a dual medium model.

- Thermal time scale

The thermal time scale concerns the heat diffusion mechanism in the medium. The thermal diffusion time scale can be expressed as

$$\begin{cases} t_D = \frac{L^2}{D} \\ D = \frac{\lambda}{\rho C p} \end{cases} \tag{5.6}$$

where D is the thermal diffusivity $[m^2/s]$. The previous coefficient is defined for the fracture and the matrix domain respectively.

With the previous two time scale, a dimensionless Peclet number could be defined as a ratio between the conduction time scale and the hydraulic time scale (which is effectively the advection time scale),

$$Pe = \frac{t_D}{t_H}. \tag{5.7}$$

As it can be easily seen, this number can evaluate the dominant heat mechanism of transport (advection or diffusion). Similarly to the hydraulic time scale analysis, the dimensionless Peclet number is an indicator of whether or not a dual medium model is useful or not in heat transfer. If diffusion is the dominant mechanism, the diffusion time is very fast compared to the advection time scale (i.e., $t_D << t_H$). In the latter case, and as the thermal diffusivity in the two medium is generally not very different (i.e., $D_F \simeq D_M$), the dual medium model for heat transfer is not necessary. An example of thermal diffusion dominant case is given at the end of this chapter.

5.3 Finite volume simulation in OpenFoam

5.3.1 Set-up of the model in OpenFoam

This section presents, how to code, compile, per-process, run and post-process a simulation problem involving flow and heat transfer in a geothermal reservoir on OpenFoam.

OpenFOAM ("Open source Field Operation And Manipulation") is a C++ suit of programs for the development of numerical solvers based on the finite volume method [Jasak et al. (2007)]. The OpenFoam toolbox contains pre-/post-processing utilities helping to customize the numerical stimulation of problem involving continuum mechanic, chemical processes etc.. The code is released as free and open-source software under the GNU General Public License. The following figure presents the flowchart of the OpenFoam toolbox.

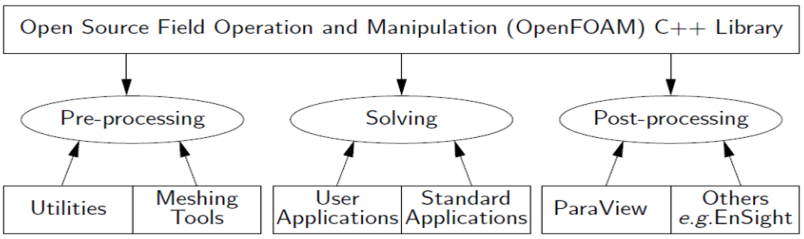

Figure 5.3: Flowchart of OpenFoam

To setup the model corresponding to the equations (Eqs. (5.3,5.4) established in Sect. (5.2) a personalized solver called "GeothFoam" has been developed. The disctretization in space and time and the solving of the resulting linear systems, is done in a single "main" code in C++ language. The fact that a single main code is necessary for our personalized solver is the major advantage from object-oriented code, which enables developers to work at a high level of abstraction. However, the developer needs to be familiar with an important amount of key-words and key-procedures proper to OpenFoam. Once the personalized "GeothFoam" code is elaborated, it is compiled and examples of coupled thermo-hydraulic problem can be run. In the following table, the properties involved in the system of equations are listed with a specification of their heterogeneity and anisotopy. This table corresponds to the present capabilities of "GeothFoam" solver at the moment of writing this thesis.

Property	Heterogeneous (Yes/No)	Scalar/Tensor	Time Dependent
C	Yes	Scalar	No
θ	Yes	Scalar	No
Φ	Yes	Scalar	No
μ	No	Scalar	No
ρ	No	Scalar	No
Cp	Yes	Scalar	No
K	Yes	Tensor	No
λ	Yes	Tensor	No
α	Yes	Scalar	No

Table 5.1: The flexibility of GeothFoam regarding heterogeneity, anisotropy and time dependent character of the physical properties of the medium.

For sake of clarity, the technical details of the implementation of the model in OpenFoam are not shown here and the procedure can be found in the OpenFoam guide for programmers. However, one can highlight the main advantages and limitations of the use

of OpenFoam for reservoir simulation. The object orientation and operator overloading of C++ has enabled us to work at a very high level of abstraction. Hence, it possible to manipulate the set of partial differential equations that describe the geothermal problem and customize the solver "GeothFoam" to each class of cases that needs to be solved. This is the main motivation for using OpenFoam, rather than other existing tools. The main limitations of the use of OpenFoam, in our point of view and also as revealed by OpenFoam users (e.g., Soulaine (2013)), are (i) the amount of time needed to handle the procedure and (ii) the difficulty to handle more deep layers of the C++ structure if it is needed.

Finally, one should note that OpenFoam is used as a geothermal reservoir simulator by [Thorvaldsson et al. (2015)] taking into account two-phase flow among other capabilities.

5.3.2 Comparison finite elements (Comsol Multiphysics) .Vs. finite volume (OpenFoam)

Once the personalized code "GeothFoam" is compiled, its validation has to be done. The validation step consists on a benchmark test with the finite element commercial solver Comsol Multiphysics. The term "Benchmark" may be viewed as an over-qualification of the comparison procedure as, in general; the benchmark tests are multi-laboratory exercises in which different codes are compared for validation and efficiently comparison. Here, as two different tools (Comsol and OpenFoam) are used in the present thesis, the comparison is performed without involving external parts.

To do the benchmark, series of tests have been prepared in the two softwares. The preparation procedure consists on building the geometry, setting the heterogeneous fields, meshing etc. The necessary pre-processing tools are automatized by Matlab scripts. The benchmark is done with an increasing degree of complexity of the cases: for example, moving from homogeneous to heterogeneous media, from isotropic to anisotropic properties etc. At the moment of writing this thesis, and although the thermo-hydraulic system of equations has been implement in GeothFoam, only benchmarks on the hydraulic part have been performed. In the following, three examples of hydraulic simulation at reservoir scale are presented in three different cases in order to compare the two softwares in an increasing degree of complexity. In all the case the mesh consists on 10,000 elements.

- Case 1: Homogeneous and Isotropic medium with No source-term

We begin by comparing the hydraulic results of the two solvers. At first, a 2D case with a square domain ($1x1[m]$) is prepared for both solvers. The permeability of the medium is homogeneous and isotropic $K = 1e^{-12}m^2$. Initially, the pressure in the medium is constant $P_0 = 10^5[Pa]$. The pressure at the boundary "$x = x_{min}$" is fixed $P(t, x = x_{min}) = 10^6[Pa]$. The other boundaries are set to no-flow boundary conditions. Probes have been placed at different locations in the medium and the evolution of the pressure with respect to time is observed. The pressure evolution is recorded on the different probes and an example of the results of the comparison is shown in Fig. (5.4).

The pressure evolution in the previous figure corresponds to a probe placed at the location $x = 0.2m, y = 0.2m$. The pressure remains equal to the initial value until the pressure diffusion attains the location of the probe. Then, the pressure will increase until attain the imposed boundary value. The equivalence of the results of the two codes is perfect. Thes results confirm the good set up of the numerical code in OpenFoam.

- Case 2: Homogeneous and Anisotropic medium with Source-term

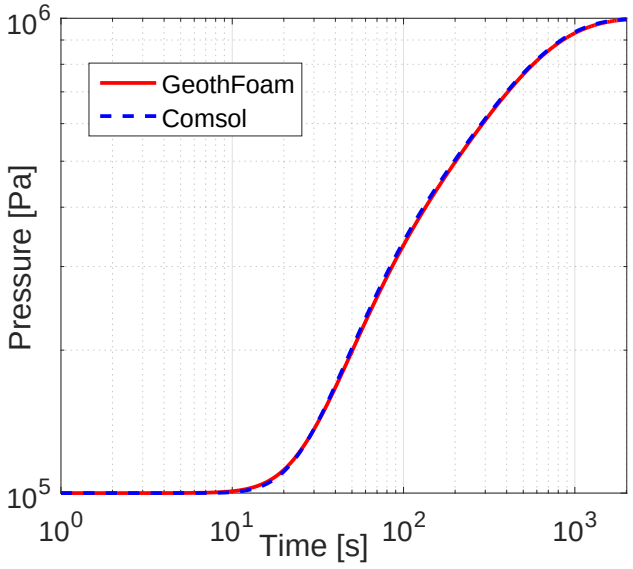

Figure 5.4: Pressure evolution comparison between GeothFoam and Comsol solvers. The boundary conditions are of Dirichlet type in x=0 and no-flow elsewhere. There is no source term in this case. The permeability of the medium is isotropic and homogeneous $K = 1e^{-12}m^2$. The CPU times of the simulation is 9 and 10s for GoethFoam and Comsol respectively.

Once the isotropic case validated, anisotropic permeability cases have been tested. Remind that the proposed code is intended to simulate large scale reservoirs where the properties are expected to be heterogeneous and anisotropic due to the fact that they are the results of the upscaling procedure. To test the capability of GeothFoam to handle anisotropic properties, a test case is designed to compare the hydraulic outputs of GeothFoam solver with Comsol. The case is a similar two dimensional homogeneous medium but with anisotropic permeability. All the boundaries of the domain are set to no-flow boundary conditions. A source term is placed at the middle ($S(x = 0.5, y = 0.5) = 1[s^{-1}]$). The permeability is tensor of the form:

$$K = \begin{pmatrix} K_{xx} & K_{xy} \\ K_{yx} & K_{yy} \end{pmatrix} \tag{5.8}$$

We tested the pressure evolution in probes at different locations while varying the ratios K_{xx}/K_{yy} and K_{xx}/K_{xy} . An example of results at probe $(0.2, 0.2)$ with an anisotropy of $K_{xx} = 10^{-10}, K_{xy} = 5.10^{-10}, kxy = 10^{-11}$ is presented in Fig.(5.5).

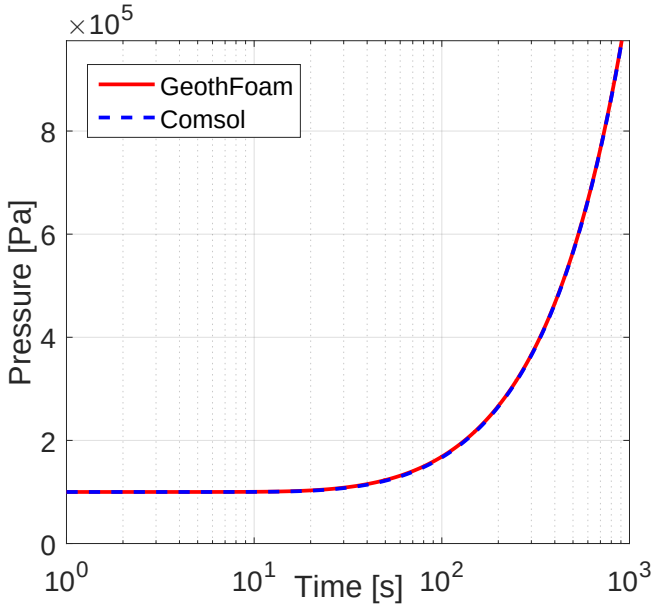

Figure 5.5: Pressure evolution comparison between GeothFoam and Comsol. The boundary conditions are of now-flow type. A source term is presented at the center of the medium. The permeability of the medium is anisotropic. $K_{xx} = 10^{-10}, K_{xy} = 5.10^{-10}, kxy = 10^{-11} m^2$

The results shown in Fig. (5.5) confirm the capability of the GeothFoam toolbox to handle correctly the hydraulic problem with anisotropic properties. Other similar cases have been addressed to further validate the developed tool. However, one has to mention that the Comsol Multiphysics finite element solver is taken as a reference which can be seen as a debatable statement. Ideally, the benchmark tests have to be performed with different research groups to compare, in the aim of improvement, different codes.

- Case 3: Heterogeneous and Anisotropic medium with Source-term

A more general case is now presented. The following example contains a 2D case of a heterogeneous anisotropic medium with a source term placed at its center. Fig. (5.6) presents the test case with four different regions in term of permeability.

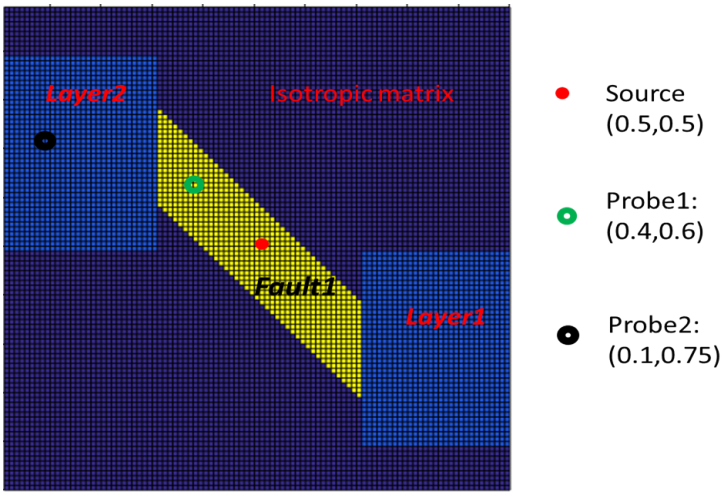

Figure 5.6: Anisotropic permeability field for the benchmark test 3.

Two layers (layer1 and layer2) with a diagonal permeability tensor (i.e., $K_{xy} = 0$), a fault with a full permeability tensor ($K_{xy} \neq 0$) and an isotropic porous matrix. The benchmark results are shown in Fig. (5.7).

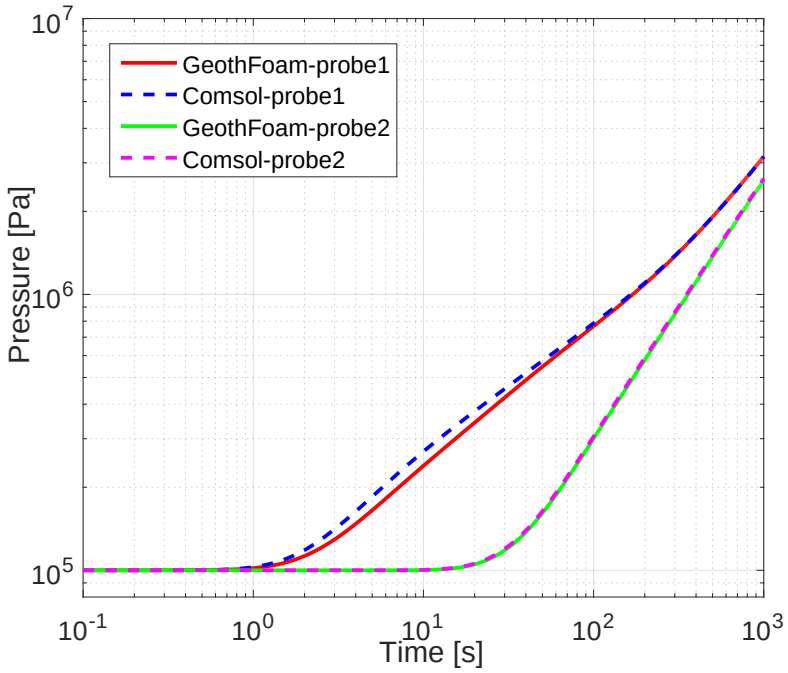

Figure 5.7: Comsol. Vs. GeothFoam Benchmark for a heterogeneous field of anisotropic permeability. Probe 1 corresponds to the location (0.4,0.4) and probe 2 corresponds to (0.25,0.1) in a 2D domain of size [1x1 m]. Straight lines correspond to the results of Geothfoam and discontinuous lines to Comsol.

The pressure evolution at probe 2 (0.25, 0.1) depicts a perfect agreement between the pressure evolution calculated by the two solvers (Comsol and GeothFoam) for all time steps. For probe1 (0.4, 0.4), which is located between the source and the discontinuity of the permeability tensor, a slight difference between the results of the two solvers can be seen in earlier time steps. The discrepancy between the two solvers can be understood since, at earlier times, the pressure gradient around the source is very important. Moreover, the discontinuity of the permeability tensor has to be approximated in the finite volume or in the finite element discretization. It has been observed that the difference in the results of Fig. (5.7) reduces if the discretized time step Δt is reduced and/or the mesh is refined.

To conclude this part, we can mention that many other benchmark tests are under investigations and more improvements are ongoing. The already tested cases have made a relative confidence on GeothFoam as a solver for flow and heat transport in heterogeneous and anisotropic 3D media.

5.4 Application: example of injection-production system in geothermal reservoir

As the aim of this thesis is to apply the developed theoretical and numerical tools presented in the previous chapters to geothermal reservoir, an academic case of geothermal energy extraction is addressed in this section. An example of a 3D domain containing two wells is presented in Fig. (5.8). The colors refer to the permeability heterogeneity. The typical well radius is between 10 cm and 20 cm. This small size of wells compared to the 3D domain size induces several meshing problems. Meshing has to be refined near the well in order to capture the important hydraulic and thermal gradients during injection or production of fluid and heat. An example of mesh refinement is presented in Fig. (5.9). The meshing procedure, in the present case, has been implemented in a manner to maintain mesh conformity as it can be seen in the zoom of Fig. (5.9).

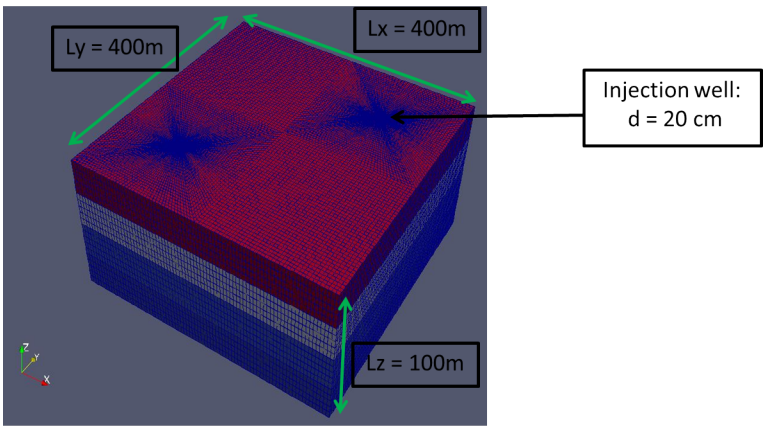

Figure 5.8: Example of two wells in a geothermal system. The mesh consists of 700,000 voxels.

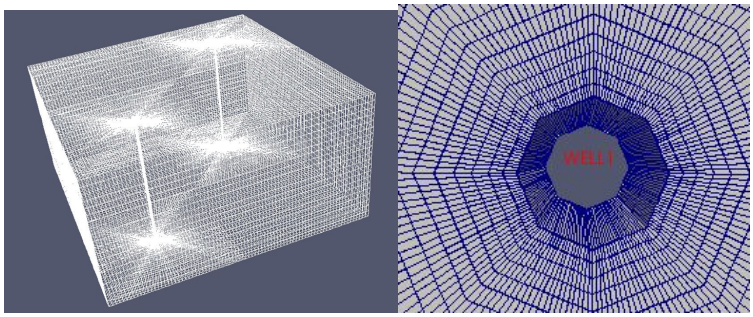

Figure 5.9: Mesh refinement near wells. The mesh is constructed in a manner to preserv conformity which is an important point for computational efficiency.

A coupled thermo-hydraulic simulation has been run on the previous example. The simulation was run in transient regime to see the transientevolution of pressure and temperature in the reservoir. The energy extracted from the production well could therefore be calculated a posteriori by calculating the evolution of enthalpy with time. In this simulation, the initial pressure in the reservoir is ($P_F = P_M = 10^5 Pa$) and the initial temperature is ($T_M = T_F = 480K$). The pressure at the injection well was set to $P_{inj} = 10^6 Pa$. The pressure at the production well is maintained at $P_{prod} = 10^5 Pa$. The injection temperature is $T_{inj} = 300K$.

The interest of reservoir simulation is to have an access to relevant parameters to the state of the reservoir at any time. The following figure depicts an example of the evolution of temperature with respect to time. In this example, the parameters have been chosen to results in a high Peclet number which results on advection dominant regime. As the heterogeneity of the example studied in this section is a stratified heterogeneity, the temperature at different layers is presented (Fig.(5.10)). The cooling of the reservoir is very fast in the more permeable layers as the advection is the dominant mechanism of transport in this example.

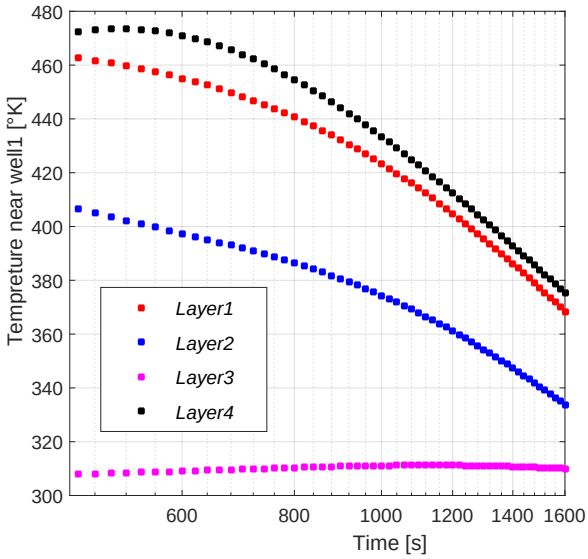

Figure 5.10: Temperature near the injection well at different layers. The probes are placed at positions (70, 70) in the (x, y) plane. The z coordinates of the probes are changed from one layer to another.

The following figure depicts an example of the evolution of pressure (in fractured medium and in the porous matrix) with respect to time. As the permeability of the fractured medium is higher than the matrix permeability, one can see (Fig. (5.11)) a fast stabilization of the pressure in the fractured medium compared to the porous matrix. Similarly, the evolution of temperature in different location in the reservoir can be visualized at each time step. In this example the Peclet number is very low which results on a conduction dominant regime. This can be seen in the temperature evolution at different locations between the two wells. The evolution of the temperature in the fractured and the porous media is approximately the same.

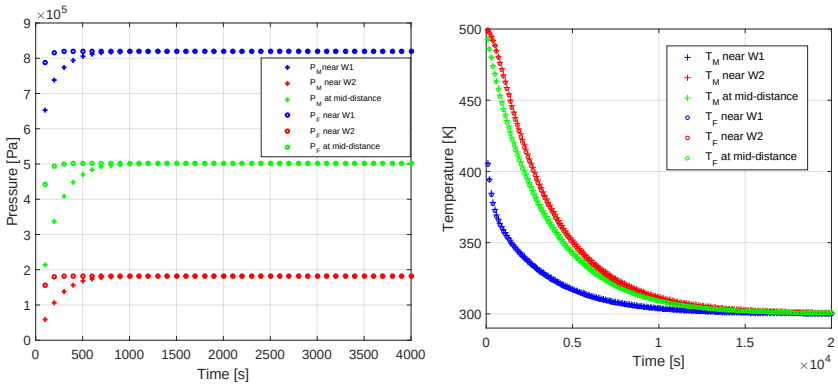

Figure 5.11: Left: Pressure transient evolution between wells. Right: temperature transient evolution between wells.

5.5 Conclusion

In this final chapter, coupled thermo-hydraulic model at reservoir scale is presented. A scale analysis has also been presented to enable analyzing the relative importance of key physical phenomena in geothermal problems. The choice of the dual model is debatable and dependent on the scale analysis of each particular problem. The double system of equations (double medium model for flow and heat transport) is the more general case. The resulting systems of equations are numerically solved in 3D by developing a solver labelled "GeothFoam" which is being developed using the open source finite volume code "OpenFoam". Meshing and simulation setup are briefly presented. The main motivation behind the development of GeothFoam is to have a solver capable of handling the anisotropy and heterogeneity of the permeability and the conductivity fields. The permeability tensor fields are the results of the upscaling procedure investigated in this thesis. This point is important, regarding that the developed upscaling methodology in the previous chapters, leads systematically to a tensor field of permeability. The solver GeothFaom has been under a continuous benchmark tests to verify its validity as a tool for handling anisotropy and heterogeneity in 3D. To do so, series of comparison tests with the finite element solver Comsol Multiphysics have been performed. The results of the hydraulic benchmarks confirm with confidence that GeothFoam is capable of resolving flow problems in a context of heterogeneity and anisotropy. A typical example of a system of injection-production wells is presented. The specific mesh refinement near wells has been successfully addressed. Typical results of the evolution of pressure and temperature at different locations in a 3D reservoir are presented and interpreted.

It comes out from the results of this chapter that OpenFoam is a suitable tool for reservoir simulation as it handles in a flexible way the heterogeneity and the anisotropy of the medium. Also, the well meshing problem can be addressed with the mesh refinement capabilities of OpenFoam. It is important to mention that the reservoir simulation tools using OpenFoam are under validation and improvement efforts. This ongoing works has another perspective which is the link between the reservoir simulator and a well simulator (W1D) developed in the context of the same project GEOTREF.

Finally, this chapter has to be placed in its context relative to the previous chapters and relative to the GEOTREF project. The reservoir simulator under development with

OpenFoam is the final step of a series of steps that begin with the numerical generation of the fractured porous rock, then the procedure of upscaling (including the percolation analysis) and finally an upscaled tensorial field of permeability will constitutes the input of the reservoir simulator. Concerning the GEOTREF project, the reservoir simulator and its solver GeothFoam are intended to be related to the geomodel of the geothermal reservoir developed under the geomodeler (GOCAD) and to be applied to the real case of Vieux-Habitant geothermal reservoir (France). The 3D geomodel has been developed by several research group in the frame of the project. The following figure shows a conceptual model of the reservoir.

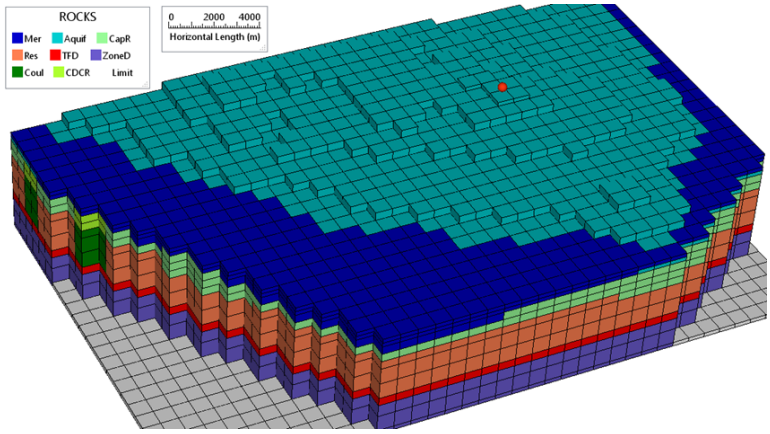

Figure 5.12: Conceptual model for the Vieux-Habitants Reservoir (GEOTREF project), adapted from [Garcia et al. (2018)].

General Conclusion (English)

In a context of energy transition, geothermal energy is gaining more and more place in the mix of energy solutions. The French GEOTREF project is part of this transition perspective. This thesis is part of this project with the objective to provide theoretical and numerical tools for insightful understanding of fractured geothermal reservoirs.

Two main aspects can be distinguished in the work of this thesis. The first one was dedicated to the numerical development of a set of algorithmic tools allowing the analysis and the understanding of the thermo-hydraulic behavior of a geothermal reservoir constituted of a fractured permeable rock. The second part concerns a set of proposals and analysis concerning upscaling, percolation, Clustering and the use of graph theory to simulate fractured rocks. The conclusions regarding these two main components can be summarized as follows:

Regarding the development of numerical tools:

• A numerical upscaling platform using Comsol Multiphysics-Matlab (LiveLink) coupling is now operational. This tool allows, as a main task, to obtain equivalent permeabilities of synthetic numerical samples of the fractured media by the detailed resolution of the 3D flow problem (mesh, finite element resolution, averaging, determination of the VER, etc.).

• A set of geometric and topological analysis algorithms for 3D fracture networks has been developed. These tools make possible, given a network of 3D planar fractures, to calculate all the geometric attributes of these networks (intersections between fractures, lengths of traces, etc.), the clusters and the percolating clusters, dead-end clusters and finally to build the equivalent graph of the 3D fracture network, among other features.

• The resolution of flow problems on the equivalent graphs of 3D fracture networks by the construction and then the resolution of the Laplacian of the equivalent graph is now functional, with a much lower computation time than in the classical methods.

• A GeothFoam reservoir simulator has been developed with OpenFoam open source code. This tool allows the simulation of thermal-hydraulic coupling in single or double media model at the scale of a geothermal reservoir in the presence of wells. GeothFoam makes possible to take into account heterogeneity and anisotropy resulting from equivalent properties upscaling of fractured porous media. A "Benchmark" exercise has been conducted between GeothFoam and the commercial software Comsol Multiphysics to validate the proposed numerical tool.

The main new results obtained at the end of this thesis are:

• The upscaling approach by superposition formulated in the present work is an effective tool, in terms of computational efficiency, for predicting the equivalent permeability of a 3D fractured medium containing a permeable porous matrix. However, the superposition must be calibrated by empirical coefficients to take into account the connectivity of the fracture network.

• Excluded volume notion is a key parameter in measuring the connectivity of a 3D fracture network. The sensitivity of the equivalence between the excluded volume density and the average intersection number per fracture is questioned in the present work. More specifically, the sensitivity of this equivalence (Excluded density .Vs. Mean number of intersections per fracture) to the size of the 3D domain has been highlighted, which can therefore explain the sensitivity of the critical percolation density to the size of the domain. Correlations have been proposed to link the density based on the excluded volume and the intersection density computed in an exact way by the algorithms developed in this thesis.

• An empirically modified Rayleigh law can describe the geo-morphological phenomenon of fractures grouping which form clusters (Clustering) by the simple knowledge of the average number of intersections per fracture.

• The resolution of the flow on the equivalent graphs of fracture networks is a highly efficient advance from a computational point of view. However, this approach underestimates the equivalent permeability. The offset is attributed to two main factors: (i) the sharp reduction in the number of degrees of freedom (DOF) in the graph compared to the actual fracture network and (ii) the choice of the weighting mode (nodes weight in the graph).

In a more general conclusion, the numerical tools developed in this thesis are the basis of the analyzes and interpretations that have been put forward. Since these tools have taken a large part of the work done during this thesis, many of the conclusions obtained also lead to short- and medium-term perspectives. Among the prospects that can be explored in the short term (or are actually being explored), we can mention:

• Continuing the development of geometric and topological analysis tools to better handle the graph approach for fractured rocks for flow and heat or mass transport problems.

• The clustering process analysis is a promising study that can help describing and understanding the evolution of the fracture system under hydro-mechanical coupling.

• More detailed analysis of the connectivity of fracture networks is now made possible by the algorithms implemented. In particular, topological indices can be explored and proposed to calibrate the equivalent permeability calculated by the superposition method or by the graph method.

• Coupling with two-phase flow with phase change in the wells is an immediate prospect. The developed tool GeothFoam is designed to allow this coupling.

Finally, fractured porous reservoirs are an intensive and interdisciplinary field of investigation. Hydraulic-mechanical-thermal-chemical coupling is strong in the context of geothermal energy. The results and advances explored in this field of application can be directly extrapolated to other areas of application such as the geological storage of CO2 or oil and gas engineering, for example.

Conclusion Générale (Français)

Dans un contexte de transition énergétique, la géothermie prend de plus en plus de place dans le mix de solutions énergétiques. Le projet GEOTREF s'inscrit dans cette perspective de transition. Cette thèse a fait partie de ce projet afin d'apporter des éclaircissements et des outils numériques pour la compréhension et la simulation du fonctionnement d'un réservoir géothermique fracturé.

Deux volets principaux peuvent être distingués dans le travail de cette thèse. Le premier a été dédié aux développements numériques d'un ensemble d'outils algorithmiques permettant l'analyse et la compréhension du comportement thermo-hydraulique d'un réservoir géothermique constitué d'une roche perméable fracturée. Le deuxième volet concerne un ensemble de propositions et d'analyse concernant l'upscaling, la percolation, le Clustering et l'utilisation de la théorie des graphes pour simuler les roches fracturées. Les conclusions concernant ces deux volets principaux peuvent être résumées comme suit:

Concernant le développement d'outils numériques:

•Une plateforme numérique d'upscaling est maintenant opérationnelle à l'aide d'un couplage (LiveLink) Comsol Multiphysics-Matlab. Cet outil permet, comme principale tâche, d'obtenir des perméabilités équivalentes des échantillons synthétiques des milieux fracturés par la résolution détaillée du problème d'écoulement en 3D (maillage, résolution par éléments finis, prise de moyenne, détermination du VER etc.).

•Un ensemble d'algorithmes d'analyses géométriques et topologiques des réseaux de fractures en 3D a été développé. Ces outils permettent, à partir d'un réseau de fractures 3D, de calculer tous les attributs géométriques de ces réseaux (les intersections entre fractures, les longueurs des traces, etc. . .), les amas et les amas percolants, les amas en cul de sac (Dead-End), et finalement de construire le graphe équivalent au milieu fracturé 3D, parmi d'autre fonctionnalités.

•La résolution des problèmes d'écoulements sur les graphes équivalents des réseaux de fractures 3D par la construction puis la résolution du Laplacien du graph équivalent est fonctionnel.

•Un simulateur réservoir GeothFoam a été développé à partir du code open source OpenFoam. Cet outil permet la simulation du couplage thermique –hydraulique en simple ou double milieux à l'échelle d'un réservoir géothermique en présence de puits. GeothFoam permet de tenir compte de l'hétérogénéité et de l'anisotropie, en de propriétés équivalentes, des milieux poreux fracturés. Un exercice de « BenchMark » a été réalisé entre GeothFoam et le logiciel commercial Comsol Multiphysics afin de valider l'outil numérique proposé.

Les principaux résultats nouveaux obtenus à l'issue de cette thèse sont :

•La montée d'échelle par superposition formulée dans le présent travail est un outil efficace, en terme d'efficacité computationnelle, pour prédire la perméabilité équivalente d'un milieu fracturé 3D contenant une matrice poreuse perméable. Cependant, la superposition doit être calée par des coefficients empiriques pour tenir en compte de la connectivité du

réseau de fractures.

•La notion de volume d'exclusion est un paramètre clé dans la mesure de la connectivité d'un réseau de fractures 3D. La sensibilité de l'équivalence entre le volume d'exclusion et le nombre d'intersection moyen par fractures est mise en question dans le présent travail. Précisément, il a été mis en évidence la sensibilité de cette équivalence par rapport à la taille du domaine d'étude qui peut à son tour expliquer la sensibilité de la densité critique de percolation à la taille du domaine. Des corrélations ont été proposées pour lier la densité basée sur le volume d'exclusion et la densité d'intersection calculée d'une façon exacte par les algorithmes développés dans cette thèse.

•Une loi de Rayleigh modifiée peut expliquer le phénomène de groupement de fractures pour former des amas (Clustering) à partir de la simple connaissance du nombre d'intersections moyen par fracture.

•La résolution de l'écoulement sur des graphes équivalents aux réseaux de fractures est une avancée très efficace d'un point de vue computationnel. Cependant, cette approche sous-estime la perméabilité équivalente. Le décalage est attribué à deux facteurs principaux : (i) la forte réduction du nombre de degrés de liberté dans le graphe par rapport au réseau de fractures réel et (ii) le choix du mode de pondération (poids des nœuds dans le graphe).

En guise de conclusion plus générale, les outils numériques développés ont été à la base des analyses et des interprétations qui ont été avancées durant cette thèse. Ces outils ayant pris une grande partie du travail effectué durant cette thèse, beaucoup des conclusions obtenues conduisent aussi à des perspectives à court et à moyen terme. Parmi les perspectives qui ont la possibilité d'être explorées à court terme (ou qui sont effectivement en cours d'exploration), nous pouvons citer :

En guise de conclusion plus générale, les outils numériques développés ont été à la base des analyses et des interprétations qui ont été avancées durant cette thèse. Ces outils ayant pris une grande partie du travail effectué durant cette thèse, beaucoup des conclusions obtenues conduisent aussi à des perspectives à court et à moyen terme. Parmi les perspectives qui ont la possibilité d'être explorées à court terme (ou qui sont effectivement en cours d'exploration), nous pouvons citer :

• La continuation du développement des outils d'analyses géométriques et topologiques afin de mieux maitriser l'approche graphe pour les roches fracturées pour les problématiques d'écoulement ou de transport de chaleur ou de masse.

•L'analyse plus détaillée de la connectivité des réseaux de fractures est maintenant rendue possible par les algorithmes mis en place. Des indices topologiques peuvent en particulier être explorés et proposés pour caler la perméabilité équivalente calculée par la méthode de superposition ou par la méthode des graphes.

•Le couplage avec l'écoulement diphasique avec changement de phase dans les puits est une perspective immédiate. L'outil développé GeothFoam est conçu de façon à permettre ce couplage.

Finalement, les réservoirs poreux fracturés constituent un champ d'investigations intensif et interdisciplinaire. Le couplage hydraulique-mécanique-thermique-chimique est fort dans le contexte de la géothermie. Les résultats et les avancées explorées dans ce domaine d'application du sous-sol peuvent directement être extrapolés à d'autres domaines d'application comme le stockage géologique du CO2 ou l'ingénierie pétrolière et gazière par exemple.

Bibliography

[Adler and Thovert (1999)] Adler PM., Thovert J-F. (1999). Fractures and fracture networks. Dordrecht: Kluwer Academic Publishers; 1999.

[Adler et al. (2012)] Adler PM., Thovert J-F., Mourzenko VV. (2012). Fractured porous media. Oxford: Oxford University Press; 2012.

[Alghalandis (2017)] Alghalandis YF. (2017). ADFNE: open source software for discrete fracture network engineering, two and three-dimensional applications. Comput Geosci 2017; 102: 1–11.

[Anderson et al. (1984)] Andersson J., Shapiro AM., Bear J. (1984). A stochastic model of a fractured rock conditioned by measured information. Water Resour Res 1984;20:79. http:// dx.doi.org/10.1029/WR020i001p00079.

[Atkinson (1984)] Atkinson BK. (1984). Subcritical crack growth in geological materials. J Geophys Res 1984, 89:4077. http://dx.doi.org/10.1029/JB089iB06p04077.

[Balberg et al. (1983)] Balberg I., Binenbaum N. (1983). Computer study of the percolation threshold in a two-dimensional anisotropic system of conducting sticks. Phys Rev B 1983;28:3799–812. http://dx.doi.org/10.1103/PhysRevB.28.3799.

[Barenblatt et al. (1960)] Barenblatt, G., Zheltov, I., Kochina I. (1960). Basic concepts in the theory of seepage of homogeneous liquids in fissured rocks. J. Appl. Math. 24, 1286–1303.

[Barker (1985)] Barker, J. (1985) . Block-geometry functions characterizing transport in densely fissured media, Journal of Hydrology 77, 263–279.

[Beacher (1983)] Baecher G.B. (1983). Statistical analysis of rock mass fracturing. Math Geol , 15: 329–348. http://dx.doi.org/10.1007/BF01036074.

[Bonneau et al. (2013)] Bonneau F. , Henrion, V. , Caumon, G. , Renard, P. , Sausse, J. (2013). A methodology for pseudo-genetic stochastic modeling of discrete fracture networks. Comput. Geosci. 56, 12–22 .

[Bonnet et al. (2001)] Bonnet E, Bour O, Odling NE, Davy P, Main I, Cowie P, et al. (2001). Scaling of fracture systems in geological media. Rev Geophys 2001, 39: 347–83. http://dx.doi. org/10.1029/1999RG000074.

[Bruel (2018)] Bruel D. (2018). An attempt to generate physically-based DFN for coupled hydro-mechanical simulation. Proceedings of Computational Methods in Water Resources (CMWR). June 3-7, 2018, Saint Malo, France.

[Davy (1993)] Davy P. (1993). On the frequency-length distribution of the San Andreas Fault System. J Geophys Res 1993, 98:12141–51. http://dx.doi.org/10.1029/93JB00372.

[de Dreuzy et al. (2001)] de Dreuzy, J.-R., P. Davy, and O. Bour (2001). Hydraulic properties of two-dimensional random fracture networks following a power law length distribution 2. Permeability of networks based on lognormal distribution of apertures. Water Resour. Res. 37(8): 2079–2096.

[Dershowitz et al. (1988)] Dershowitz WS, Einstein HH. (1988). Characterizing rock joint geometry with joint system models. Rock Mech Rock Eng 1988, 21: 21–51. http://dx.doi.org/ 10.1007/BF01019674.

[Dong et al. (2018)] Dong S., Zenga L., Dowd P., Xu C., Cao H. (2017). A fast method for fracture intersection detection in discrete fracture networks.Computers and Geotechnics,Volume 98, pp.205-216.https://doi.org/10.1016/j.compgeo.2018.02.005

[Dykhiusen (1990)] Dykhuisen, R. (1990). A new coupling term for dual-porosity models, Water Resources Research 26(2), 351–356.

[Einstein et al. (1983)] Einstein H.H., Baecher G.B. (1983). Probabilistic and statistical methods in engineering geology. Rock Mech Rock Eng 1983, 16:39–72. http://dx.doi.org/10.1007/ BF01030217.

[Fourno et al. (2019)] Fourno, A., Ngo, T.-D., Noetinger, B., La Borderie, C. (2019). FraC: A new conforming mesh method for discrete fracture networks, J. Comput. Phys., 376, 713–732.

[Franz (2015)] Peter Franz (2015). OOMPFS – A New Software Package for Geothermal Reservoir Simulation. Proceedings World Geothermal Congress 2015 Melbourne, Australia, 19-25 April 2015.

[Garcia et al. (2018)] M. Garcia, J. Mathieu, D. Siffert. (2018). From Numerical Conceptual Models To Phenomenological Modelling and Production Optimization for Better Assessing. First EAGE/IGA/DGMK Joint Workshop on Deep Geothermal Energy. 2018: (Geothermal Reservoir Potential) Strasbourg, France.

[Gerke and Van Genuchten (1993)] Gerke, H. and VanGenuchten, M. (1993). Evaluation of a first-order water transfer term for varably saturated dual-porosity flow models, Water Resources Research 29(4), 1225– 1238.

[Hennings et al. (2000)] Hennings, P.H., Olson, J.E., Thompson, L.B. (2000). Combining outcrop data and threedimensional structural models to characterize fractured reservoirs : An example from Wyoming. AAPG Bulletin, 2000, vol. 84, no6, pp. 830–849.

[Herbert (1996)] Herbert AW. (1996). Modelling approaches for discrete fracture network flow analysis. In: Stephansson O, Jing L, Tsang C-F, editors. Coupled thermohydro- mechanical processes of fractured media, vol. 79. Amsterdam: Elsevier; 1996. p. 213–29.

[Huseby et al. (1997)] Huseby, O., J.-F. Thovert, and P. Adler, Geometry and topology of fractures ystemsd, . Phys.A Math. Gen., 30, 1-30, 1997.

[Huyakorn et al. (1983)] Huyakorn, P., Lester, B. and Faust, C. (1983. Finite element techniques for modeling grounwater flow in fractured aquifers, Water Resources Research 19(4), 1019–1035.

[Hyman et al. (2014)] Hyman, J.D., Gable, C.W., Painter, S.L., Makedonska, N. (2014). Conforming delaunay triangulation of stochastically generated three dimensional discrete fracture networks: a feature rejection algorithm for meshing strategy. SIAM Journal on Scientific Computing 36(4), 1871–1894.

[Hyman et al. (2015)] Hyman, J.D., Karra, S., Makedonska, N., Gable, C.W., Painter, S.L., Viswanathan, H.S. (2015). dfnWorks: A discrete fracture network framework for modeling subsurface flow and transport. Computers & Geosciences 84, 10–19.

[Hyman et al. (2017)] Hyman, J. D., Hagberg, A., Srinivasan, G., Mohd-Yusof, J., Viswanathan, H. S. (2017). Predictions of first passage times in sparse discrete fracture networks using graph-based reductions. Physical Review E, 96(1), 013304.

[Jasak et al. (2007)] Jasak, H., Jemcov, A., and Tukovic, Z.: OpenFOAM: A C ++ Library for Complex Physics Simulations, International Workshop on Coupled Methods in Numerical Dynamics, volume m, (2007), 1–20.

[Jing (2003)] Jing, L. (2003). A review of techniques, advances and outstanding issues in numerical modelling for rock mechanics and rock engineering. International Journal of Rock Mechanics & Mining Sciences 40, 283–353.

[Karra et al. (2018)] Karra, S., O'malley, D., Hyman, J., Viswanathan, H., Srinivasan, G. (2018). Modeling flow and transport in fracture networks using graphs. Physical Review E, 97.3, 033304. https://doi.org/10.1103/PhysRevE.97.033304

[Kattenhorn and Pollard (2001)] Kattenhorn SA, Pollard DD (2001). Integrating 3-D seismic data, field analogs, and mechanical models in the analysis of segmented normal faults in the Wytch Farm oil field, southern England, United Kingdom. Am Assoc Pet Geol Bull 2001; 85:1183–210. http://dx.doi.org/10.1306/8626CA91-173B-11D7- 8645000102C1865D.

[Kaviany 1995] M. Kaviany (1995). Principles of Heat Transfer in Porous Media, Springer, Berlin, 1995.

[Kazemi et al. (1976)] Kazemi, H., Merril, L., Porterfield, K. and Zeman, P. (1976). Numerical simulation of water-oil flow in naturally fractured reservoirs, Soc. Petrol. Eng. J. pp. 317–326.

[Kulatilake (1984)] Kulatilake PHSW, Wu TH. (1984). Estimation of mean trace length of discontinuities. Rock Mech Rock Eng 1984,17: 215–32. http://dx.doi.org/10.1007/ BF01032335.

[Landereau (2000)] Landereau P. (2000). Modèles macroscopiques pour les écoulements monophasiques en milieu poreux fracturé : Application aux tests de puits. PhD thesis, ENSAM, 2000.

[Lei et al. (2017)] Lei Q, Latham J-P, Tsang C-F (2017). The use of discrete fracture networks for modelling coupled geomechanical and hydrological behaviour of fractured rocks. Comput Geotech 2017, 85:151–76. https://doi.org/10.1016/j.compgeo.2016.12.024.

[Lim and Aziz (1995)] Lim, K. and Aziz, K. (1995). Matrix-fracture transfer shape factors for dual-porosity simulators, Journal of Petroleum Science and Engineering 13, 169–178.

[Long et al. (1982)] Long JCS, Remer JS, Wilson CR, Witherspoon PA. (1982). Porous media equivalents for networks of discontinuous fractures. Water Resour Res 1982, 18:645. http:// dx.doi.org/10.1029/WR018i003p00645.

[Long et al. (1985)] Long JCS, Gilmour P, Witherspoon PA. (1985). A model for steady fluid flow in random three-dimensional networks of disc-shaped fractures. Water Resour Res 1985; 21:1105–15. http://dx.doi.org/10.1029/WR021i008p01105.

[Macé (2006)] Macé L. (2006). Caractérisation et modélisation numériques tridimensionnelles des réseaux de fractures naturelles - Application au cas des réservoirs. Thèse de doctorat, Institut National Polytechnique de Lorraine, Nancy, France, June 2006.

[Matthäi et al. (2007)] Matthäi S. K., Geiger, S., Roberts, S. G., Paluzny, A., Belayneh, M., Burri, A., Mezentsev, A., Lu, H., Coumou, D., Driesner, T., Heinrich, C.A. (2007). Numerical simulations of multiphase fluid flow in structurally complex reservoirs. In Structurally Complex Reservoirs, Jolley S. J., Barr, D., Walsh J. J., and Knipe R. J. (eds.), pp. 405-429. Geological Society of London Special Publications 292.

[McClure and Horne (2014)] McClure, M.W., Horne, R.N. (2014). An investigation of stimulation mechanisms in Enhanced Geothermal Systems. Int J. Rock Mech. Min. Sci. 72, 242–260.

[Mourzenko et al. (2005)] Mourzenko VV, Thovert JF, Adler PM (2005). Percolation of three-dimensional fracture networks with power-law size distribution. Phys. Rev. E 72: 036103.

[National Research Council (1996)] National Research Council (1996). Rock Fractures and Fluid Flow : Contemporary Understanding and Applications. Washington D.C. : National Academy Press, 1996.

[Noetinger et al. (2001)] Noetinger, B., Estebenet, T. & Landereau, P. (2001). Transport in Porous Media, 44: 539. https://doi.org/10.1023/A:1010647108341

[Noetinger and Jarrige (2012)] B. Noetinger, N. Jarrige (2012). A quasi steady state method for solving transient Darcy flow in complex 3D fractured networks, J. Comput. Phys. 231(1) (2012) 23–38.

[Odeh (1965)] Odeh, A. (1965). Unsteady-state behavior of naturally fractured reservoirs, SPE Journal pp. 60–66.

[Paluszny et al. (2009)] Paluszny A, Matthä SK. (2009). Numerical modeling of discrete multi-crack growth applied to pattern formation in geological brittle media. Int J Solids Struct 2009; 46:3383–97. http://dx.doi.org/10.1016/j.ijsolstr.2009.05.007.

[Pandey et al. (2018)] Pandey SN, Vishal V, Ghaudhuri A. (2018). Geothermal reservoir modeling in a coupled thermo-hydro-mechanical-chemical approach: a review. Earth Sci Rev 2018; 185:1157e69.

[Pollard and Aydin (1988)] Pollard, D. D., and A. Aydin (1988). Progress in understanding jointing over the past century. Geological Society of America Bulletin, 100:1181–1204.

[Priest (1981)] Priest SD, Hudson Ja. (1981). Estimation of discontinuity spacing and trace length using scanline surveys. Int J Rock Mech Min Sci Geomech Abstr 1981; 18:183–97. http://dx.doi.org/16/0148-9062(81)90973-6.

[Pruess et al. (1999)] Pruess, K., Oldenburg, C., & Moridis, G. (1999). TOUGH2 User's Guide, Version 2.0. LBNL-43134.

[Quintard and Whitaker (1996)] Quintard, M. and Whitaker, S. (1996a). Transport in chemically and mechanically heterogeneous porous media i : Theoretical development of region-averaged equations for slightly compressible single-phase flow, Advances in Water Resources 19(1), 29–47.

[Renard et al. (1997)] Renard P, de MarsilyG (1997). Calculating equivalent permeability:Areview.AdvWater Resour 20:253–278

[Renshaw and Pollard (1994)] Renshaw CE, Pollard DD. Numerical simulation of fracture set formation: a fracture mechanics model consistent with experimental observations. J Geophys Res 1994;99:9359–72. http://dx.doi.org/10.1029/94JB00139.

[Robinson (1983)] Robinson PC (1983). Connectivity of fracture systems-a percolation theory approach. J Phys A Math Gen 1983; 16:605–14. http://dx.doi.org/10.1088/0305-4470/ 16/3/020.

[Robinson (1984)] Robinson PC. (1984). Numerical calculations of critical densities for lines and planes. J Phys A Math Gen 1984; 17:2823. http://dx.doi.org/10.1088/0305-4470/17/14/ 025.

[Salimzadeh et al. (2018b)] Salimzadeh S., A. Paluszny, H.M. Nick, R.W. Zimmerman (2018b). A three-dimensional coupled thermo-hydro-mechanical model for deformable fractured geothermal systems, Geothermics 71 (2018b) 212e224.

[Thorvaldsson et al. (2015)] Thorvaldsson L., Palsson H. (2015). Modeling Hydrothermal Systems with OpenFOAM. Proceedings World Geothermal Congress 2015 Melbourne, Australia, 19-25 April 2015.

[Thovert et al. (2011)] Thovert J.F. , V. Mourzenko, P. Adler, C. Nussbaum, P. Pinettes Faults and fractures in the Gallery 04 of the Mont Terri rock laboratory: characterization, simulation and application Eng. Geol., 117 (2011), pp. 39-51, 10.1016/j.enggeo.2010.10.003

[Valentini et al. (2007)] Valentini L., D. Perugini, G. Poli (2007). The "small-world'" topology of rock fracture networks. Physica A: Statistical Mechanics and its Applications 377(1): 323–328.

[Van Genuchten et al. (1984)] Van Genuchten, M., Tang, D. and Guennelon, R. (1984) Some exact solutions for solute transport through soils containing large cylindrical macropores, Water Resources Research (20), 335–346.

[Wallis (2007)] Wallis, W.D. (2007). A Beginner's Guide to Graph Theory, Birkhauser, Boston, 2007.

[Warren and Root (1963)] Warren, J. and Root, P. (1963) The behavior of naturally fractured reservoirs. SPE Journal (3), 245–255.

[Weiwi et al. (2019)] Weiwei Zhu, Bora Yalcin, Siarhei Khirevich and Tadeusz W. Patzek (2019). Fourth EAGE Conference on Petroleum Geostatistics, Florence, Italy, 2-6, sept, 2019.

[Wennberg et al. (2005)] Wennberg, O.P., Azizzadeh, M., Blanc, E. et al. (2005). Use of outcrop analogues in fractured reservoir characterization – an example from the Dezful Embayment, SW-Iran. In 67th EAGE Conference & Exhibition, Madrid, Spain, 13-16 June, 2005. pp. 1–4.

[Whitaker (1986)] Whitaker, S. (1986). Flow in porous media i : A theoretical derivation of darcy's law, Transport in porous media 1, 105–125.

[Whitaker (1999)] Whitaker, S. (1999). The Method of Volume Averaging, Kluwer Acad., Norwell, Mass., 1999.

[Yu et al. (2017)] Liyuan Yu, Richeng Liu, and Yujing Jiang (2017). A Review of Critical Conditions for the Onset of Nonlinear Fluid Flow in Rock Fractures, Geofluids, vol. 2017, Article ID 2176932, 17 pages, 2017. https://doi.org/10.1155/2017/2176932.

[Zhang et al. (2000)] Zhang L, Einstein HH. (2000). Estimating the intensity of rock discontinuities. Int J Rock Mech Min Sci 2000, 37: 819–37. http://dx.doi.org/10.1016/S1365-1609 (00)00022-8.

[Ziemmerman et al. (1993)] Zimmerman, R., Chen, G., Hadgu, T. and Bodvarsson, G. (1993). A numerical dual porosity model with semi-analytical treatment of fracture/matrix flow, Water Resources Research 29, 2127–37.